FACULTY
OF MATHEMATICS
AND PHYSICS
Charles University

DOCTORAL THESIS

Volodymyr Buturlim

U in metastable systems: structure, magnetism, superconductivity

Department of Condensed Matter Physics

Supervisor of the doctoral thesis: Doc. RNDr. Ladislav Havela, CSc.

Study programme: Physics
Specialization: Physics of Condensed Matter and Materials

Prague 2020

I declare that I carried out this doctoral thesis independently, and only with the cited sources, literature and other professional sources.

I understand that my work relates to the rights and obligations under the Act No. 121/2000 Coll., the Copyright Act, as amended, in particular the fact that the Charles University has the right to conclude a license agreement on the use of this work as a school work pursuant to Section 60 paragraph 1 of the Copyright Act.

In…...... date............ signature

Acknowledgments

During my doctoral study at Charles University I have obtained a lot of experience and knowledge applicable to my professional and personal life. I am happy to be a part of an environment where everybody is willing to share and learn. My supervisor Doc. RNDr. Ladislav Havela, CSc. is one of the people who guided me along the studies. I am grateful for all the knowledge, advices and scientific experience he transferred during these years. Our discussions were extremely beneficial for my personal development.

I also would like to express great thanks to RNDr. Silvie Mašková, Ph.D. who was always eager to instruct through the experimental procedures and help to solve different "puzzles". I have substantially benefitted from work with my colleague Mgr. Mykhaylo Paukov. He gave me valuable lessons of proper experimental approaches. In the same time, I would like to express the deepest appreciation to Dr. Hab. Nhu-Tarnawska Hoa Kim-Ngan, Ph.D. and her student Mgr. Sylwia Sowa from Institute of Physics of Pedagogical University in Krakow. They contributed a great deal of their time and efforts to investigate and present our studies to a broad scientific community.

I also address special thanks to RNDr. Daria Drozdenko, Ph.D. and RNDr. Peter Minárik, Ph.D. from the Department of Physics of Materials. Their persevering work significantly improved knowledge of the microstructure of the studied materials. In the same time my understanding of the technological and practical aspects of the crystal structure determination was raised thanks to profound discussions and assistance of RNDr. Milan Dopita, Ph.D., Doc. RNDr. Stanislav Daniš, Ph.D., Mgr. Lukáš Horák, Ph.D. and Dr. Khrystyna Miliyanchuk. I would like to express my appreciation to all colleagues from the Department of Condensed Matter Physics, particularly RNDr. Jiří Prchal, Ph.D. for his support in resistivity and high pressures measurements.

My thanks also go to the staff of the Materials Growth & Measurement Laboratory, Ing. Martin Žáček and RNDr. Jan Prokleška, Ph.D. for help and assistance during measurements on the laboratory equipment.

I wish to thank all my friends and family for support, inspiration and motivation.

Název práce: U v metastabilních systémech: struktura, magnetismus a supravodivost
Autor: Volodymyr Buturlim

Katedra / Ústav: Katedra fyziky kondenzovaných látek

Vedoucí doktorské práce: Doc. RNDr. Ladislav Havela, CSc.

Abstrakt: Tato práce představuje studium slitin a hydridů U-Nb a U-Ti syntetizovaných různými technologickými postupy. Výzkum mikrostruktury slitin s různými koncentracemi Ti (Nb) umožnil najít optimální parametry pro udržení metastabilní *bcc* alotropní fáze uranu. Ultrarychlé chlazení doprovázené legováním vede ke stabilizaci materiálů s vysokým stupněm neuspořádanosti na atomové úrovni, prokázané studiem transportních vlastností. Tyto slitiny vykazují slabě paramagnetický základní stav a nízkoteplotní supravodivost, která slabě závisí na koncentraci Ti (Nb) a vykazuje velmi vysoké hodnoty kritického magnetického pole.

Interakce s vodíkem umožňuje stabilizovat dvě charakteristické formy hydridu: β-UH_3 a UTi_2H_x. β-UH_3 legovaný Ti (Nb) se uspořádává feromagneticky s teplotami přechodu přesahujícími 170 K a slabě ovlivněnými koncentrací tranzitivních prvků. Vývoj hustoty elektronových stavů na Fermiho mezi byl sledován také studiem specifického tepla. Výsledky byly interpretovány v kontextu změn vzdáleností mezi atomy uranu.

UTi_2H_x reprezentuje kubickou Lavesovu fázi AB_2, která se však v tomto případě netvoří bez vodíku. Tento hydrid může pojmout různé koncentrace vodíku. Zkoumání magnetických vlastností odhaluje možnost stabilizace magnetické sloučeniny UTi_2H_6 a nemagnetické sloučeniny UTi_2H_5. Transportní a termodynamické vlastnosti UTi_2H_5 charakterizují tento materiál jako spinový fluktuátor přivedený do těsné blízkosti magnetického uspořádání.

Klíčová slova: Uran; Supravodivost; Feromagnetismus; Hydridy, Silné electron-elektronové korelace

Title: U in metastable systems: structure, magnetism, and superconductivity
Author: Volodymyr Buturlim

Department / Institute: Department of Condensed Matter Physics, Faculty of Mathematics and Physics, Charles University

Supervisor of the doctoral thesis: Doc. RNDr. Ladislav Havela, CSc., Department of Condensed Matter Physics, Faculty of Mathematics and Physics, Charles University, Prague, The Czech Republic

Abstract: This thesis presents studies of U-Nb and U-Ti alloys and hydrides synthesized via different technological paths. Investigation of the microstructure of the alloys with different concentrations of Ti (Nb) allowed to find the optimum setting for stabilization of the metastable *bcc* U allotrope. Ultra-fast cooling accompanied by alloying leads to retention of materials with high degree of atomic disorder apparent from the studies of their transport properties. The alloys exhibit a weakly paramagnetic ground state and low-temperature superconductivity, the critical temperature of which has only moderate variations with Ti (Nb) concentrations and which has very high upper critical fields.

Interaction with hydrogen allows to stabilize two distinctive forms of hydride: β-UH_3 and UTi_2H_x. β-UH_3 alloyed by Ti (Nb) orders ferromagnetically with transition temperatures exceeding 170 K, weakly influenced by the concentration of the transition elements. Development of the density of electronic states at the Fermi level was monitored by the studies of heat capacity. The results were interpreted in the context of variations of U-U spacing.

UTi_2H_x represents a cubic Laves phase AB_2, which is, however, in this case not form without hydrogen. This hydride can accommodate different concentrations of hydrogen. Investigation of magnetic properties reveals the possibility of stabilization of magnetic UTi_2H_6 and non-magnetic UTi_2H_5. Transport and thermodynamic properties of UTi_2H_5 characterize this material as a spin fluctuator poised at the verge of magnetic ordering.

Keywords: Uranium, Superconductivity, Hydride, Strong Correlations

Contents

Introduction

During the last 50 years different *ab initio* approaches and theoretical models were developed for the description of actinide condensed-matter physics and chemistry, but the desired universality has not been achieved yet. This is particularly true for actinides in the metallic state (metals, alloys, intermetallic compounds), in which Coulomb correlations in the system of conduction electrons bring an extra dimension, which cannot be approximated in any effective one-electron picture. The phenomena include superconductivity, magnetism in the sense of formation of moments and their ordering, heavy fermion behavior etc.

While these specific types of ground state are quite usual for ordered systems like 5*f* electron compounds where positions of particular atoms are defined, they can also occur in alloys which exhibit a statistical distribution of the constituent atoms over available lattice sites. Recent studies addressed the development of fundamental understanding of the physics of solid solutions of U and transition elements. Investigation of the correlations between the change of the transport and magnetic properties due to the hybridization of 5*f* -3*d* (4*d*) states and atomic disorder is useful for this purpose. The present work contributes to the subject by investigation of the U-Ti and U-Nb alloys and their hydrides. The ultra-fast cooling technique employed for the synthesis of alloys allowed to retain the metastable *bcc* allotrope of U. Essential features that depend on the concentration of the transitions elements are strong superconductivity and development of a flat temperature dependence of resistivity. Hydrogen considerably modifies the crystal and electronic structure of the alloys. Investigated hydrides exhibit two structure forms. β-UH_3 orders ferromagnetically, while the ground state of UTi_2H_x can be experimentally mediated by varying H concentration.

The thesis consists of a general introduction to the theory of magnetism and transport phenomena observed in simple metals and 5*f* electron materials (Chapter 1-5). Particular emphasis is given to a revision of the properties of U-based systems. Chapter 6 presents the experimental setups which were employed for the study. Discussion of the structural, magnetic, transport and thermodynamical properties of the studied U-Ti and U-Nb materials is given in Chapter 7. The last part is dedicated to a brief summary and future outlook.

1. Formation and ordering of magnetic moments

Classical physics allows to build a clear understanding of the phenomena which are appreciable at the macroscopic level, but things which are hidden from “naked eye” did not get a reliable description on the fundamental level until the 20th century [1]. Being observed already more than 2 thousand years ago, strong magnetism finds robust theoretical background only with the development of the quantum mechanics. Two important aspects of the magnetism will be described in the following sections. The first aspect is related to the formation of magnetic moments, while the second one discovers the problematics of the ordering of the magnetic moments in a solid state.

1.1. Magnetism of individual atoms

From the perspective of formation of magnetic moment, one should distinguish magnetism of a free atom and magnetism of condensed matter, which will be described later. There are three different components for the magnetic moment of a free atom, they are: spin, orbital angular momentum, and the change of the orbital momentum due to an applied magnetic field. Paramagnetic contribution to magnetization is related to spin and orbital momenta, while the last effect yields a diamagnetic contribution.

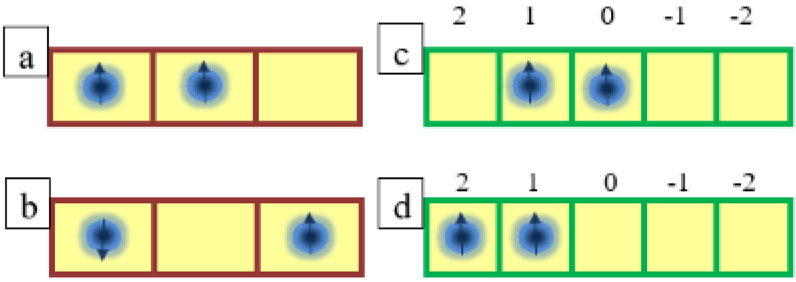

Fig. 1.1 Schematic representation of the filling of the atomic orbitals according to the 1st and 2nd Hund’s rule.

Formation of the atomic ground state is described by the Hund’s rules. Besides the description of the term symbol of multi-electron atoms, they also help to understand the magnetic properties of a specific element. The first rule defines the way in which electrons „occupy“ atomic orbitals. It pinpoints that the total spin angular momentum $\boldsymbol{S}=\sum_i \boldsymbol{s}_i$ should be maximized respecting the Pauli exclusion principle. Correspondingly the energetically favorable electronic configuration is depicted on the Fig. 1.1 (a), electrons with the opposite spins (Fig. 1.1 (b)) do not satisfy the rule.

In quantum mechanics, electronic orbitals of an atom are described by 3 quantum numbers (QNs): 1) principal QN $n=1,2,...;$ *2)* orbital angular momentum QN $l=0,1,2,3,...n-1$; 3) magnetic QN $m_l= l, (l-1), ..., 0, ..., -l, -(l-1)$. Each n has a corresponding group of orbitals called the K, L, M, N... shells (for $n=1,2,3,4...$ respectively). For instance, the shell N has four types of orbitals, l=0,1,2,3, respectively describes their angular momenta. These orbitals are respectively occupied by so-called *s*, *p*, *d*, and *f* electrons. The component of l parallel to a significant direction, e.g. external magnetic field, is also quantized, leading to $2l+1$ discrete states described by m_l. The second Hund's rule specifies how electrons fill these orbital states. It maximizes the total atomic angular momentum $\boldsymbol{L}=\sum_i \boldsymbol{l_i}$. Let us look at a d orbital with $m_l=2,1,0,-1,-2$ (Fig. 1 (d, c)). While the upper scheme would give $L=1$, the lower one with $L=3$ is correct as it satisfies the rule [2].

Interaction between a spin and angular momentum (spin-orbit interaction) of the same electron is introduced by the third Hund's rule. It says that total angular momentum J equals L-S when the shell is less than half filled, and $J=L+S$ when it is more than half-filled [3]. For clarity, let us look at rare-earth ions. Their electronic structure can be expressed as $(4f)^n(5s)^2(5p)^6(5d)^1(6s)^2$. They have an open 4$f$ shell, which is well screened from outer perturbation by the subsequent $(5s)^2(5p)^6$ shells. In solids, the outermost electrons are easily removed, producing tetravalent ions with well isolated 4f electrons, therefore they exhibit nearly atomic character Fig 1.2.

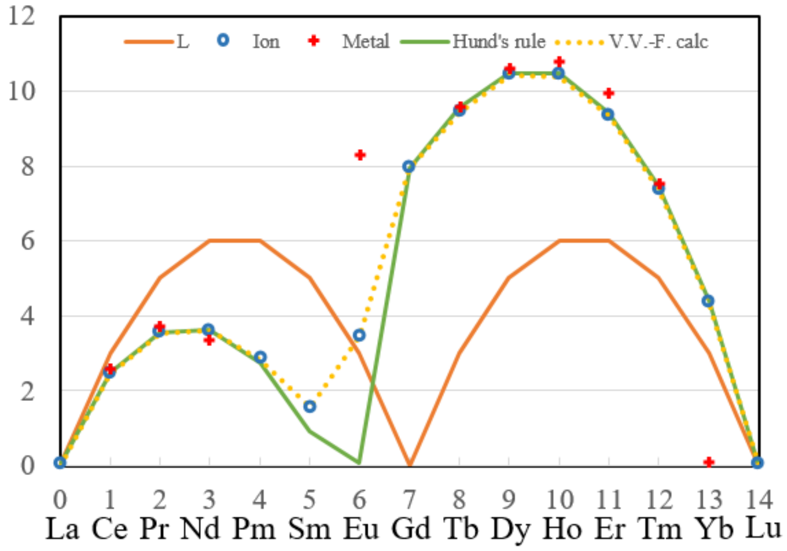

Fig. 1.2 Comparison of the effective magnetic moment of the 4f elements measured on ionic compounds and metals which are respectively depicted by open circles and

crosses. The solid line describes the moments calculated by the Hund's rules. Van Vleck and Frank calculation is presented by the dashes line [2].

The magnetic moments (and effective moments in the paramagnetic state) observed experimentally well agree with the values obtained by the Hund's rules (see Fig. 1.2). Magnetic moment as a function of the number of $4f$ electrons follows S and L, taking into account different values of the gyromagnetic ratio for the spin and orbital moments (the g-factor) calculated as:

$$g = 1 + \frac{J(J+1) + S(S+1) - L(L+1)}{2J(J+1)}$$

Anomalous magnetic moments of Sm and Eu ions were described by Van Vleck and Frank. These elements exhibit multiple terms, therefore their ground states and excited states produce different $\boldsymbol{J}$ [4].

1.2. Magnetism in solid state

1.2.1. Localized limit

In the previous section, the formation of magnetic moments of individual atoms was considered, but magnetism is a collective phenomenon, which involves number of units. In this section properties of the insulating and metallic systems with localized moments are discussed. Description of the magnetism of the insulating materials does not account for the cooperation between the localized atomic moments (*exchange interactions*). *Direct exchange interaction* between the moments is negligible, because the distance between atoms (ions) is too large, therefore such materials are usually modeled by means of independent moments located at particular sites. In metals the exchange is realized by means of the conducting electrons, this interaction is referred as *indirect exchange interactions*. The description of these phenomena is presented below.

Insulating rare earth compounds are relevant examples of the systems where electrons responsible for *paramagnetism* are localized at individual lattice sites. Such system can be described by a model that assumes the presence of *N* identical atoms (ions) in a volume *V.* Only the magnetic moment produced by the independent ions is the subject of interest. In such representation, individual moments can be determined by the Hund's rules, while determination of the temperature dependence of magnetization M and susceptibility χ becomes an atomic problem [5]. The model Hamiltonian is:

$$H = \sum_{j=1}^{N} \left(H_0^{(j)} + H_{\mathrm{SO}}^{(j)} - \boldsymbol{m_j} \cdot \boldsymbol{B_0} \right) = \sum_{j=1}^{N} H_{\mathrm{I}}^{(j)}$$

$H_0^{(j)}$ defines the term scheme of the jth ion, it is based on the electron-electron and electron-nucleus Coulomb interaction. Spin-orbit (SO) coupling of the jth ion is described by $H_{\mathrm{SO}}^{(j)}$. $\boldsymbol{m_j} = -\frac{\mu_{\mathrm{B}}}{\hbar} (\boldsymbol{S_j} + \boldsymbol{J_j})$ is the magnetic moment localized at the site R_j, therefore Zeeman energy equals $\boldsymbol{m_j} \cdot \boldsymbol{B_0}$. Strength of the SO coupling and Zeeman energy is decisive for the calculation of the magnetization:

$$\boldsymbol{M} = n\langle \boldsymbol{m} \rangle = \mathrm{k_B} T\, n\, \frac{\delta}{\delta B_0} \ln Z_1$$

Now calculation of magnetization is limited to the determination of the single-particle partition function $Z_1 = Tr(e^{-\beta H_I})$. It can be done for particular magnitudes of the following factors (see Table 1): 1) thermal energy $\mathrm{k_B} T$; 2) SO interaction $H_{\mathrm{SO}} = \Lambda(\gamma, LS)(L \cdot S)$; 3) magnetic field H_{Z}.

Table 1 Particular solution of the partition function for magnetization.

Case №	Description	Formula
1	Field and thermal energy is much larger than SO coupling one: $\hbar^2 \Lambda(\gamma, LS) \ll \mu_{\mathrm{B}} B_0 \ll \mathrm{k_B} T$ – then all terms of (LS) – multiples have equal probability to be occupied	$M \approx \frac{n\mu_{\mathrm{B}}^2}{3\mathrm{k_B} T} B_0 \{L(L+1) + 4S(S+1)\}$
		$\chi = \mu_0 \left(\frac{\delta M}{\delta B_0} \right)_T$ – Curie law $\chi(T) = \frac{n\frac{\mu_0 \mu_{\mathrm{B}}^2}{3\mathrm{k_B}} (L(L+1)+4S(S+1))}{T} = \frac{C_1}{T}$, where C_1 is the Curie constant
2	Field energy is close to the SO interaction energy:	$M = n \frac{\mu_{\mathrm{B}}^2}{3\mathrm{k_B} T} B_0 \{L(L+1) + 4S(S+1)\}$

Case №	Description	Formula
	$\hbar^2\Lambda(\gamma, LS), \mu_B B_0 \ll k_B T$ – SO coupling should not be negligible	$\chi(T) = n\frac{\mu_0\mu_B^2}{3k_B T}\left(L(L+1) + 4S(S+1)\right) = \frac{C_1}{T}$,
3	Strong SO coupling: $\hbar^2\Lambda(\gamma, LS) \gg \mu_B B_0, k_B T$	$M = M_0 B_J(\beta g_J J \mu_B B_0)$, where $M_0 = n J g_J \mu_B$ is saturation magnetization
		$\chi = n\frac{\mu_0 p_{\mathrm{eff}}^2}{3k_B T}\mu_B^2$ with $p_{\mathrm{eff}} = g_J\sqrt{J(J+1)}$

Weak SO coupling $\hbar^2\Lambda \ll \mu_B B_0$ and $\hbar^2\Lambda(\gamma, LS) \approx \mu_B B_0$ leads to the same form of magnetization (Table 1, cases 1 and 2). Strong SO coupling is usually realized in the 4*f*-systems (see Table 1, case 3). It is worth to mention that the described models are also applicable to certain 5*f* systems. Detail description of the solution of the partition functions for the cases presented above can be found in [6].

In metals, indirect exchange interactions transfer information about the localized spins between the neighboring ions. Particular configuration of the system leads to the *spontaneous* ordering of the magnetic moments below the critical temperature T_{Cr}. Such a collective magnetism divides into: *ferromagnetism* ($T_{\mathrm{Cr}} = T_{\mathrm{C}}$, T_{C} *– Curie temperature*), *ferrimagnetism* ($T_{\mathrm{Cr}} = T_{\mathrm{C}}$), *antiferromagnetism* ($T_{\mathrm{Cr}} = T_{\mathrm{N}}$, T_{N} *– Néel temperature*).

In rare earths, the indirect interaction is also clearly recognizable. For instance, gadolinium (Gd) which theoretically should have saturation magnetization of 7μB, exhibits slightly larger value 7.55μ_B (extra 0.55 μ_B appear due to intra-atomic 5*d* polarization), it is a ferromagnet with T_{C}=293 K [2]. In the material the means of the spin information exchange is the oscillatory polarization of the conduction electrons imposed by the localized 4*f* spins S. This interaction is called *RKKY interaction*, by the initials of the authors, Ruderman, Kasuya, Kittel and Yosida. The interaction can be expressed by the effective Hamiltonian: $H_{ij} = \sum_{i,j} J(R_{ij}) \cdot S_i \cdot S_j$, where $J(R_{ij})$ is the RKKY- coupling constant [6]:

$$J(R_{ij}) = \frac{J^2 k_\mathrm{F}^6}{E_\mathrm{F}} \frac{\hbar^2 V^2}{N^2 (2\pi)^3} F(2k_\mathrm{F} R_{ij})$$

Through the function $F(2k_\mathrm{F} R_{ij})$ it gets an oscillatory behavior (see Fig. 1.3). The distance between the magnetic ions R_{ij} influences the ground state magnetism of the system. The interaction can lead either to ferromagnetism or antiferromagnetism. In contract to direct exchange interaction which decreases exponentially with distance, RKKY interactions exhibit relatively larger range: $J(R_{ij}) \sim \frac{1}{R_{ij}^3}$. It also depends on the electron density (n_e) [6]: $J(R_{ij}) \sim n_e^{4/3} \sim (\frac{N_e}{V})_e^{4/3}$.

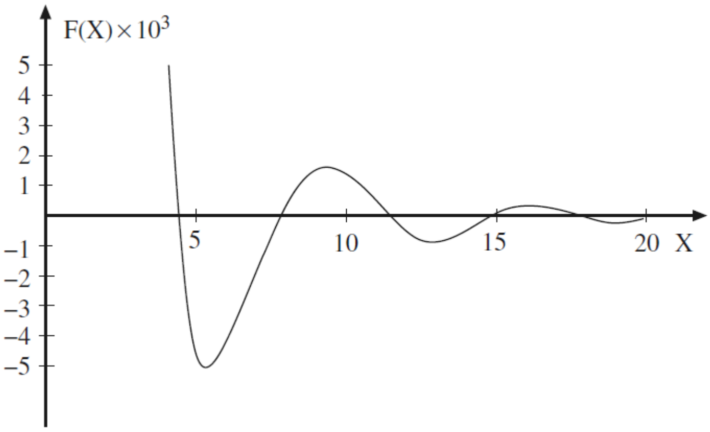

Fig. 1.3 Oscillatory behavior of the RKKY exchange is described by $F(x) = \frac{\sin x - x \cos x}{x^4}$, where $x = 2k_\mathrm{F} R_{ij}$ [6].

1.2.2. Band magnetism

In the system of transition metals one typically meets magnetism which does not have any distinct relation to the Hund's rules moment for any relevant electron configuration. For instance, iron is a ferromagnet with 2.2 μ_B per atom. With *d*-states, the only ones which can be responsible for magnetism, forming band states (Bloch waves), one has to understand how such band ferromagnetism (*itinerant* ferromagnetism) can principally arise. It develops in number of elemental metals (Fe, Co, Ni) and compounds (as $ZrZn_2$) and can be interpreted as unequal occupancy of spin-up and spin-down band states (spontaneous band splitting).

A rigorous description of the phenomena took a lot of theoretical efforts. The main reason of the complexity of the problem is the significant dependence on the many-body quantum interactions: among conducting electrons, among conducting electrons and ions, intra-ionic etc.

At the moment, there are various approaches for the investigation of the itinerant magnetism: 1) using model Hamiltonians in conjunction with many-body techniques; 2) application of the density functional theory (DFT) or its local density approximation (LDA), which have the advantage of being *ab initio* (they are restricted in ability to describe strong correlations); 3) LDA+DMFT (dynamical mean-field theory) merges band structure theory (LDA) and advanced many-body techniques (Dynamical Mean Field Theory, DMFT) [7].

For clarity, let us have a look at two basic models that present spontaneous band splitting: 1) Stoner model [8, 9] and 2) the one-band Hubbard model [10]. The conditions for spontaneous band splitting were originally introduced by Stoner. He considered nearly free electrons [11], which follow the Pauli exclusion principle (occupy the same energy state only when their spins are opposite, Fig. 1.4 (a)). The electrons fill the band states up to the Fermi energy E_F.

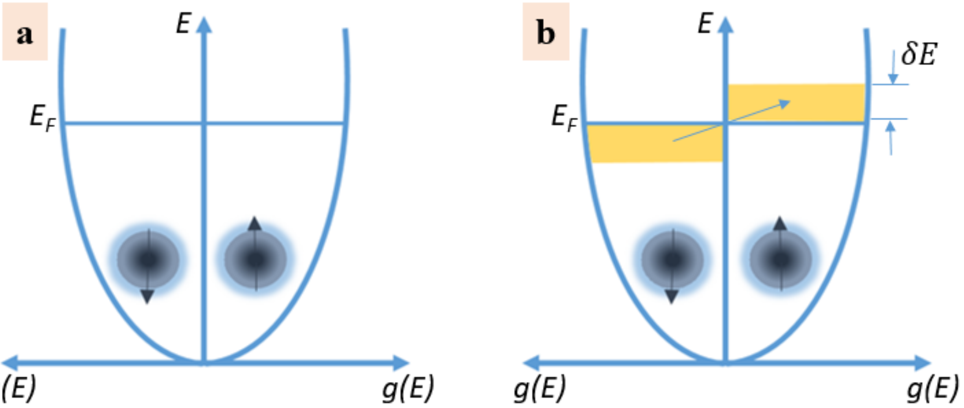

Fig. 1.4 Schematic representation of electronic bands with equal (a) and unequal occupation of the spin up and spin down states.

The origin of magnetism can be understood in a simple mean-field picture. When we take spin-down states from the slab between $E_\mathrm{F} - \delta E$ and E_F and move them to the spin-up band component (Fig. 1.4 (b)), this configuration will be more stable than the spin balanced one (Fig. 1.4 (a)) when the total energy change $\Delta E < 0$. During the described spin flip kinetic energy has to increase. The change of the kinetic energy depends on the density of states at the Fermi level $g(E_\mathrm{F})$, it equal to: $\Delta E_{\mathrm{K.E.}} = \frac{1}{2} g(E_\mathrm{F})(\delta E)^2$. Now we consider the situation when two electrons with opposite spin occur on the same site, they undergo a Coulomb repulsion, increasing their energy by the correlation energy U ($U = \mu_0\mu_{\mathrm{B}}^2\lambda$, typically several eV). Potential energy brought in by such a term gives on, then the potential energy change is: $\Delta E_{\mathrm{P.E.}} = \frac{1}{2}U(g(E_{\mathrm{F}})\delta E)^2$. The total energy change written in the following form shows that spontaneous magnetization, i.e., unequal occupancy of spin-up and spin-down states, is stable when $Ug(E_{\mathrm{F}})\geq 1$ [12]:

$$\Delta E = \Delta E_{\mathrm{K.E.}} + \Delta E_{\mathrm{P.E.}} = \frac{1}{2}g(E_{\mathrm{F}})(\delta E)^2(1 - Ug(E_{\mathrm{F}}))$$

This is known as the *Stoner criterion*. Ferromagnetic polarization of the band requires strong Coulomb interaction U and high $g(E_{\mathrm{F}})$. If the Stoner product $Ug(E_{\mathrm{F}})$ is below 1, the system has the Pauli susceptibility χ_{P} (magnetic susceptibility of the non-interacting electron gas) enhanced in following way: $\chi = \frac{\chi_{\mathrm{P}}}{(1-Ug(E_{\mathrm{F}}))}$.

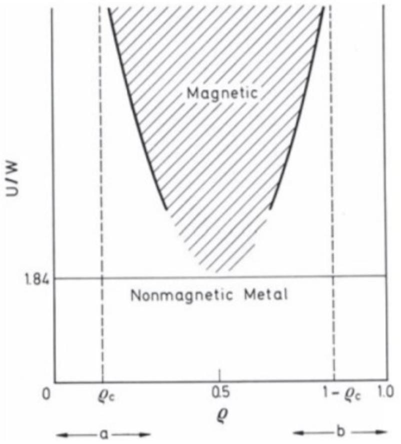

Fig. 1.5 Phase diagram of the one-band Hubbard model at $T = 0$ K [13].

Going beyond the mean-field level, the underlying physics is described by the Hubbard model. It incorporates the kinetic energy of electrons in a single band and intra-atomic Coulomb repulsion U between electrons with different spins (the Stoner U was just an effective parameter). The Hubbard Hamiltonian has the following form [10]:

$$H = \sum_{ij\sigma} t_{ij}c_{i\sigma}^{\dagger}c_{j\sigma} + U\sum_{i} n_{i\uparrow}n_{i\downarrow}$$

where $c_{i\sigma}^{\dagger}c_{j\sigma}$ are the creation and annihilation operators respectively, t_{ij} is the hopping parameter. $n_{i\uparrow}$ and $n_{i\downarrow}$ are operators of the number of particles with spin up and down, respectively, at the site i. The Hamiltonian is not solvable exactly, assuming that $E(k) = \hbar^2k^2/2m^*$ one can get the ground state energy equal to [13]:

$$E = NWg(E_{\mathrm{F}})^{\frac{5}{3}}\left[\frac{9}{5}+\frac{Ug(E_{\mathrm{F}})^{1/3}}{W+U(1-g(E_{\mathrm{F}})^{1/3})}\right],$$

here kinetic and potential energies were expressed in terms of the bandwidth W, the coupling constant U and the electron density $g(E_{\mathrm{F}})$. The ferromagnetic state will exist when: $\frac{U}{W} > \frac{1}{g(E_{\mathrm{F}})^{1/3}-(0.136)^{1/3}}$, and there is no solution below the critical density $g_{\mathrm{c}}(E_{\mathrm{F}}) = 0.136$. Even infinite interaction strength $U = \infty$ does not induce magnetic solution below the critical density, see Fig. 1.5.

1.2.3. Magnetism of the 5f electron systems

1.2.3.1. Electronic structure of the actinide materials from the perspective of 5*f* electrons

Actinide atoms have more than 89 electrons and their intra-atomic correlations complicate, besides the strong spin-orbit interaction, determination of their ground state configurations. Different computational approaches give different outcomes. For instance, self-consistent-field non-relativistic calculations performed by Liberman (1965) for Uranium [14] gave the ground state configuration $5f^2 6d^2 7s^2$, more than a decade later increase of the computational power allowed inclusion of relativistic effects which yielded generally accepted U configuration $5f^3 6d^1 7s^2$ [15]. Important relativistic effects (mainly the strong spin-orbit interaction) also affect ionic magnetic moments [16], *L*-*S* coupling scheme does not give a correct estimate, which is experimentally proven for Pu [17]. In other words, Hund's rules are not helpful for the understanding of the atomic magnetic properties.

In fact, the issue becomes even more complicated. The partially filled *f* shells of light actinides (Th, Pa, U) and lanthanides exhibit different properties. An early formulation of the realistic description of the actinide elements was presented by Hill, his analysis suggested that the 5*f* states in the light actinides cannot be treated as localized ones, the main reason is the considerable 5*f* wave function overlap [18]. Non-relativistic augmented-plane wave (APW) method utilized by Hill indicated that in light actinides the 5*f* electrons form a relatively broad band resembling electronic structure of transition metals. The later photoemission experiments confirm presence of the 5*f* band in the solid state [19]. Inclusion of the relativistic effects indicate that relativistic contraction of the core states leads to considerable expansion of the 5*f* orbitals. Even more important consequences is the sharp increase of the localization of the energy of the 5*f* electrons with increasing atomic number. It results in the rapid narrowing of the bandwidths [20, 21]. Particularly small bandwidth *W* promotes localization of the 5*f* electrons and the 5*f* states leave the Fermi level. For elemental actinides, the localization threshold is located between Pu and Am, as seen in Fig. 1.6.

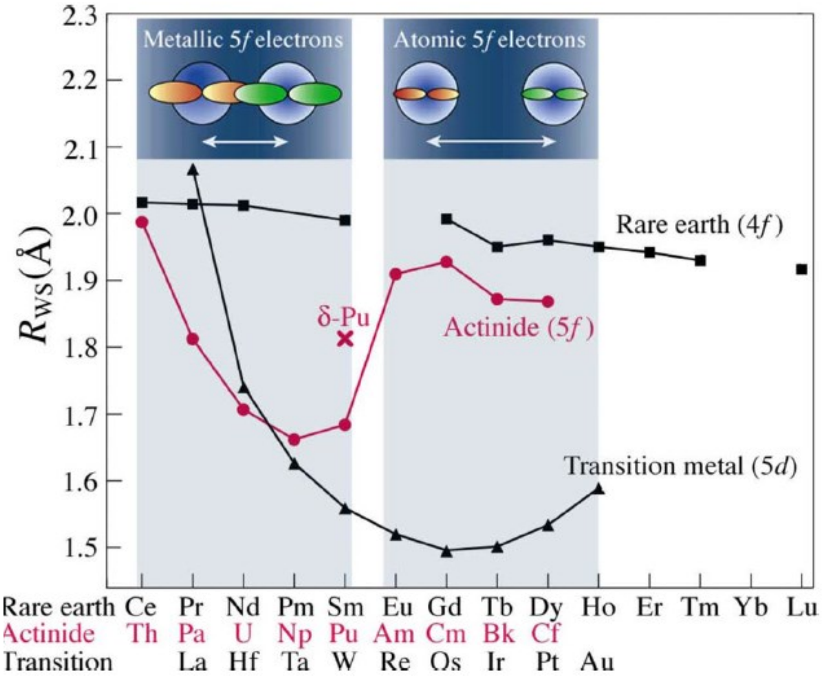

Fig. 1.6 Wigner Seitz atomic radii of the 5*d*, 4*f* and 5*f* elements which illustrate the similarities of the light actinides with *d*-electron series and heavy actinides with 4*f* [25].

The Mott localization, going beyond the framework of the band picture, depends critically on the ratio between the canonical 5*f* bandwidth *W* and interatomic Coulomb interactions which have the form of the Hubbard *U*. $U \approx W$ value represents the transition point, when $U \gg W$ the electrons are localized in space (not able to move between different lattice sites) [22]. Pu lies on the borderline [23]. It separates the series into light actinides described by energy band calculations and heavy actinides which require inclusion of the many-body physics [24]. It is clearly visible from the schematic illustration of the development of the Wigner Seitz atomic radii across the 5*d*, 4*f* and 5*f* series. Participation of the 5*d* electrons in bonding is characterized by the parabolic like behavior, on the other hand, localization of the 4*f* electrons and absence of their bonding role bring small volume changes. The actinide series is the only one crossing the localization point within pure elements (Fig. 1.6) [25]. The critical point, which can give rise to multitude of interesting emergent phenomena with large fundamental importance, cannot be in this way accessed sufficiently smoothly. Hence tuning by chemical composition (in compounds) or other external parameters becomes indispensable.

In the "*U*&*W*" description, the localized state gives rise to a metal-insulator (Mott) transition in theory [26]. However, in actinides we typically remain in the metallic state, in which the metallicity is maintained due to the itinerant 7*s* and 6*d* states, unless even those are gapped, as in actinide oxides.

The many body nature of the phenomena driving the Mott transition is a fundamental reason why it cannot be quantitatively accounted by current computational approaches. The phenomena which require further development of fundamental understanding include partial localization of the *f* electrons or sudden change of the bulk modulus and volume, etc. Last 30 years of the development of the condensed matter theory approaches these issues in different ways: 1) applying various models with corresponding simplifications (actinide model [27], Hubbard model [28]); 2) exploration of different *ab initio* (SP-LDA[1] [29], SIC-LSD[2] [24]) and semi *ab initio* approaches (DMFT[3]&LDA+*U* [30]). Nevertheless, the lack of the universality for the description of the magnetic and transport properties motivates further development and brings desire for more experimental data.

1.2.3.2. Formation of magnetic moments over the actinide series

Temperature independent magnetic susceptibility $\chi(T)$ of uranium, neptunium, plutonium and americium indicates non-magnetic ground state of the metals [31]. The thorough study of the borderline element Pu confirms the absence of either ordered or a disordered magnetic moment [32]. Am, being on the localized side already, is non-magnetic, as well, clearly due to the $5f^6$ state, giving $J = 0$ both assuming *L-S* or *j-j* coupling. Although some authors observed features which look like a transition from Curie-like to Pauli-like [33], it is believed that it is related to the radiation damage

---

[1] Spin polarized local density approximation.

[2] Self-interaction corrected local spin density.

[3] Dynamical mean field theory.

and/or material purity, being progressively more problematic, as the half-life of elements decreases fast (to several hundred years for common Am isotopes) with increasing atomic number Z. The susceptibilities $\chi(T)$ of curium, berkelium and californium fit the localized moment model [34].

Much larger atomic volume for localized 5*f* systems, see from Fig. 1.6, links the localization with the inter-actinide distances. On a finer scale, a band magnetism should appear before the threshold of localization is reached, which can be achieved in compounds, where the presence of other component(s) enhances the spacing. Convenient scheme introduced by Hill for light actinides takes into account the smallest inter actinide distances $d_{\mathrm{An\text{-}An}}$ [18]. The critical parameter called Hill limit (d_{C}) separates the "space" of the actinide compounds into two parts, the materials with $d_{\mathrm{An\text{-}An}}$ distance smaller than d_{C} often appear superconducting, whereas the compounds on the other side of the limit are non-superconducting, often magnetic. This feature is understood as a consequence of the influence of the direct 5*f* wave function overlap. The original Hill's work included, besides U, Np, and Pu also Ce. At present we know that the loss of magnetism of Ce and Pu has another driving mechanisms (Kondo effect or valence fluctuations), but the cases of U and Np reveal that the 5*f* overlap is usually the primary parameter we have to consider exploring the 5*f* states and their magnetism.

Useful relationships were also observed within the series of materials that form the cubic Laves phase (structure type $MgCu_2$). Investigation of the pseudo binary system $NpOs_2$ (T_{C} = 9 K) & $NpRu_2$ (T_{C} = 0 K, i.e. paramagnet) indicated gradual decrease of T_{C} and p_{eff} with reduction of the $d_{\mathrm{An\text{-}An}}$ distance [35]. These results supports the Hill's picture, nevertheless reader should bear in mind the fact that it does not take into account other phenomena (hybridization with non-*f* states, presence of *d*-moments). For instance, around half of the actinide compounds with $AuCu_3$ structure type do not form magnetic moment, despite their $d_{\mathrm{An\text{-}An}} \gtrsim 0.4$ nm, while Np_3Sn (0.328 nm) and NpB_2 (0.316 nm) order magnetically being at the verge of the Hill limit [34].

1.2.3.3. Magnetism in U alloys and compounds

All U allotropic modifications are Pauli paramagnets with temperature-independent magnetic susceptibility. Their smallest inter uranium distances $d_{\mathrm{U\text{-}U}}$ lie well below the Hill limit which ranges from 0.34 nm to 0.36 nm (Fig. 1.7). Binary U-T (T – transition element) intermetallics are paramagnets with moderately enhanced Sommerfeld coefficient γ, which reflects the density of states at the Fermi level, and the magnetic susceptibility $\chi(T)$ (for instance, UCo with the $d_{U\text{-}U} \approx 0.32$ nm) [36]. Magnetic moment can be induced by expanding $d_{U\text{-}U}$ e.g. moving from the 3*d* series to 4*d* and 5*d* elements which have larger atomic radii. Thus UPt with $d_{U\text{-}U} \approx 0.37$ nm is a ferromagnet with $T_C = 30$ K [37]. On Fig. 1.7, the distribution of the U compounds follows the Hill rule with the exception described below.

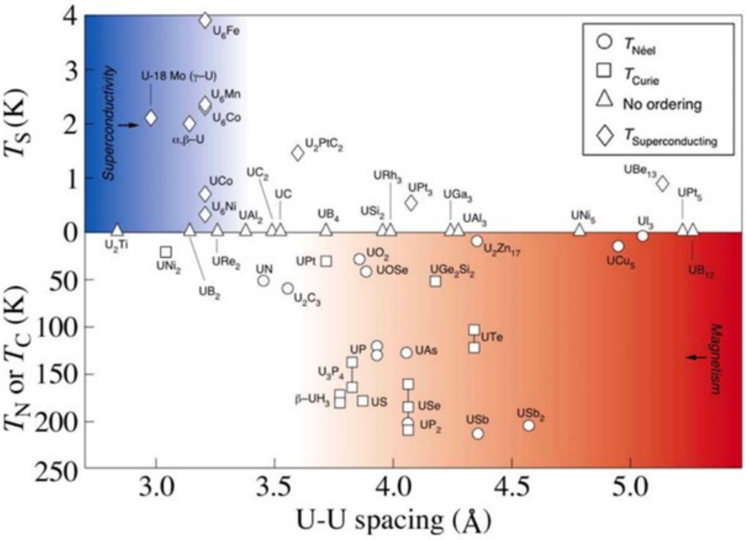

Fig. 1.7 "Hill plot" for selected U compounds taken from [25] which was modified according to the current state of knowledge. The reddish part of the graph represents the space of the magnetic compounds. The bluish area corresponds to non-magnetic materials.

Significant expansion (by 60%) of the metallic uranium lattice can be introduced by hydrogenation. Cubic β-UH_3 hydride formed from the orthorhombic α-U phase was the first discovered 5*f*-electron ferromagnet ($T_C = 170$ K) [38, 39]. The expansion from $d_{U\text{-}U} = 0.276$ nm to 0.331 nm allows formation of U magnetic moments of 0.9 μ_B/U, according to Bartscher two types of uranium atoms which are present in the structure are equally magnetic [40]. The Sommerfeld coefficient of the electronic specific heat γ increase by more than a factor of 3 from α-U to β-UH_3 (γ = 33.9 mJ/mol K^2) [41]. It highlights the probable reduction of the 5*f* function overlap and 5*f* bandwidth, which leads to the rise of the density of the states (DOS) at the Fermi energy $g(E_F)$ [42]. High-resolution photoelectron spectroscopy also supports this representation, it revealed dramatic modification of the 5*f* states [43]. Magnetism of the uranium trihydride β-UH_3 matches the Stoner framework described earlier, increase of the DOS near the Fermi level induces spontaneous band splitting. The saturation magnetic moment of 0.9 μ_B/U is significantly lower than the ionic moments ($\approx$3.2 μ_B for f^2 and f^3) was taken as due to the itinerant nature of the ferromagnetism. However, now we know that the partial cancellation of spin and orbital moment brings the situation that the total moment does not have a direct information in this sense.

The Curie temperature of β-UH_3 is high even though $d_{U\text{-}U}$ lies at the Hill limit (Fig. 1.7). The value of the ordering temperature distinguishes this U hydride among other compounds, which are typically either paramagnets or weak ferromagnets at similar inter U distances. The other UH_3 phase is α-UH_3, which has only one type of U atom in the structure and the shortest $d_{U\text{-}U} = 0.360$ nm. It is a metastable phase retained at low temperatures, therefore its magnetic properties were not well determined. Neutron diffraction studies suggested a non-magnetic ground state [44]. Nevertheless, recent report on the α-UH_3 hydride stabilized by Zr alloying shows that it is a ferromagnet with T_C similar to that of β-UH_3 ($\approx$ 180 K) [45].

The fact that these UH_3 hydrides with very different crystal structure exhibit almost identical magnetic properties suggested that the U-H interaction plays an important role [46]. Ab-initio electronic structure calculations discovered less extended 5*f* states below the Fermi energy. Comparing to U metal, significant hybridization between 6*d* and 5*f* states is lost. The U-6*d* occupancy is reduced by 50%, while the H-1*s* occupancy increased from 1 to 1.74 [47, 29]. Employing the GGA+*U* technique authors also obtained physically realistic orbital and spin uranium moments μ_L=3.19 μ_B, $\mu_S = -2.41$ μ_B (total $\mu = 0.78$ μ_B).

U based Laves phases represent high-density compounds with low values of U-U spacing. The compounds with transition metals can exhibit magnetism driven by *d* as well as *f* electron states. At the same time, there are many systems that are not magnetic, as a consequence of close packing. For instance, UMn_2, UCo_2, UIr_2 form cubic Laves phase with $d_{U\text{-}U}$ = 0.310 nm, 0.304 nm, and 0.324 nm, respectively, exhibiting paramagnetic ground state [36]. Isostructural UFe_2, with $d_{U\text{-}U} = 0.306$ nm, orders ferromagnetically ($T_C \approx 162$ K), but its magnetism originates mainly from the 3*d* electrons [48]. UNi_2 is a real exception from the rule, it is a weak itinerant 5*f* ferromagnet, in spite of the shortest U-U distance far below the Hill limit (0.303 nm). The formation of the low magnetic moment of 0.1 μ_B could be supported by the reduced 5*f*-3*d* overlap in the energy scale and corresponding suppression of hybridization [36]. Theoretical studies notice for those compounds the possibility of orbital moment antiparallel to the spin moment leading to practically zero total moment [49].

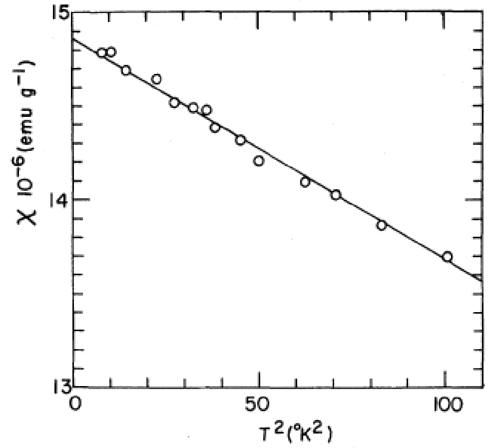

Fig. 1.8 Susceptibility χ (T^2) for UAl$_2$. The fit corresponds χ=14.86*10^{-6} (1-7.94*10^{-4} T^2) emu/g [50].

A larger atomic radius of Al even in the absence of 3*d* metals brings another Laves phase, UAl$_2$, close to the verge of magnetism. It had been recognized as an archetype of the spin fluctuating[4] materials. With $d_{U\text{-}U}$ = 0.338 nm it lies on the non-magnetic side of the Hill limit (Fig. 1.7). One of the characteristic properties of UAl$_2$ is enhanced magnetic susceptibility at low temperatures (Fig. 1.8), while the high-temperature part resembles the Curie-Weiss behavior (above 100 K). Spin fluctuations also induce a large Sommerfeld coefficient γ (140 mJ/mol K^2). According to theoretical studies, the absorption and re-emission of spin fluctuations renormalizes electronic self-energy, leading to the enhancement of the electronic specific heat coefficient γ [50]. B. Coqblin emphasizes that UAl$_2$ is a good example of the ferromagnetic spin fluctuator, in the antiferromagnetic case magnetic susceptibility is roughly temperature-independent [31].

---

[4] Spin fluctuations refer to “longitudinal” and “transverse” fluctuations of magnetic moment.

2. Electron and heat transport in matter

2.1. Classical and semiclassical description of the transport properties

2.1.1. Drude and Sommerfeld metals

Development of consistent models for the description of the transport properties in the condensed matter was started by Paul Drude. He treated the electrons in a metal as electron gas applying the kinetic theory of gases. The electrons were examined as non-interacting units which can only scatter by the heavy, immobile ions. Drude's approach allowed to build a simplified picture for rough evaluation of the thermal (κ) and electrical (σ) conductivity. The obtained quantities agreed with the Wiedemann-Franz law[5], while the electronic specific heat was overestimated by 100. The main drawback of the model was the assuption that the electron velocity distribution in equilibrium at temperature T is given by the Maxwell-Boltzmann distribution function.

In the Sommerfeld theory of metals the Pauli exclussion principle was taken into account leading to application of the quantum Fermi-Dirac distribution for the description of the electron velocities. The specific heat of the electron gas is found to be equal to: $c_v = \frac{\pi^2}{3} \mathrm{k}_\mathrm{B}^2 T g(E_\mathrm{F})$. In comparison to the classical result for the ideal gas ($c_v = 3n\mathrm{k}_\mathrm{B}/2$) Fermi-Dirac statistics depress the value by a factor of $(\frac{\pi^2}{3})(\mathrm{k}_\mathrm{B}T/E_\mathrm{F})$.

In a solid, the ionic vibrational degrees of freedom dominate the specific heat at high temperatures, below room temperature it falls as the cubic power of T. At very low temperature it drops below the electronic specific heat. Thus the total low temperature specific heat has the following form: $C = \gamma T + AT^3$, where γ is referred to as Sommerfeld coefficient. The Sommerfeld theory reasonably well describes heat capacity of the alkali and the noble metals [11].

2.1.2. Details of the electron and heat transport in metals

Understanding of the heat and electron transport requires a realistic description of the

---

[5] According to the Wiedemann-Franz law great number of metals exhibit the ratio of the thermal to the electrical conductivity, directly proportional to the temperature, $\kappa/\sigma = T\ L$ (where L is the Lorenz number).

interaction of electrons and phonons (ionic vibrations) between each other and with impurities. These phenomena define the dynamics of the processes. Wiedemann-Franz law which was deduced more than fifty years before the formulation of the reliable models suggested that electron and heat transport are closely related. Therefore we start from the description of the electronic conductivity of solids.

The assumption of the Drude model that electrons collide only with the ions failed to account for the observed temperature dependences. From the perspective of the modern physics the reason is clear, quantum effects should be taken into account. Within the Bloch solution of the Schrödinger equation the electron interactions with the periodic array are taken *ab initio*. It indicates that conduction within the perfect periodic crystal is infinite, because in the periodic array a wave can propagate without scattering. The approach that treats electrons in a general periodic potential is known as *semiclassical model*. In this model, the applied electronic and magnetic fields are treated classically.

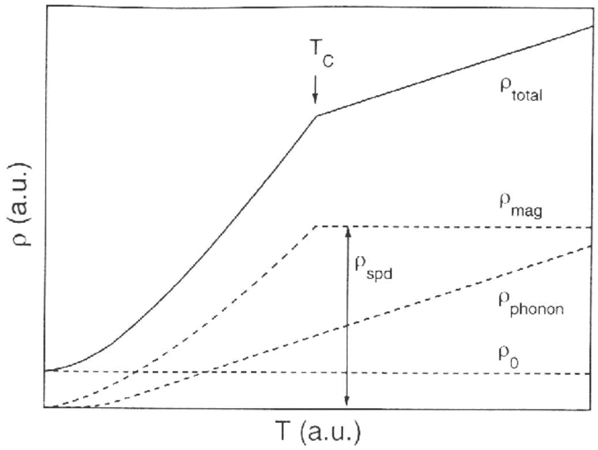

Fig. 2.1 Graphical representation of the Matthiessen's rule which indicates different contributions to the total resistivity, where: ρ_{phonon} – resistivity due to electron-phonon scattering, ρ_{mag} – contribution due to magnetic interactions (spin-disorder term), ρ_0 – residual resistivity.

Within the framework of the semiclassical model the conduction processes can be approached assuming that the electron distribution function does not affect the electron collision rate and the post-collision distribution function $g(\mathbf{k})$. This method known as the *relaxation time approximation* is the easiest way to show that the collisions do take place. It is relevant for description of the processes where details of the collision processes of little value (for instance, high frequency conductivity, high field Hall effect etc.). The results which are sensitive to the detailed features of the function form of the relaxation time $\tau_n(\mathbf{k})$ require more detailed description of the collisions. It is done by the solution of the Boltzmann equation: $\frac{\partial g}{\partial t} + \mathbf{v} \cdot \frac{\partial}{\partial \boldsymbol{r}} g + \mathbf{F}\, \frac{1}{\hbar} \frac{\partial}{\partial \mathbf{k}} g = \left(\frac{\partial g}{\partial t}\right)_{\text{coll}}$, where $\left(\frac{\partial g}{\partial t}\right)_{\text{coll}}$ is the rate of the change of the distribution function (more details present in [11]). This equation lies in the center of the theory of transport in solid.

In real materials the limited electron conductivity appears due to the crystal imperfections. The description of the particular electron collision depends on particular collision mechanisms which can be divided into several categories: 1) temperature independent scattering from the impurities and crystal defects; 2) temperature dependent interaction with the intrinsic deviations from the periodicity (due to thermal vibrations, magnetic ordering etc.). In certain circumstances the contribution of the individual scattering mechanism to the total scattering rate $W=1/\tau$ can be separated in the following way: $W=W^{(1)}+W^{(2)}=(1/\tau^{(1)})+(1/\tau^{(2)})$ (τ – relaxation time) [11]. It is known as Matthiessen's rule, and it allows to express electrical resistivity as sum of the scattering due to different mechanisms: $\rho(x,T)=\rho_0+ \rho_0(x,T)+ \rho_{\text{e-ph}}(T)+ \rho_{\text{mag}}(T)+ \rho_{\text{el-el}}$, where ρ_0 – is the residual temperature-independent contribution due to impurities and imperfections, while $\rho_0(x,T)$ represents the temperature-dependent contribution of the same origin. $\rho_0(x,T)$ term appears because many actinide materials do not strictly follow Matthiessen's rule. The main reason is that the electron mean free path cannot decrease below the inter-atomic spacing. Hence e.g. for strongly disordered systems, the electron-phonon scattering cannot have the same increment in resistivity as in clean periodic systems.

The temperature-dependent electron-phonon scattering is described by the Bloch-Gruneisen formula [34], it leads to T^5 dependence below the Debye temperature ($T \ll \Theta_D$) [36] for simple metals. ρ_{mag} represents the temperature-dependent contribution due to magnetic interactions, below the temperature of magnetic ordering (T_C, T_N) the resistivity exhibits a pronounced decrease due to gradually suppressed spin-disorder scattering (Fig. 2.1). At low temperatures the contribution of the electron-electron interaction term $\rho_{\text{el-el}}$ can be visible following the Fermi liquid scaling aT^2. In the U systems, a can be significantly higher than in simple metals. In the case of the vicinity of the onset of magnetic order lower exponents can be observed, 3/2 or 5/3 were predicted by the spin fluctuation theory [51] for the non-Fermi liquid regime.

More details on the modification of the low-temperature properties due to the enhanced electron-electron interaction will be presented in the next chapter.

Thermal resistance and conductivity associated with electrons also depend on the electrons' rate of interaction with impurities, phonons, and other electrons. The effect of the elastic scattering on static impurities is similar to electrical conductivity, it leads to temperature-independent relaxation time τ_{imp}, i.e. temperature-independent $\kappa_{\mathrm{imp}}=\frac{L_0 T}{\rho_0}$ (here Sommerfeld value $L_0 = L+S^2$, S – Seebeck coefficient). The common τ_{imp} for electron and heat transport maintains the validity of the Wiedemann-Franz (W-F) law. On the other hand, electron-phonon interaction contains an additional level of complexity. At high temperatures ($T \geq \Theta_{\mathrm{D}}$, Θ_{D} – Debye temperature) $\kappa_{\text{e-ph}}$ is temperature independent, because the high momentum phonons, which are present above Θ_{D} elastically scatter electrons. This process is similar for thermally and electrically perturbed electrons, therefore W-F law is satisfied. At low temperature, low energy phonons are incapable to scatter electrons in the steady state, which now require few collisions. For $T \ll \Theta_{\mathrm{D}}$ thermal conductivity $\kappa_{\text{e-ph}}$ should be proportional to T^{-2}, while electrical conductivity follows the T^{-5} dependence. This disparity is related with the fact that it is easier to relax thermally excited electrons, relaxation time for this process is shorter, consequently in this regime W-F law will not be satisfied. Electron-electron scattering is the process that introduces the smallest contribution to the transport properties. For instance, the ratio of the resistivity associated with the electron-electron scattering $\rho_{\text{el-el}}$, to the residual resistivity ρ_0 is proportional to 10^{-4}. Thermal conductivity associated with electron-electron scattering is proportional to $\frac{1}{T}$. At the moment, it is not possible to recognize it experimentally. The total thermal conductivity of electrons associated with the described processes is established as follows: $\kappa_{\mathrm{el}} = \frac{K_2}{T} - eSK_1$, where K_1 and K_2 are the transport coefficients defined by the temperature gradient [52].

While electronic thermal conductivity is a property of metals, thermal conductivity of lattice can be associated with any solid. Phonon-electron interaction is an important factor that influences the phonon distribution function. Therefore, the phonon-electron thermal-conductivity equals to $\kappa_{\mathrm{ph-el}} = G\left(\frac{T}{\Theta_{\mathrm{D}}}\right)^2 J_3(\frac{\Theta}{T})$, where $G = \frac{\mathrm{k_B^3 h}\theta_{\mathrm{D}}M}{2\pi^2 \mathrm{m_e^2} a^3}\sum_{j=1}^{3}\frac{1}{C_j^2}$. It depends on ion mass M and electron-phonon coupling constant C_j^2.

Above the Debye temperature Θ_{D} the phonon-electron thermal conductivity is temperature independent, while it rapidly decreases below Θ_{D}. The thermal conductivity of phonons is significantly lower than the electronic one, even at high temperatures it accounts only for ≈ 2 % of the total value. That can change in alloys because impurities affect the electron mean free path more than phonons distribution function. A detailed description of the transport phenomena could be found in [52] and [11].

2.2. Superconducting state in matter

In the previous section the properties of the normal metal were deduced from the uncorrelated single particle electron functions. Description of the superconducting phase requires inclusion of an attractive interaction between electrons with opposite spins. In fact, Leon Cooper emphasized that a system can gain energy when turning in the correlating state [53]. The BCS theory by J. Bardeen, L. N. Cooper and J. R. Schrieffer succeeded to explain most of the thermodynamical properties of the low temperature superconductors taking into account only two-body correlations [54]. The authors emphasize that the energy involved in the superconducting transition 8 order of magnitude lower than the repulsion energy due to Coulomb interaction. The interaction between electrons found to be a retarded effect of electron-phonon interaction [53]. It leads to “formation” of Cooper pair (a pair of electrons with zero total spin which can be separated by hundreds of nanometers). The electron pairs do not obey the Pauli exclusion principle, as bosonic particles, they can occupy the same energy state. In BCS theory binding energy of the pair (Δ) is the only parameter which defines properties of the superconducting state. From absolute zero to critical temperature T_{c} electronic structure of the BCS superconductor can be characterized by the energy gap of 2Δ crossed by the Fermi energy. Coupled electrons located below the gap require minimal energy of 2Δ to be excited in the normal state. For superconductors with weakly attracting electrons (in a weak coupling regime) BCS theory provides valuable predictions. Calculated free energy allowed estimate of the critical field and specific heat which agrees with experimental data (Fig. 2.2 (a)).

Specific heat of the matter in a superconducting state is higher than in a normal state. Near T_{c} the difference between normal and superconducting state specific heat can be estimated by formula: $\Delta C = C_{\mathrm{S}} - C_{\mathrm{N}} = 1.43\,\gamma\,T_{\mathrm{c}}$. Thus, $\Delta C/\gamma T_{\mathrm{c}} = 1.43$ is the main hallmark of a weak-coupling superconductor, higher $\Delta C/\gamma T_c$ usually indicates materials belonging to the strong coupling regime. The upper critical field of the weak coupling superconductor can be described by the Werthamer-Helfand-Hohenberg (WHH) theory. It gives the $T \rightarrow 0$ limit value H_{c2} (0) $\approx 0.7 \cdot T_c \cdot (-dH_{c2}/dT)$.

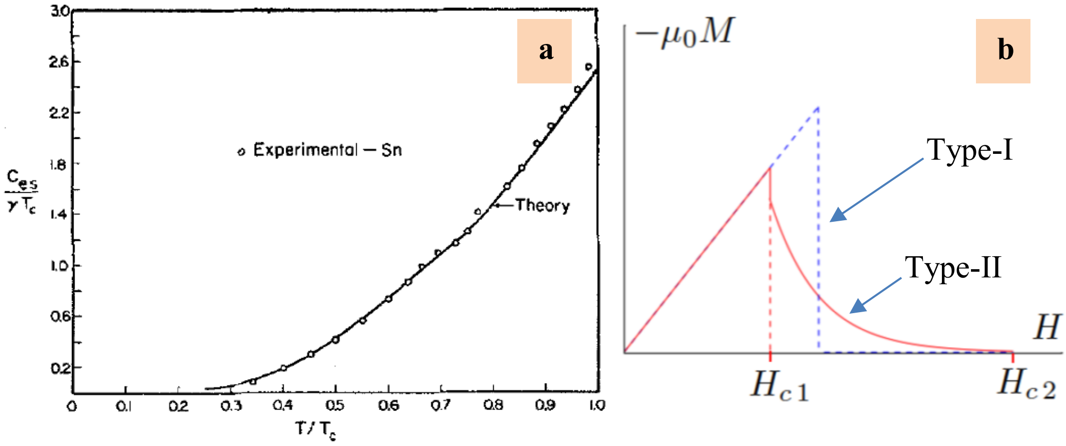

Fig. 2.2 (a) - comparison of the calculated ration of the electronic specific heat in the superconductor to the normal state value (T_c vs. T/T_c). Solid line presents the experimental value of Sn [53]. (b) - magnetization vs. magnetic field for the type-I and type-II superconducting phase [55].

Superconducting materials described by weak and strong coupling regimes are materials where interaction is phonon mediated. They can be sorted into type-I superconductors with one critical magnetic field, or type-II, in which magnetic field penetrates the superconductors in the form of flux lines. The complete suppression of superconductivity thus takes place only above the upper critical field H_{c2} (Fig. 2.2 (b)).

An exotic class of unconventional superconductors (UcS) comprises materials in which non-phononic superconductiong mechanisms appear. In those Cooper pairs can consist of electrons with parallel spins, and the coupling does not depend on electron-phonon interaction but rather on magnetic fluctuations. Futher information can be found in [56].

2.3. Electron and heat transport in Uranium alloys and compounds

Uranium based materials show electrical resistivities rather different from rare earth and transition metal compounds. The room temperature $\rho(T)$ value quantity often exceeds 200 μΩcm (compare with ≈ 1 μΩcm for Cu metal [51]). Earlier it was shown that the dominant resistance mechanism for normal metals is the electron-phonon scattering, leading to a monotonous increase of $\rho(T)$. For U systems the scattering on magnetic fluctuations becomes a strong effect. The additivity of the individual contributions of ρ becomes questionable, in other words, the resistivities of U compounds often do not follow the Matthissen's rule. Due to the strong anisotropy of exchange couplings, strongly anisotropic electrical resistivity appears, as e.g. in UNiAl [57, 58]. From the "Hill plot" presented in Fig. 1.7 one can see that the superconducting phase appears in compound with different shortest $d_{\text{U-U}}$. For UC, $d_{\text{U-U}} = 0.321$ nm and $T_c = 1.5$K, while the heavy-fermion compound UBe_{13} with $d_{\text{U-U}} = 0.513$ nm and $T_c = 0.9$ K lies on the opposite side of the plot [59], testifying unconventional nature of superconductivity. Some U compounds exhibit a complex phase diagram, as for instance, UPt_3 which superconducts below 0.5 K. Above the T_c specific heat indicates that it is a spin fluctuator [60]. The effect of the magnetic disorder is clearly seen from the study of single crystal of an antiferromagnetic compounds UNiGa [61]. In the vicinity of the magnetic transition $\rho(T)$ builds-up a gradual upturn (for $i||c$). It was attributed to the antiferromagnetic spin fluctuations, below the Néel temperature $\rho(T)$ drastically drops following ρ_0+AT^2.

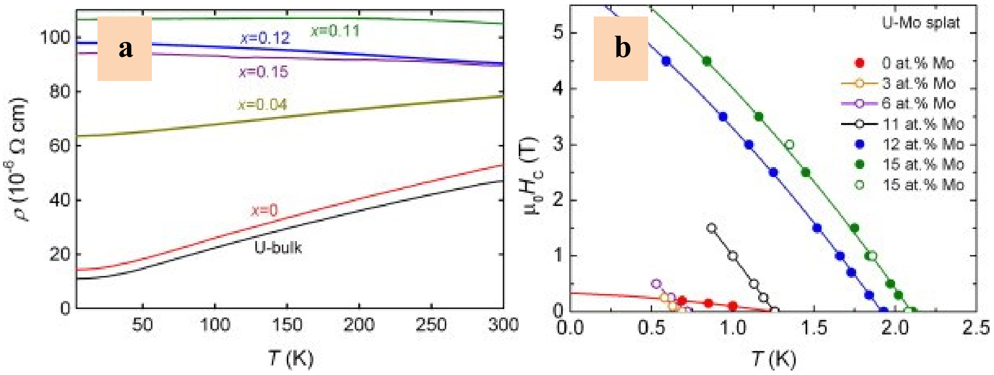

Fig. 2.3 (a) – electrical resistivity of the U-Mo alloys with Mo concentration span between 0 and 15 at.%; (b) – critical magnetic field H_c vs temperature T of the selected U-Mo alloys [62].

The low-temperature slope of resistivity $d\rho/dT$ in the concentrated alloys is another property that can be explored in U alloys. Mooij showed that low and even negative temperature coefficient of resistivity could develop in alloys with resistivity exceeding 100 μΩcm [63]. The author suggested that electron conduction reflects the fact that due to chemical disorder electron mean free path approached the lower limit. Early studies of *bcc* U alloys with Mo and Nb indicated that they are superconducting below 2K and their resistivity also obeyed negative temperature coefficient [64]. A recent investigation of the U-Mo alloy system revealed more details about the transport properties. The alloys with cubic γ and nearly cubic γ^0 (tetragonal) structure exhibit an increase of the superconducting transition temperature from 1.25 to 2.11 K (for 11 and 15 at.% Mo respectively). The resistivity measurement between 300 K and 3 K revealed an appreciable increase with $T\rightarrow$ 3 K and saturation in the low-T limit (Fig. 2.3 (a)). The largest increase of 8% was obtained for the alloy with 12 at.% Mo [62]. Authors suggest that the reason of the negative resistivity slope is the statistical distribution of the Mo atoms, which lead to a large disorder effect. Alloying also increases the critical field $\mu_0H_{c2}(0)$ of the alloys with cubic structure from 3.3 T to 5.3 T (for 11 and 15 at.% Mo, respectively) (Fig. 2.3 (b)). Despite intense discussion of the superconductivity of the orthorhombic α-U phase in [65] single-crystal study indicates that the phase transition is not present down to 0.02K [66]. It exhibits a series of charge-density wave (CDW) transitions.

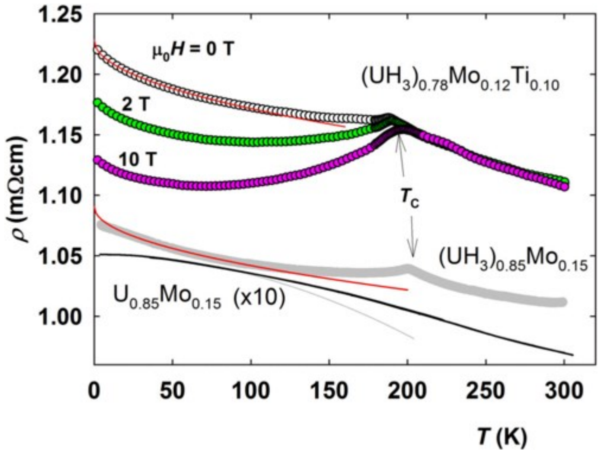

Fig. 2.4 White, green and pink circles represent the resistivity measurements of $(UH_3)_{0.78}Mo_{0.12}Ti_{0.10}$ in magnetic field of 0, 2 and 10T respectively [67].

Another mechanism of resistivity in magnetic materials is the spin-disorder scattering. This effect becomes more pronounced in the paramagnetic state where the electron spins are disordered. Microscopic difference between $(UH_3)_{0.78}Mo_{0.12}Ti_{0.10}$ and $(UH_3)_{0.80}Zr_{0.20}$ allowed to study the concept having two ferromagnetic systems with different length scale. The estimated distance between the scattering sites in the first hydride is an order of magnitude smaller, due to much reduced grain size, which leads to a more profound effect. It approaches the size of the electron wavelength leading to quantum interference and weak localization. The presence of the cusp in

$\rho(T)$ (see Fig. 2.4) of the $(UH_3)_{0.78}Mo_{0.12}Ti_{0.10}$ and $((UH_3)_{0.85}Mo_{0.15})$ was related to the interplay between electron-phonon/electron-impurity and ferromagnetic ordering [67]. Applied magnetic field gradually suppresses the magnetic excitations and magnetization in individual nano-grains, but the effect is negligible above Curie temperature (see Fig. 2.4). It highlights the role of the spin-disorder scattering.

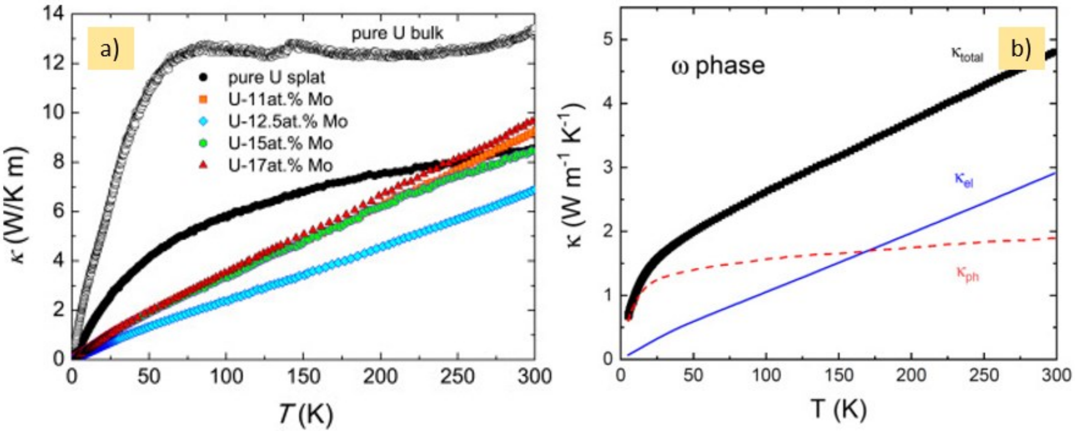

Fig. 2.5 (a) Thermal conductivity of pure U sample measured in bulk and splat form. The Mo alloyed samples were investigated only in splat-form [68]. (b) Thermal conductivity of $U_{0.27}Zr_{0.73}$ with the estimated electron (κ_{el}) and lattice (κ_{ph}) contributions [69].

There is no much data on the thermal conductivity of the U-base materials. Thermal conductivity is important property from the perspective of the energy "generation" abilities of the actinide-based materials, nevertheless, majority of the studies focus on the high-temperature conductivity of certain compounds (UP, UC, UP [70]; UO_2 [71, 72, 73], etc.). Most of the low-temperature data were obtained more than fifty years ago. Thus, pure U measured by R. O. A. Hall [74] exhibits a broad peak below 40 K and thermal conductivity $\kappa \approx 30$ W K^{-1} m^{-1} (at 100 K). A significant fraction was related to the lattice conductivity (≈ 10 W K^{-1} m^{-1} at 100 K). Authors indicate that the value can be overestimated, because at room temperature, it should reach 1.5 W K^{-1} m^{-1}. A recent study of pure U sample did not show any peak below 40 K, it was shifted to 90 K (see Fig. 2.5 (a)) [68]. At room temperature, absolute value of thermal conductivity is three times smaller than the one reported by Hall. The difference was related to the disorder effect. On the other hand, no maximum appears in the thermal conductivity of U-Mo splats (see Fig. 2.5 (a)), they exhibit a linear increase in the whole temperature range. Similar results were reported for $U_{0.27}Zr_{0.73}$, which crystalizes into distorted hexagonal ω-phase [69]. The authors estimated individual electron (κ_{el}) and lattice (κ_{ph}) contributions to thermal conductivity (see Fig. 2.5 (b)), at 300 K κ_{ph} accounts for ≈40 % of conductivity. Earlier we have indicated that enhancement of the phonon conductivity is usual for alloys. It looks like a higher disorder present in the U-Mo splats recovers the usual κ_{el}/κ_{ph} balance. The other effect, which can significantly reduce thermal conductivity, is the spin is the spin fluctuations inducing a dynamical Jahn-Teller distortion. A comprehensive study of a single crystal UO_2 highlights that it is the main source of reduction of the thermal conductivity with respect to isostructural ThO_2 [73].

3. Strong electron correlations in the U-based compounds

3.1. *Quantum phase transitions*

Classical theory of critical phenomena does not involve quantum mechanics. High temperatures destroy quantum coherence effects over the distances where critical phenomena could play their role. Discovery of the materials that do not fit the modern understanding of the condensed matter physics points out that certain missing pieces of the puzzle exist. The first description of the new form of order which emerges at the ground state was done by Hertz. He shows that in metals suppression of the magnetic phase transition temperature down to absolute zero produces "quantum critical point" (QCP).

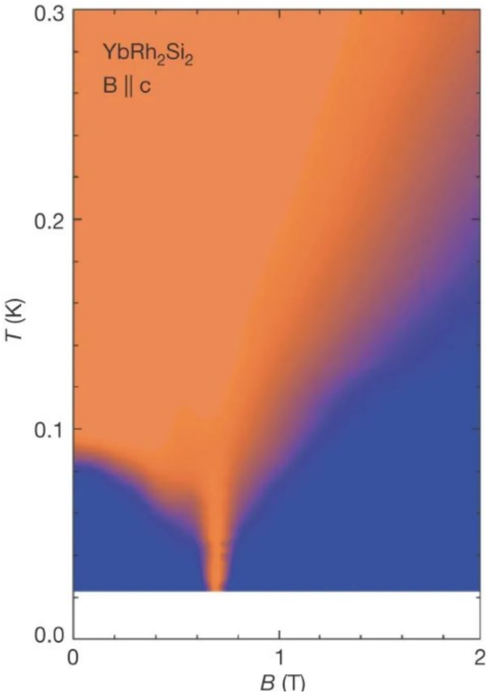

Fig. 3.1 Temperature-field phase diagram of the YbRh$_2$Si$_2$ close to QCP [79]. The normal metallic state is indicated by blueish regions, while orange regions represent anomalous metallic behavior with linear resistivity.

At QCP electron-electron interactions become infinite in space and time. In other words, the influence of the electron "movement" is perceived long after it was performed, the interactions become highly correlated [75]. For this type of QCP long-wave length fluctuations of the order parameter represent the only important degrees of freedom (for magnetic systems they are called paramagnons). Assuming two-dimensional spin fluid around the local moments X. Si proposed another class of QCP

[76]. It can be characterized by interaction localized in space and infinite in time. Nevertheless, for three-dimensional magnetic medium the theories introduced by Hertz and Si coincide [75].

Typically the materials with QCP contain rare earth or actinide elements. Tuning of the magnetic phase transition temperature can be performed by doping ($U_xTh_{1-x}Pd_2Si_2$ [77], $CeCu_{6-x}Au_x$ [78]), magnetic field ($YbRh_2Si_2$ [79], Fig. 3.1) and pressure ($CePd_2Si_2$ [80]), more examples of the materials can be found in the review written by G. Stewart [81]. Presence of QCP modifies low-temperature properties of the materials, in some cases non-Fermi liquid behavior can be observed for three temperature decades. The deviation of the properties helps to understand the nature of the quantum criticality. Recent measurements of the Hall-effect helped to get insight into the changes of the Fermi surface. The heavy electron material $YbRh_2Si_2$ exhibits sudden reconstruction of the Fermi surface in the vicinity of the QCP, corresponding to the loss of the electron mobility (discontinuous Fermi volume change) [82].

3.2. Modification of the low-temperature properties due to strong electron correlations

Strongly correlated electron systems take the central stage in the condensed matter research. Heavy fermion metals, high temperature superconductors, Kondo systems, exotic types of magnetic order are some of the examples. QCP materials described in the previous section belong to matter which also exhibits physically observable quantities different from the regular metal. These properties are described by the Landau Fermi liquid (FL) theory. With $T \to 0$, usual metallic electronic specific heat C/T is constant, with values reflecting the heavy effective masses of interacting quasiparticles. Magnetic susceptibility χ is temperature independent and resistivity ρ equals to ρ_0+AT^2. When the electron-electron interactions are too strong, the general FL scaling is lost. Several other distinct universality classes realize, depending on dimensionality and type of magnetic coupling, which are generally labelled as non-Fermi liquid behavior. Besides that, the FL scaling is lost (trivially) e.g. in strongly disordered systems. In magnetic systems, the Fermi liquid degrees of freedom are transformed into degrees of freedom of magnetic moments, which lose their internal structure, and the heavy Fermi liquid transfoms into the light Fermi liquid of remaining electrons around the Fermi level, while the low temperature properties are governed by magnetic excitations as magnons.

For the *f* electron systems, few proposed routes lead to non-Fermi liquid behavior [83]: 1) a multichannel Kondo effect [84]; 2) a distribution of Kondo temperatures [85]; 3) proximity to the QCP [86] and 4) the Griffiths phase model [87]. Each of the routes is characterized by a specific form of the low-temperature properties. Usually, they exhibit diverging *C/T*, χ and non-quadratic resistivity ρ. In the case of the multichannel Kondo effect extra spin susceptibility and specific heat per impurity mole diverge as: $\frac{C(T\to 0)}{T} = -\frac{A'}{T_\mathrm{K}} ln\frac{T}{bT_\mathrm{K}} + B'$, $\chi(T\to 0) \sim \frac{1}{T_\mathrm{K}} ln\frac{T}{b_\chi T_\mathrm{K}}$, with $A' = 0.251R, b = 0.41$, $b_\chi \approx 1$ and B' temperature independent electronic/crystal-field background. The electrical resistivity follows $\rho(T \to 0) \sim 1 - a(\frac{T}{T_\mathrm{K}})^{1/2}$ (a ~ 1). Materials with large disorder can exhibit distribution of Kondo temperatures T_K. This temperature distribution was also recognized as the origin of the modification of the transport and thermodynamical properties. The non-Fermi liquid dependences adopt following tendencies: 1) $C(T) \sim -Tln(T/T_0)$; 2) $\chi(T) \sim -\ln(T/T_0)$; 3) $\rho(T) \sim 1 - aT$ [83].

At QCP thermodynamical and transport properties are modified for a temperature decade above 0K (in extreme cases even higher). The fluctuations of the order parameter determine the properties. In other words, the QCP systems can be characterized by the correlation length and relaxation time ξ_τ (defined with the dynamical scaling exponent *z*). *z* can take values of 2, 3 and 4, which respectively correspond to antiferromagnetic, clean and dirty ferromagnet. Effective dimension $d_\mathrm{eff}=d+z$ relates the dimensionality of the quantum system *d* and the classical one. Within the renormalization group theory $d_\mathrm{eff}>4$ corresponds to Fermi liquid state [86].

Table 2 Comparison of the low-temperature dependencies close to QCP [81].

		AFM, *z*=2, *d*=3	AFM, *z*=2, *d*=2	FM, *z*=3, *d*=3	FM, *z*=3, *d*=2
Renormalization group theory	*C/T*	$\gamma - a\sqrt{T}$	$c \log (T_0/T)$	$c \log (T_0/T)$	$T^{-1/3}$
	$\Delta\chi$	$T^{3/2}$	$\chi_0 - dT$		
	$\Delta\rho$	$T^{3/2}$	T	T	

		AFM, 3-*dim*	AFM, 2-*dim*	FM, 3-*dim*	FM, 2-*dim*
Self-consistent renormalization group theory	C/T	$\gamma_0\text{-}a\sqrt{T}$	$-\log(T)$	$-\log(T)$	$T^{-1/3}$
	χ	$T^{-3/2}$	$-(\log T)/T$	$T^{-4/3}$	$-\frac{1}{T\log T}$
	$\Delta\rho$	$T^{3/2}$	T	$T^{5/3}$	T

There is no universal theory for the description of the QCP. At the moment different models were implemented for description of the physical properties in the vicinity of the QCP. Renormalization group theory can define the region of the T vs. δ (temperature vs. tuning parameter) phase diagram where quantum fluctuations dominate over the thermal ones, but the absence of the interactions broadens the range with classical behavior [81]. Some systems can be described within the framework of the self-consistent renormalization group theory. It introduces systematic treatment of the interaction between spin fluctuation modes, nevertheless, it does not account for the chemical disorder [81, 88]. Comparison of the low-temperature dependences of the physical properties is presented in the Table 2. The models coincide in the description of the 3D antiferromagnet, but other states get different representations.

3.3. Electron mass enhancement in U-based compounds

Number of U based compounds are found to be weakly or nearly magnetic systems, i.e. generally regarded in the proximity of the verge of magnetism. They exhibit different structure types, stoichiometries (UTX → UNiAl [58], U_2T_2X → U_2Pd_2In, UT_2 → UAl_2 [50], UT_3 → UPt_3 [89], etc.; T – transition element, X – p electron element) and their $d_{U\text{-}U}$ values are typically located close to the Hill limit. The most significant physical “fingerprint” of the materials is the anomalous low-temperature specific heat C. Enhanced correlations rise the values of the electronic contribution to specific heat (reflected in Sommerfeld coefficient γ) from 10 (for α-U [90]) to 830 mJ/mol K^2 (for U_2Pt_2In [91]). The other contributors to the increase are the spin fluctuations, which lead to a characteristic shape recognized in the C/T vs. T representation of the heat capacity. Narrow band intermetallic compound UAl_2 is an archetype of spin fluctuation materials. It stabilizes in cubic Laves phase modification (structure type $MgCu_2$) with the shortest inter-U distance $d_{U\text{-}U}$=0.338 nm [36].

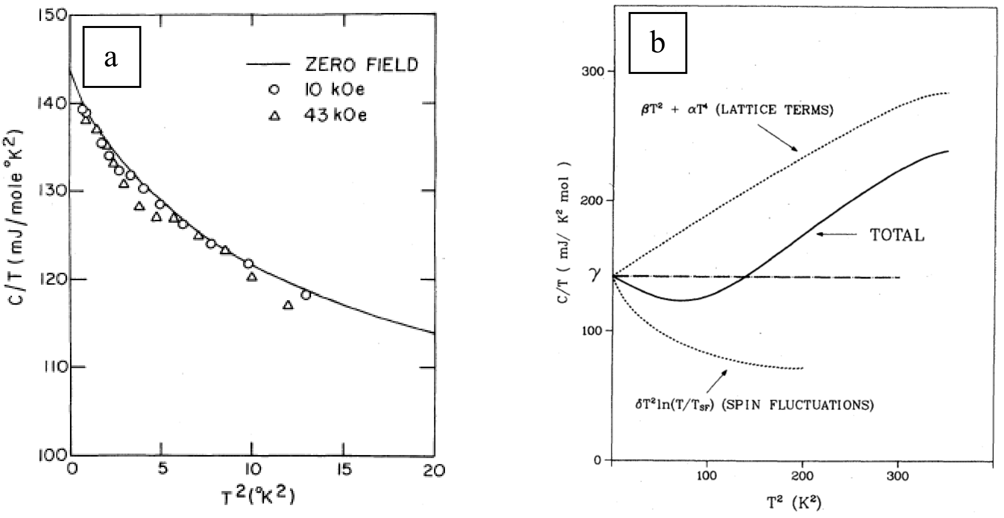

Fig. 3.2 (a) – the solid line represents the fit of the *C/T* vs T^2 data for UAl_2 (including spin fluctuation term) [50]. (b) – decomposition of the low-temperature specific heat into respective contributions of the lattice, electrons and spin fluctuations [92].

Ferromagnetic spin fluctuations lead to significant modification of the specific heat *C* of UAl_2. At low-temperature description of the *C/T* data require inclusion of the $T^2 \ln T$ term along with the regular electronic (γ) and lattice contributions (βT^2, (Fig. 3.2 (a))): $C/T = \gamma + \beta T^2 + T^2 \ln T$. Magnetic fields of 12.5 T results in 40% suppression of the low-temperature upturn at 2.1K [93], while the lower field of 4.3T suppresses *C/T* by less than 2% [50]. In his work Boring addressed the low-temperature specific heat data with a model which allows to get better insight into the physics of UAl_2. The data analysis was performed by the following formula:

$$\frac{C}{T} = \gamma + \epsilon T^2 + \delta T^2 lnT_{\mathrm{SF}} + \alpha T^4,$$

here $\gamma = \gamma_0(1 + \lambda_{\mathrm{e-ph}} + \lambda_{\mathrm{SF}})$ and $\epsilon T^2 = \beta T^2 - \delta T^2 \ln T_{\mathrm{SF}} + \mathcal{H}_{\mathrm{SF}}$. $\lambda_{\mathrm{e-ph}}$ and λ_{SF} correspond to electron-phonon and spin fluctuation contribution to specific heat. α and β represent phonon contributions. The contribution of the spin fluctuations can be taken as the sum of the enchancement of the electronic contribution γ_0 by λ_{SF} and reduction of the reduction by $\delta T^2 lnT_{\mathrm{SF}}$ which is valid below the spin fluctuation temperature T_{SF} (see Fig. 3.2 (b)) [92]. Estimated T_{SF} appears to be close to 40 K [92] which is higher than the earlier reported value of 12-16 K [50]. Investigation of the resistivity under pressure indicates that the temperature is risen by ≈25% at 1.8 Gpa suggesting that the compound becomes less magnetic [94]. On the other hand, doping can drive the system to a non-Fermi liquid (nFL)state. Mayr proves that for $U_{1-x}Y_xAl_2$ with $x > 0.875$ lnT term is found in the low temperature C/T [95]. From the perspective of this work understanding of the nFL and materials close to the magnetic ordering is an important ingredient required for the description of the studies systems.

4. Metastable alloys based on U

Phase diagram of U contains three crystallographically different phases below the melting point (1407.8±2 K). α-U is the allotropic modification which is stable at room-temperature and ambient pressure. This phase crystallizes in the orthorhombic structure with the space group №63, *Cmcm* with a = 2.8536 Å, b = 5.8698 Å, and c = 4.9555 Å (all ± 0.0001) [96]. It is stable between ≈ 942 K and 43 K. Neutron diffraction experiments showed that three transitions below T = 43 K are in fact structural instabilities, described as charge-density waves (CDW) [97].

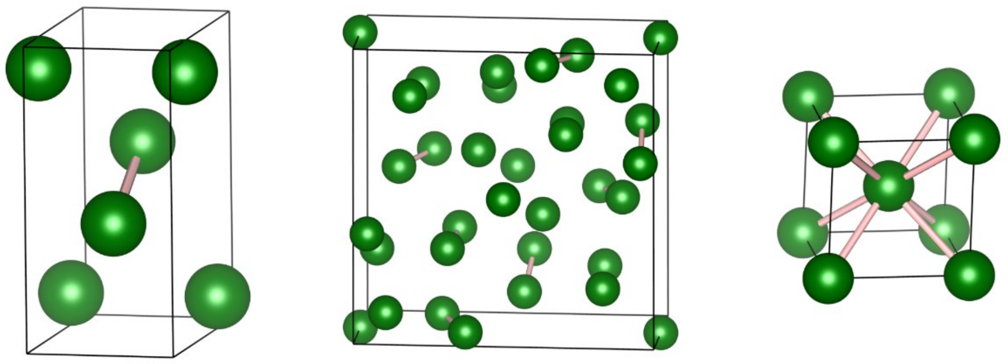

α-U: $d_{\text{U-U}}$≈2.80 Å   β-U: $d_{\text{U-U}}$≈2.889 Å   γ-U: $d_{\text{U-U}}$ ≈ 3.067 Å

Fig. 4.1 Crystalographic phases of Uranium with the corresponding shorted U-U distances. The shortest inter-Uranium distances are depicted by the bond sticks.

β-U (sp. gr. *P*4$_2$*/mmm*, a = 5.656 Å and c = 10.759 Å) exists in the temperature range 942 – 1049 K (± 2 K for both temperatures). Its complex structure exhibits 6 crystallographically independent atoms in the tetragonal unit cell. The γ-phase with a body-centered cubic A2-type of structure (sp. gr. *Im*-3*m*) and a = 3.472 Å is stable above 1049±2 K. Each U atom in the A2 arrangement is surrounded by 8 equidistant atoms which form a cubic coordination polyhedron. The difference of densities between the phases is not very large. The density of γ-U is only about 5% lower than the density of α-U (18.06 g/cm^3 compared to 19.04 g/cm^3), and a part of the difference is accounted to thermal expansion. The fact that alloying combined with fast cooling allows retaining the high-temperature phases down to room temperature allows to study their properties. More details will be given below.

4.1. Rapid solidification processing

A new era of the material processing started from the time when people realized that cooling rate can influence structure and phase composition of the materials [98]. A number of techniques for rapid solidification (RS) of metallic and non-metallic melts were developed in the second half of the 20th century (see Table 3). One of the main drives of the progress was the study of glassy materials, especially metallic glasses – not-crystalline matter with metallic properties. Their electron transport and magnetic properties influenced by the electron band structure modification motivated the investigational activity [99].

Table 3 Rapid solidification techniques [99].

Technique	Type	Cooling rate K/s	Sample shape
Single foil	Gun technique	10^9	Porous and irregular foils
	Piston anvil	10^7	Nearly circular foils
Extended foil/ filaments	Arc quenching	10^7	--
	Drum casting	10^7	2-3 mm wide ribbons
	Twin-roller casting	10^5	Fairly wide foils
	Melt spinning	10^6	Smooth ribbons
	Melt extraction	10^6	Fine wires and ribbons
Thin films	Plasma spraying	10^5-10^6	Porous Films
	Electric field atomization	10^6	--
	Lazer glazing (surface meting)	10^{10} - 10^{11}	Thick films 1-2 μm
Powder technique	Spark erosion	10^5-10^6	Particles 20-30 μm diameter

Starting from the early 1960s, the field of application of the RS processing also included exploration of fundamental phenomena around the metastable phase formation. In this context, various non-equilibrium techniques were broadly employed (laser pulse, ion implantation, particle bombardment, chemical deposition and sputtering). Gibbs free energy *G* is usually used to describe stability, instability, or metastability of certain phases. Variations of *G* as a function of atomic arrangement is depicted in Fig. 4.2. The stable state corresponds to the absolute minimum, while the atomic ordering in the relative minimum represents a metastable phase. Kinetics defines the metastable conditions where a system can end up. Metastable structure can be synthesized only in the case when kinetically preferred path differs from the thermodynamically preferred one [100].

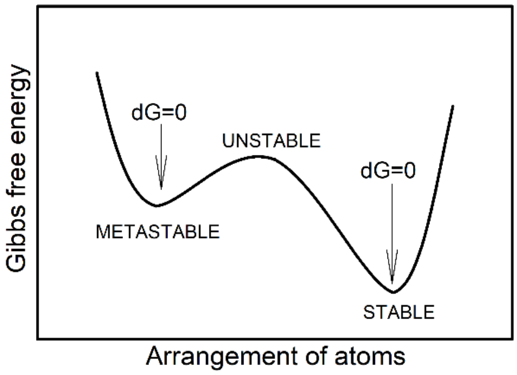

Fig. 4.2 Schematic representation of the free energy of the system as a function of atomic arrangement [100].

Different types of metastability can be considered, namely compositional, structural, morphological, and topological. These metastability types are characterized by different energy deviations from the equilibrium state. The energy difference can be scaled by R^*T_m, where T_m is the average equilibrium melting temperature of the components, R is the gas constant. Composition metastability implies the highest excess energy ($\approx 1^*R^*T_m$). For the same composition and different structure, the energy difference is typically about $0.5^*R^*T_m$. Topological metastability is characterized by the lowest energy difference ($0.1^*R^*T_m$) [100].

Construction of the equilibrium phase diagrams requires knowledge about the free energy of a phase at particular composition, pressure, and temperature. Earlier it was mentioned that certain kinetic reasons may promote metastable phases, in this case the common tangent rule is applied to the new equilibria and certain modifications result in a metastable phase diagram. Active investigation of the influence of the cooling rate on microstructure and phase composition showed that the changes can be dramatic. Low cooling rates lead to a microstructure which are close to the equilibrium one, while high cooling rates can result in fine microstructure which is far from equilibrium. For example, thorough studies of stainless steel under different cooling conditions indicate that at certain Cr/Ni ratios in the Fe-Cr-Ni system the primary solidification mode (PSM) can be altered by cooling rate, which stresses the role of chemical composition as an important variable in the development of microstructure [101].

4.2. γ-U phase

In 1937 Jacob and Warren reported the correct crystal structure of α-U [102], but more than a decade passed before *bcc* γ-U was described correctly. The main challenge was related with the determination of the room temperature lattice parameter. It required development of experience in the field of Uranium metallurgy. The first solution for the problem was achieved via high-temperature X-ray measurements. In practice, a strong predisposition of Uranium to oxidation led to contamination of the X-ray diffraction patterns with the oxide reflections. The lattice parameter of the pure γ-U phase obtained at 800ºC equals to 3.487 ± 0.001 Å [103]. Assuming the Vegard's law, the authors also determined the room temperature value from high Mo concentration alloys, having found that Mo tends to stabilize the *bcc* structure. A graphical extrapolation from the lattice parameters obtained from *bcc* U-Mo alloys with different Mo concentrations led to $a = 3.474 \pm 0.005$ Å. A later study performed at 805 ºC suggests $a = 3.524 \pm 0.002$ Å [104].

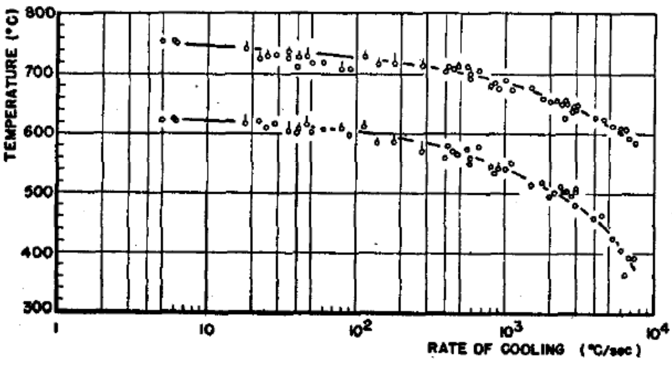

Fig. 4.3 Effect of the cooling rate on the allotropic transformation temperatures between γ→β (upper curve) and β→α [105].

Started from 1950's, uranium science was spurred due to the interest in nuclear energy. A primary imperative for nuclear fuel is its dimensional stability. α-U exhibits anisotropic thermal expansion, γ-U with the cubic unit cell expands isotopically, in this sense it is the best choice among the Uranium allotropes. Studies of the effect of the cooling rate on structural phase transformations indicated that it is not possible to retain the high-temperature phase down to room temperature. Cooling by means of helium jet allowed to investigate rates in the range from 5 to 8000 K/s. Despite the fact that γ-U was not stabilized down to room temperature, the temperature of the γ→β transition was substantially depressed (by 150 K, see Fig. 4.3) [105].

The first studies of U alloy with low Mo concentration (2.8 at.% of Mo) suggested that the γ→β transition was not suppressed in the case of enhanced cooling rate combined with alloying [106]. On the other hand, later study of the effect of cooling rate on the decomposition of the γ-U in the U-Mo alloys indicated that γ→γ+α transformation occurs even in U alloy with 2.5 at.% of Mo with an approximate rate of cooling equal 400 K/min [107]. In the following work the assumption was confirmed, study of the alloys with 0.9 and 1.7 at.% of Mo shows that if β-U phase forms during quenching, its stability increases with increase of the Mo concentration [108]. Suppression of the γ→β transition proves that the concentration of Mo in the alloys influences the phase composition along with transformational dynamics.

The highest cooling rate was obtained by mercury quenching, giving ≈ 400 K/min. It allows stabilizing the tetragonally distorted modification of γ, which is denoted γ^0, with 12.5 at.% of Mo, no other phases were detected metallurgically. On the other hand, investigation of the structure changes along the direction of the quench temperature gradient indicates that γ and α formed even for 2.5 and 5 at.% Mo alloys with lower cooling rates, faster cooling stabilized the α′ phase (α phase with contracted *b* parameter due to a certain amount of Mo presented). This α-type of phase can probably accommodate even higher Mo concentrations, which leads to a monoclinically distorted phase α″, mentioned for 10 at.% Mo besides γ^0 (γ^0 forms in the case of slower cooling). Mercury quenching allows retaining pure γ phase alloy with anisotropic grains only for 15 at.% Mo alloying. In his study Hills also described the changes of the microstructures with respect to different cooling rates and Mo concentration. He shows that alloys with 11.5 at.% Mo form banded[6] structure with fast cooling (mercury quenching), while the oil-cooled alloy (slower cooling) exhibits polygonal structure. In the alloys with lower Mo concentration banded structure was observed for the fast cooling, slower cooling lead to formation of lamellae [107].

---

[6] Microstructural banding can be defined as alternating of two different microstructure layers which is caused by fluctuations in the concentration of alloying elements. More details can be found here [201].

Tangri extended the knowledge about the effect of the cooling rate using air cooling (10 K/s), argon quench (220 K/s) and water quenching (1000 K/s) [109]. In the cited work, the author shows that for U with 11.18 at.% Mo the α″ phase forms in the water quenched sample, while the air-cooled sample exhibits the γ^0 allotrope. More details can be found in the works which present metallurgical studies performed by Hills, Tangri and Harding [107, 108, 109, 110].

Later work on U-Mo alloys shows that the γ phase can be stabilized with 8 wt.% of Mo (17.7 at.% Mo) [111]. On the other hand, application of ultra-fast cooling allowed to stabilize (in fact to retain) the phase with 11-12 at.% of Mo [112]. Ultrafast cooling allows applying cooling rate as high as 10^6 K/s. Unlike mercury quenched alloys studied by Hills [107], ultrafast cooling leads to a dominance of the γ phase already in the 10 at.% Mo alloy, and the α phases vanish for 11 and 12 at.% Mo alloys exhibiting the tetragonally distorted *bcc* (γ^0) structure. This results indicate that ultrafast cooling is more efficient than mercury and water quenching. It also contradicts with the conclusion that slow cooling is required for stabilization of the γ^0 in alloys with 10-12 at.% of Mo. The last studies mentioned [111, 112] have already implemented modern diagnostic techniques as TEM with EBSD, capable of capturing the distribution maps of individual crystal phases, not only maps of elemental composition.

Although it has not been clearly articulated, we can assume that the *bcc* phase retention depends on a large extent on slow diffusion of Mo out of U, as the α-U phases tend to be lean in Mo. The unique Uranium orthorhombic phase is unwilling to incorporate Mo or other element. For instance, phase diagrams of U-Ti and U-Nb systems show that α-U incorporates only few % of the transition elements (see Fig. 4.4).

Zirconium is less efficient γ phase stabilizer than Mo. Hills applied mercury quenching for alloys with Zr concentrations which range from 2.5 to 50 at.% [113]. The author indicates that the γ phase cannot be even partially retained with Zr concentration below 30 at.%. On the other hand, helium gas quenching allowed to obtain a single phase *bcc* sample with 25 at.% of Zr [114]. A significant reduction of the required Zr concentration was also observed in the case of ultrafast cooling [66]. The specimen with 15at.% Zr exhibits dominant γ-U reflections, however, traces of the most intense peaks of the α′-U phase are present in the diffraction pattern of the 20 at.% Zr alloy.

4.3. Stabilization of bcc U by Ti and Nb

Along with the study of the representative U-Mo and U-Zr alloys, other elements were examined. Early studies of the U-Ti alloys suggested that even a small concentration of Ti increases corrosion resistance [115], for instance, U 14 at.% Ti alloys exhibit 10 times better performance than the pure U. It is also emphasized that an increase of the Ti concentration reduces the γ→β transition temperature. In [110] authors present study of the effect of the impurity concentration and cooling rate on the appearance of the γ-U phase. Direct water quenching of the alloys with 4.9 and 9.2 at.% of Ti results in the formation of the α-phase based Widmanstatten microstructure. Air quenching has different effect, it stabilizes the equiaxed α-U grains. Mercury quenching of the alloy with 9.2 at.% of Ti allows to stabilize γ-U, nevertheless, some α-U grains were also present. Investigation of the cross-section shows that starting from the quenched tip concentration of the α-U grains increases. It highlights that quenching rate is an important parameter that defines the phase composition of the U-Ti alloys. Study of the water quenched U-Ti alloys indicates that no single-phase alloy of γ-U was present up to 18.8 at.% Ti [116]. Later investigation of the U-Ti phase diagram suggests that predominantly α-U based alloys with an admixture of the U_2Ti compound stabilize in slow cooled (with not identified rate) specimens with less than 30 at.% Ti [117, 118].

Comparable more information is available about the formation of the metastable phases in the U-Nb system. It is a less efficient stabilizer of γ-U phase than Mo [119]. On the other hand, in some sense, it is a unique element, because it does not form intermetallic compounds (check U-Nb temperature vs. composition phase diagram on Fig. 4.4 (b)). The phase diagram also indicates that there is complete solubility of Nb in γ-U phase at high temperature (similar to U-Ti system, Fig. 4.4 (a)). At room temperature equilibrium U-Nb alloys exhibit a mixture of orthorhombic α-uranium and γ phase over a wide composition range. This mixture typically has poor mechanical and corrosion properties [120]. According to Kelly for U alloyed by 14 at.% of Nb onset of the equilibrium phase formation can be bypassed applying cooling rate of 20 K/s. It results in the formation of α″ martensite (which is α phase with monoclinic distortion) [121]. Same composition alloy produced by centrifugal atomization process led to stabilization of the γ^0 phase with admixture of metastable α'' or α' modification (α' suffers contraction of *b* compared to lattice parameters of the equilibrium α phase) [122]. Similar results were also reported for the water quenched alloys with 14 at.% of Nb [123, 124]. According to the investigations of U-Nb system the border between the composition region where modifications of α or γ dominate the alloy content lies around 16 at.% [125, 126]. Retention of γ phase solid solution was reported for the alloy with 21.2 at.% of Nb [127].

An overview of the U-Ti and U-Nb alloys studies indicates that these materials were not studied within one technological scheme (applying the same cooling technique for alloys with different elemental composition). Investigation performed by Tangri (0-18.5 at.% Nb alloying [126]) and by Buzzard (0-30 at.% Ti alloying [116]) also lack analyses of microstructure by means of modern techniques like SEM (EDX, EBSD). In these work the question of crystal structure and microstructure of the alloys will be studied along with the investigation of the transport and magnetic properties. U alloys with 5, 10, 15, 20, 25, 30, 50 at.% Ti and 10, 13, 15, 17, 20 at.% were prepared by ultrafast cooling technique, which is described later. Later, it will be shown that the technique allows stabilizing the desired *bcc* structure of U while reducing the necessary concentration of the transition element.

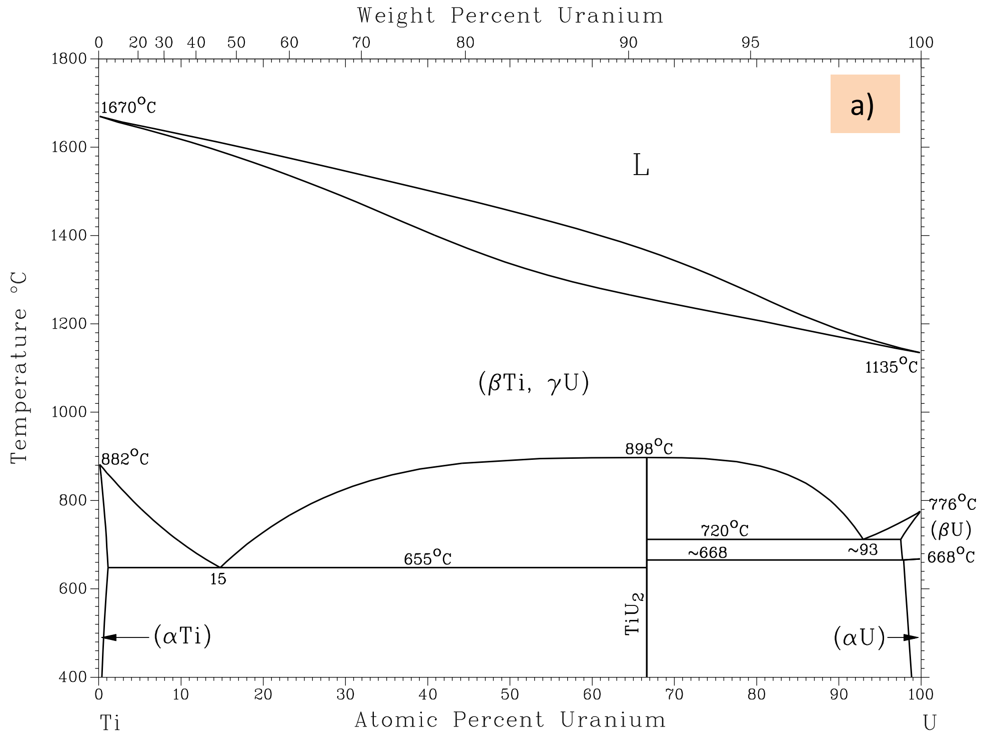

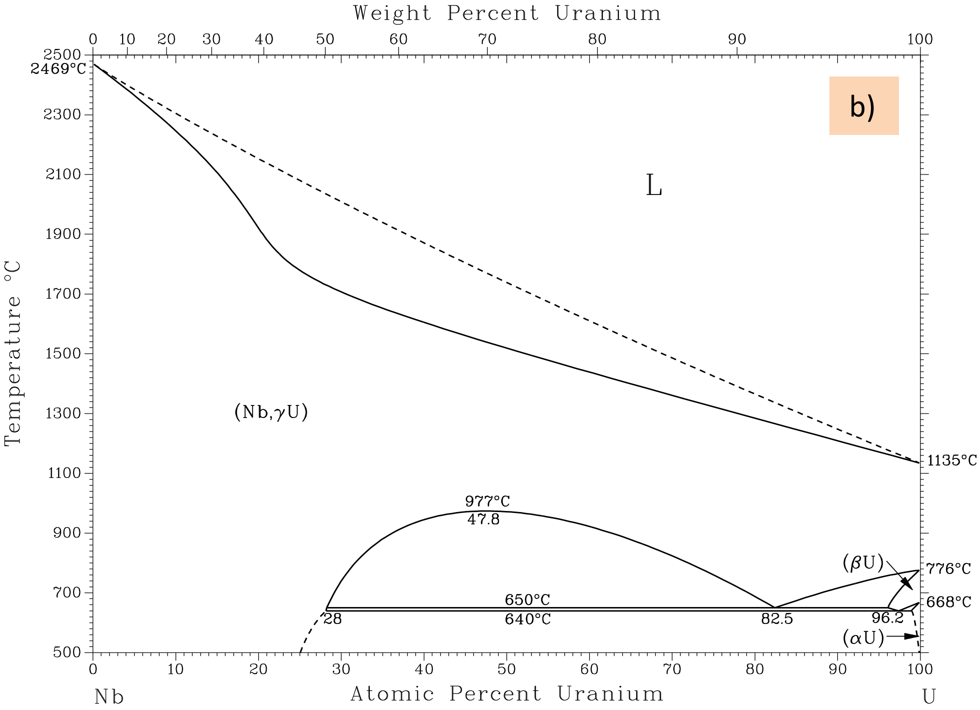

Fig. 4.4 Phase diagrams of the U-Ti (a) and U-Nb (b) systems.

5. Interaction of metals with hydrogen

From the perspective of fundamental physics hydrogen is an efficient crystal and electronic structure modifier. Hydrogenation frequently leads to lattice expansion and structural modifications, which can dramatically change magnetic and transport properties. α-$U_2Co_2SnH_{<0.1}$ and β-$U_2Co_2SnH_{1.4}$ are examples that can give a good feeling of the possible changes. The first compound exhibits ferromagnetic transition with Curie temperature $T_C = 33.5$ K, while the second one orders antiferromagnetically with Neel temperature $T_N = 27$ K [128]. This system also highlights the fact that metal hydrides can exist over a broad range of nonstoichiometric composition.

5.1. Basic principles of the hydride formation

The term “hydride” can refer to two different forms of materials: 1) a solid material with random distribution of small amount of H atoms, also denoted as α-hydrides and can be called disordered hydrides; 2) materials with a sub-system of H atoms which systematically occupy crystal sites defined by certain symmetry operations. This section discusses mainly the second form of hydride, typically β-hydride, here we call it “ordered hydride”.

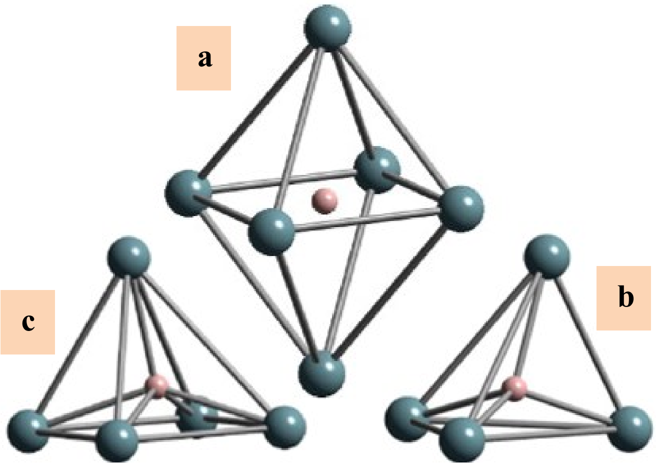

Fig. 5.1 (a, b) – octahedral and tetrahedral interstitial sites usually occupies in hydrides; (c) - square-pyramidal site [129].

The process of the formation of the ordered hydride involves the following phenomena: 1) surface phenomena (mass transport and dissociation of H_2 molecule on the surface with subsequent absorption in bulk), 2) transport (diffusion to the trap sites for saturation), 3) trapping, 4) saturation and, finally, 5) phase transformation. More details about the individual steps can be found in [129, 130]. After the phase transformation H atoms occupy interstitial sites of the lattice, therefore such materials are sometimes denoted as interstitial alloys [131]. In practice, only two types of interstitial sites (octahedral (O) and tetrahedral (T)) are occupied by H in the most common crystal structures (*fcc*, *hcp* and *bcc*).

There is not much experimental evidence about the location of H in the lattices of the U allotropes, therefore theoretical studies serve for development of certain feeling of possible structural changes. Orthorombic α-U also provides O and T sites for the allocation of hydrogen. These interstitial sites are presented in Fig. 5.1 (a, b). In the case of α-U they exhibit significant site anisotropy. Elongated octahedral site has height/width ratio of 1.34, while regular octahedral display 0.71. Taylor indicates that DFT calculations reveal an optimal U-H bond length of 2.1 Å, it can be approached when symmetry breaking of the octahedron into square-pyramidal (see Fig. 5.1 (c)) sites is performed [129]. On the other hand, mentioned study stressed out that in α-U the tetrahedral sites are preferable for hydrogen occupation. DFT study of hydrogen absorption on γ-U (100) surface reveals that tetrahedral site is the most stable interstitial site, it has absorption energy of 1.534 eV, for octahedral sites it is 0.534 eV lower [132]. The presented studies indicate that in the respect of hydrogen accommodation *bcc* structure of U is similar to the orthorhombic one.

It is also important to highlight that α-hydrides based on α-U and γ-U filled with hydrogen are not relevant in this study. Experimentally determined solubility of H in α-U (0.2 ppm) is significantly lower than the concentration which corresponds to the 1U to 3H ratio observed in UH_3 allotropes (≈12.5 ppm) [130]. In order to accommodate that large number of H atoms α-U and γ-U structures undergo structural changes that lead to considerable modification of the physical properties. Possible scenarios of the transformation were studies in the following works [129, 130, 132, 133, 134, 135].

5.2. Uranium hydrides

There are two structural forms of UH_3: α-UH_3 and β-UH_3. Both of them exhibit cubic symmetry. Primitive cubic lattice of α-UH_3 has two UH_3 formula units per unit cell. The crystal structure of α-UH_3 is formed by the 60% expanded *bcc* lattice of U atoms (enlarged γ-U phase) with lattice parameter a = 0.416 nm and the shortest inter U distance $d_{U\text{-}U}$ = 0.360 nm (space group *Pm-3n*, Fig. 5.2 (c, d)). Unit cell of β-UH_3 contains eight U atoms and a = 0.663 nm ($d_{U\text{-}U}$ = 0.330 nm). This structure is more complicated, there are two types of U atoms: two U atoms in (0,0,0) and (1/2,1/2,1/2); and six U atoms in ±(1/4,0,1/2) [136] (space group *Pm-3n*, Fig. 5.2 (a, b)). In α-UH_3 and β-UH_3 each U atom is surrounded by 12 nearest H atoms located at a distance of 0.232 nm [137]. In the Fig. 5.2 selected tetrahedra occupied by H atoms are highlighted.

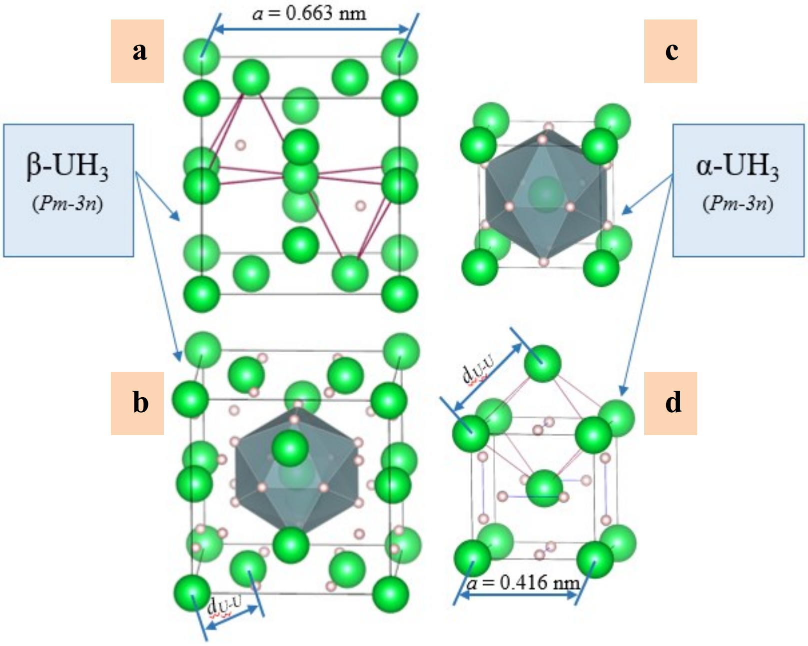

Fig. 5.2 (a, b) – crystal structure of β-UH_3 with highlighted interstitial sites and icosahedra formed by 12 H atoms (on a only H atoms from the highlighted tetrahedrons are shown); (c, d) – analogous representation of α-UH_3.

Until recently, α-UH_3 was not synthesized in pure form. It was considered as an intermediate phase that appears during the transformation from α-U to β-UH_3. Mulford stated that it can be stabilized at a low temperature. The hydride produced at -80° C contained a mixture of two hydride forms (α-UH_3 content estimated to be equal to 50%) [138]. High-pressure hydrogenation of γ-U alloyed by Zr allowed stabilizing the proper structure at room temperature [45]. This is contrasting with the behavior of uranium metal, which can react with hydrogen even at gas pressures as low as 500 Pa and 30° C producing β-UH_3 [139]. Pressure vs. composition isotherm of the α-U-UH_3-H system pointed out the possibility of H deficiency in β-UH_3, as this phase exhibits temperature-dependent stoichiometry, which can be reflected in the formula UH_{3-x} (at room temperature x = 0) [130]. It can be summarized that crystal structure of the obtained hydrides depends on thermodynamic conditions (pressure, temperature), parent compound and its chemical composition.

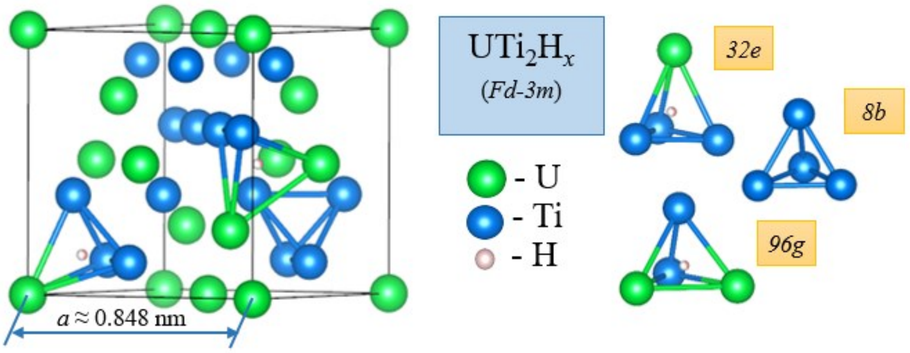

Fig. 5.3 Cubic Laves phase structure (also called C15 structure) with the highlighted interstitial sites of three types. The hydrogen atoms are shown only in the occupied interstitial type.

Hydrides with the cubic Laves structure is another form of hydride deserving attention. Except being oxidation and creep resistant, this structure provides fast hydriding-dehydriding kinetics and a high hydrogen capacity [140, 141]. AB_2 is the general formula used for representation of Laves compounds (AB_2H_x correspond to hydride). In the cubic allotrope there are three types of tetrahedral interstices available for hydrogen (by Wyckoff position): one 8*b* (H surrounded by 4 B atoms), four 32*e* (AB_3) and twelve 96*g* (A_2B_2) (present on the Fig. 5.3). Centers of the neighboring tetrahedra are less than 0.16 nm apart, electrostatic forces lead to the occupation of the sites which do not share triangular faces (located at least 0.2 nm apart). Thus, the theoretically estimated maximum sorption is 6 H atoms per formula unit AB_2 [142]. Some alloys exhibit event higher value, for instance, *bcc* $ThZr_2$ alloy allows formation of Laves hydride with H content spanning a broad range of $1.8 \leq x \leq 6.7$ [143].

Some authors suggested presence of the Laves-type hydride in the U-Ti-H phase diagram [144, 145]. In fact, as U_2Ti (structure type AlB_2, sp. gr. *P6/mmm*) is the only intermediate phase in the U-Ti phase diagram, it highlights the role of hydrogen in the stabilization process. On the other hand, during hydrogenation free energy of the formation of binary hydride from the alloy is usually more favorable than the formation energy of a ternary hydride. In most of the isolated experimental cases due to kinetic limitations ternaries form at temperatures which are lower than for binary hydrides. At high temperature the thermodynamic barrier for the most stable phase should be reduced resulting in decomposition of the ternary to a binary hydride [146].

Nevertheless, hydrogenation of U_xTi_{1-x} alloys can produce a structure which corresponds to cubic Laves allotrope of $MgCu_2$ type. In the discussion of the experimental results it will be shown that U-Ti system is a good example that presents the chemical and temperature dependence of the structure modifications due to hydrogenation.

6. Experimental

6.1. *Sample preparation*

This section provides information about the methods of syntheses and physical characterization which were applied throughout the experiments. Two different forms of alloys were used for preparations of the studied hydrides: 1) as cast material in the form of a spherical button – product of the monoar furnace; 2) ultrafast cooled alloys in the form of splats (thin foils produced in splat cooler, described below).

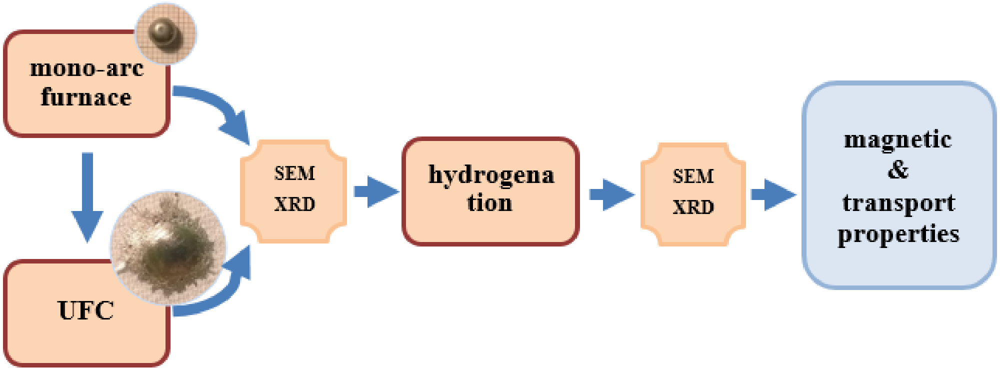

Fig. 6.1 Life-time of a typical studied sample. UFC – ultra-fast cooling; SEM – investigation of the surface by means of scanning electron microscope; XRD – x-ray diffraction analysis.

6.1.1. Arc furnace

Production of the alloys with the desired concentration of U, Ti and Nb was performed using an arc furnace. The device melts purified metals by an arc discharge under argon atmosphere. The main advantages of this type of furnace are: 1) materials with a high melting point can be processed; 2) a very clean atmosphere can be achieved with high-vacuum pre-pumping and pure Ar gas; 3) it is easy to maintain the operational state of the system; 4) a set of crucibles allows to produce alloys with different shape profiles (spherical, rod).

The main components of the arc furnace (also called non-arc) are: 1) vacuum system with turbomolecular and scroll pump; 2) water-cooled copper crucible; 3) W arc electrode; 4) power supply; 5) chamber. The usual operational process included evacuation down to 0.2 Pa. At sufficiently low pressure the chamber degases with the support of heating. Then Ar is loaded to pressure of ≈ 60 kPa. This pressure allows the ignition of the arc, which is supplied by a DC welding power system. Alloys with different masses can be produced using the arc furnace. For the subsequent splat-cooling, samples with masses m = 0.3-0.6 g were produced. There is no restriction for mass of the samples which were hydrogenated without the intermediate step of ultra-fast cooling. The system is shown in Fig. 6.2.

Fig. 6.2 Arc furnace with the crucible.

6.1.2. Splat cooling

Earlier in the text it was shown that the cooling rate influences both phase composition and microstructure of the processed materials. Techniques which were used in the previous studies of the U based alloys had several disadvantages. U is easily oxidizing, therefore it is important to maintain a proper vacuum or inert atmosphere during casting/quenching. In this sense, water, air and steam quenching represent a risk. At the department of Condensed Matter Physics, the splat cooling technique has been adapted for high-vacuum treatment (produced by Vakuum Praha), see Fig. 6.3.

This system allows reaching the cooling rate of 10^6 K/s. In principle, it is also an arc-melter. The main functional elements of the system are following: electrode, vacuum chamber, water-cooled copper crucible, copper anvils, power supply and infrared detector. Due to high thermal conductivity of the copper anvils and instant melt quenching, splat cooling provides cooling rates sufficient for preparation of the high-temperature phases [62, 90, 147], amorphous materials (glassy metals) and high entropy alloys. The other advantage of the system is the possibility to perform quenching in an argon atmosphere.

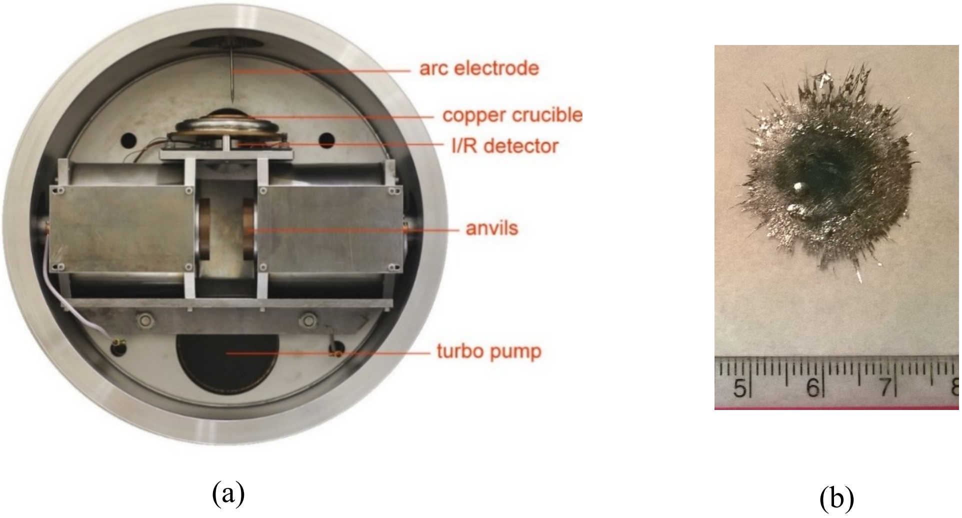

(a) (b)

Fig. 6.3 (a) – opened chamber of the splat cooling system; (b) – a typical product of the quenching (splat).

The chamber can be evacuated below the pressure of 3 Pa, argon atmosphere of 50 kPa is provided before melting/quenching. Alloy is melted by electrical arc. The melt drops through the hole in copper crucible. Infrared photoelectric switch detects the fallen droplet and initiates movement of two anvils. The anvils squeeze the droplet resulting in samples that usually have an irregular disc shape with a diameter of about 20 mm and a thickness of 100 - 200 μm Fig. 6.3 (b).

U with 5, 10, 15, 20, 25, 30, 50 at.% Ti alloys and 10, 13, 15, 17, 20 at.% Nb were produced by means of the splat cooling system. For synthesis we have used natural U with 2N8 purity and Ti (Nb) with 4N purity.

6.1.3. Hydrogenation equipment

From the end of the 20th century, the portfolio of actinide materials studied at the Faculty of Mathematics and Physics included also metal hydrides. Construction of the dedicated hydrogenation equipment stimulated the development. The system consists of two branches, the first branch is used for hydrogenation, while the second branch designed for desorption experiments, which help to determine the absorbed gas concentration (see Fig. 6.4 (a)).

The hydrogenation branch contains the following functional elements: 1) solid-state hydrogen (deuterium) storage realized on the basis of $LaNi_5$; 2) a set of pressure gauges which allow covering the pressure range from $5*10^{-6}$ Pa (with cold cathode gauge from Pfeiffer Vacuum) to 15 MPa (with high-pressure piezoelectric sensor); 3) resistance heaters which allow setting the reactor temperature in the range from RT (room temperature) to 850ºC. The detailed scheme of the hydrogenation branch is presented on Fig. 6.4 (b).

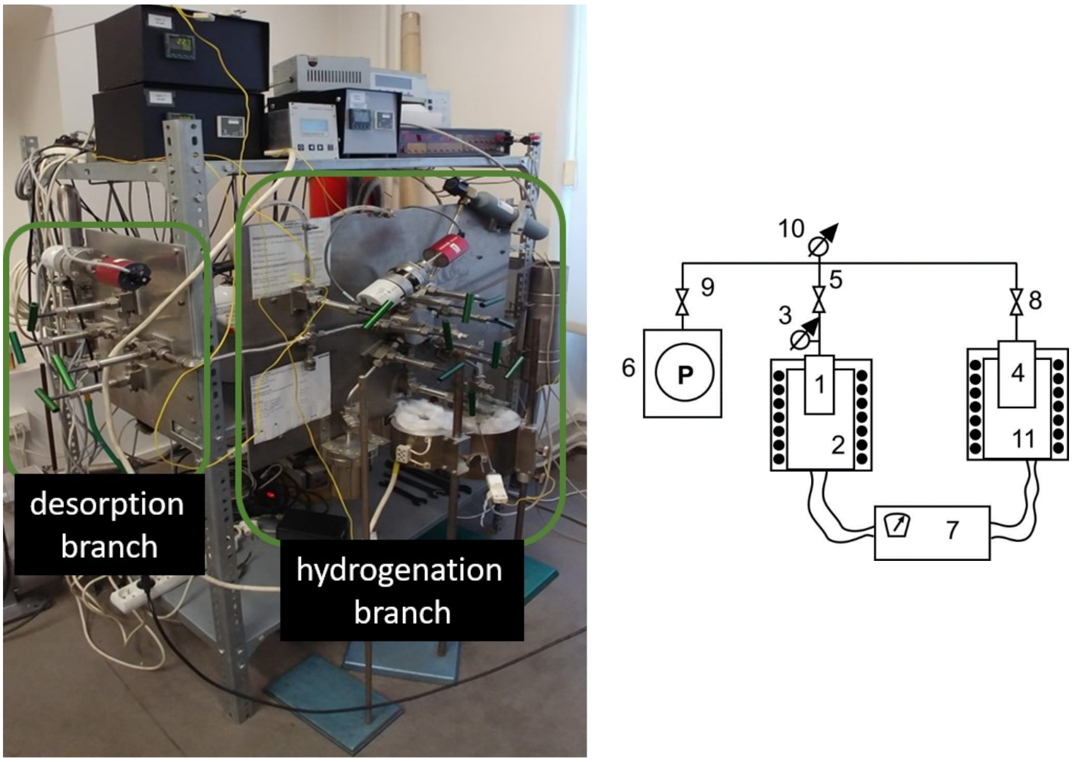

(a) (b)

Fig. 6.4 (a) - hydrogenation equipment; (b) - schematic representation of the hydrogenation branch: 1 – reactor; 2, 11 – heaters; 3, 10 – vacuum gauges; 4 – $LaNi_5$ container with H_2; 5, 8, 9 – valves; 6 – vacuum pumps; 7 – temperature control unit.

We used two different approaches for hydrogenation of the alloys in the present work. The phase composition and shape (bulk, splat) represent the factors that determine the choice between them. The common procedure included sample preparation (weighted amount of the material should be inserted in the reactor) and evacuation down to 1 Pa. Then different temperature treatment and hydrogen pressure was used for different materials.

6.1.3.1. Hydrogenation of the *bcc* U-(Ti, Nb) alloys

There is no available phase diagram for the *bcc* U-(Ti, Nb) alloys and hydrogen. In [45] and [47] authors indicate that irrespective of composition hydrogenation of the *bcc* U alloys with Mo and Zr requires minimum H_2 pressure in the range 0.4–0.5 MPa. Higher pressures (10 MPa) speeds up the process, but the absorbed H amount remains the same. For hydrogenation of the *bcc* U alloys with Ti and Nb the gas pressure equal 10 MPa was used. The main purpose of this process was the study of the hydrogenation products obtained from γ-U alloys. Heat treatment leads to decomposition, therefore alloys were not activated (heated in vacuum) before hydrogenation. Room temperature hydrogenation was the usual procedure performed for γ-U alloys. It typically leads to the formation of brittle hydride lamellae, which are shown on the Fig. 6.5 (f).

6.1.3.2. Preparation of the UTi_2H_x hydrides

Formation of UTi_2H_x requires, on the other hand, high temperatures. The first indication of the conditions which can favor its stabilization appears in the paper of Yamamoto [148], nevertheless, the technology which can be used for the production of the UTi_2H_x with Laves structure was not clear. For this study, hydrogenation of the bulk alloys with different concentrations of Ti was performed by exposure of a hot specimen to H_2 gas atmosphere. Different temperature treatment procedures were undertaken yielding hydrides based on the alloys with the following compositions: 1) $U_{0.70}Ti_{0.30}$ – two different hydrides; 2) $U_{0.34}Ti_{0.66}$ – three different hydrides; 3) $U_{0.20}Ti_{0.80}$ – one hydride. The reason for the complicated scheme is that the production of the desired UTi_2H_x phase is rather tricky and the best route had to be identified through the production of the hydrides at different conditions. During technological experiments, it first became apparent that the phase can form only at H_2 exposure at high temperatures. However, further details of synthesis play a role, and the sequence of pressure and temperature reduction at the end can change a lot.

The different hydrogenation routes were also giving different forms of the products:

1) If the $U_{0.70}Ti_{0.30}$ alloys was hydrogenated at room temperature and a hydrogen pressure of 8 MPa for 48 hours, the bulk piece was disintegrated into small fragments – Fig. 6.5 (a).

2) Next the same $U_{0.70}Ti_{0.30}$ alloy was hydrogenated at $T = 973$ K starting from 30 kPa, then pressure was increased to 0.1, 0.5, 1 and 7 MPa, each pressure was maintained for 24 hours. The bulk specimen was broken into compact pieces – Fig. 6.5 (b).

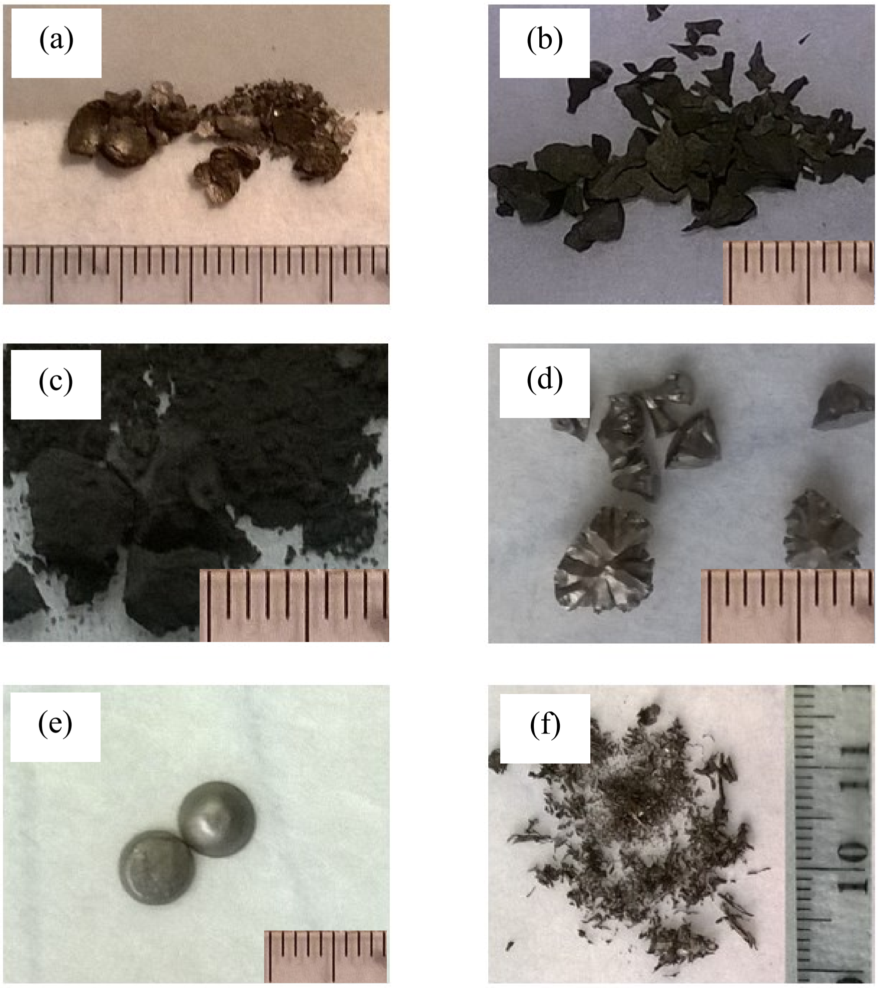

Fig. 6.5 U-Ti hydrides produced at different temperature and pressure conditions: a and b – hydrides produced from the $U_{0.70}Ti_{0.30}$ at high and low temperature respectively; c – hydride produced from the (I) $U_{0.34}Ti_{0.66}$ alloy without quenching from high temperature; d – quenched hydrogenated (II) $U_{0.34}Ti_{0.66}$ (high pressure); e – quenched (III) $U_{0.34}Ti_{0.66}$ alloy hydrogenated at high temperature (low pressure); f – product of splat hydrogenation performed at room temperature (high pressure).

3) The first (I) $U_{0.34}Ti_{0.66}$ alloy was hydrogenated at 0.45 MPa and 973 K. After 110 hours the temperature was slowly reduced down to room temperature. The hydride had a form of a very fine powder – Fig. 6.5 (c). It is a result of sample decomposition into different phases of Ti-H and U-H hydrides.

4) For the second (II) $U_{0.34}Ti_{0.66}$ ingot, the H_2 pressure was ramped up to 7.3 MPa at $T = 973$ K. After the 68 hours of hydrogenation the reactor was rapidly cooled down to room temperature and the pressure was slowly lowered to 30 kPa. Hydrogenation resulted in the dissociation of the bulk into smaller pieces Fig. 6.5 (d).

5) Hydrogenation of the third (III) $U_{0.34}Ti_{0.66}$ ingot was performed at 0.54 MPa H_2, after 24 hours hold at 973 K the temperature was reduced (with 0.1 K/min) down to 893 K, where it was held for 25 hours. Still, at high temperature, the pressure was reduced down to 30 kPa and the sample was quenched. The sample remained monolithic in this case, without any visible cracks. The sample changed visually, the original silver luster turned into a grey hue Fig. 6.5 (e).

6) Hydrogenation of the $U_{0.20}Ti_{0.80}$ was conducted at $T = 973$ K, the pressure was sequentially increased from 60 kPa to 0.6 MPa (0.1 MPa and 0.3 MPa – intermediate steps). Before quenching the sample was held at 923 K and 833 K (24 hours at each temperature point). The surface of the hydrogenated alloy exhibited cracks, it can be a result of the heat treatment performed in the end of the procedure.

Detail description of the phase compositions of the hydrides obtained via different routes will be shown later.

6.2. Sample characterization

6.2.1. Determination of the crystal structure of the U-(Ti;Nb) alloys and hydrides

Diffraction and interference of the electromagnetic radiation is the basic phenomena that underline the investigation of the materials crystal structure (crystallography). In the sense of diffraction, X-ray have the proper wavelength to be used for investigation of the solid matter. From the basic course of physics, we know that diffraction can be observed when the wavelength of the radiation is comparable to the distance between the scattering centers (interatomic distance). In crystallography, usually used wavelength range between ≈ 0.5 Å and 2.5 Å.

Solid matter can be described as parallel atomic planes with identical triplets of Miller (*hkl*) indices which are equally spaced. W.H. Bragg treated reflection from the atomic planes as mirror reflection of the incident x-ray beam. Therefore each set of *hkl* planes can be considered as a separate scattering object which is characterized by the interplanar distance d_{hkl}. Bragg introduced convenient relationships between the diffraction angle (Bragg angle), wavelength and interplanar spacing. Constructive interference of the waves scattered from different planes of a set occurs when the phase difference (Δ) for the waves equals $2\Delta=n\lambda$, where $\Delta = d_{hkl}sin\Theta$ (see Fig. 6.6). The usual form of the Bragg equation is: $n\lambda =2d_{hkl}sin\Theta$. Atomic positions of material can be found from the diffraction patterns, which contain information about intensity of the scattered radiation as a function of Bragg angle. Nevertheless, it is important to mention that real photon scatterers are electrons (or electron density of an atom), that is why angle dependent atomic scattering efficiency is an important component intensity moderator.

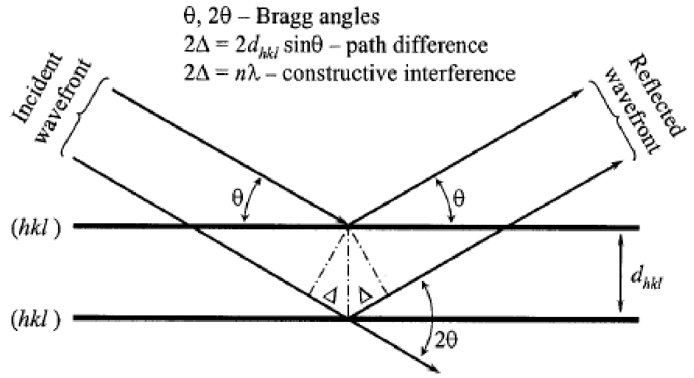

Fig. 6.6 Schematic representation of the electromagnetic radiation scattering with the condition of constructive interference [149].

Investigation of the crystal structure was performed by means of the X-ray powder diffractometer Bruker D8 Advanced with Cu K_α radiation. The goniometer of the diffractometer is equipped with high precision stepper motor which is insured by the optical encoders. D8 Advanced is constructed according to the Bragg-Brentano geometry which achieves high diffracted intensity without loss in resolution – see Fig. 6.7. The advantages rise as a result of the diffraction beam parafocussing.

There are three different specimen shapes which were studied with the diffractometer: splat, bulk ingots and powder. Uranium splats and bulks are hard materials, therefore it was not possible to crush them into powder. It is the main reason why the materials structure measurements were performed on the surfaces (see Fig. 6.8). The bulk ingots were cut into half, before the measurement cut surface was polished by SiC grinding papers). This approach leads to the observation of preferred orientation, in the case of low symmetry structures (for instance, orthorhombic) it complicated determination of the lattice parameters. More details are given in the result section.

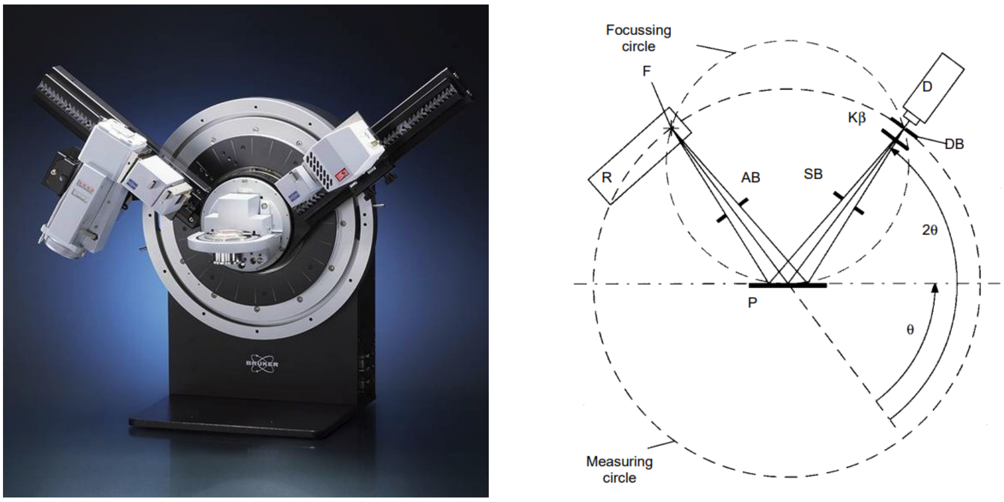

(a) (b)

Fig. 6.7 (a) goniometer of the Bruker D8 Advanced; (b) – beam path of the diffractometer, where: AB – aperture slit, D – detector, DB – detector slit, F – focus, P – sample, R – X-ray tube, SB – scattered radiation slit.

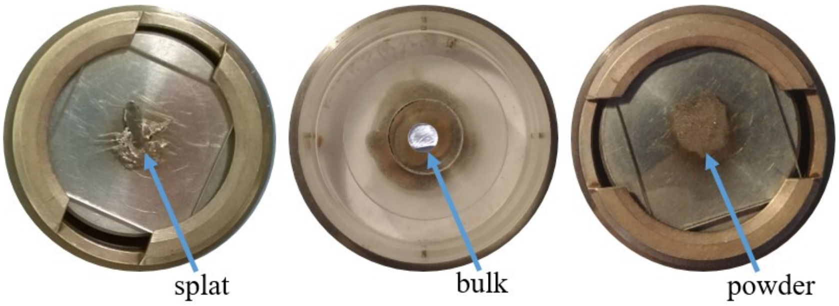

Fig. 6.8 Sample cups with different specimen shapes.

6.2.2. Investigation of the microstructure and grain orientation distribution

6.2.2.1. Description of the SEM techniques

Modern investigation is characterized by a thorough investigation of all details which can influence material properties. The microstructure is an important piece of a physical puzzle. From the perspective of this study, knowledge of the microstructure helps to understand mechanical properties, corrosion behavior, along with transport properties. Material scientists developed a number of techniques for sample characterization. In the middle of 20th century people studied microstructure by means of polarized light microscopy. It was a useful tool for differentiation between different phases and precipitates [150, 107]. Nevertheless, optical investigations do not give fundamental reasons to rely on their results.

Now, capabilities of the contemporary scanning electron microscopes (SEM) allow precise determination of the chenical composition, morphology, distribution of the chemical elements and distribution of crystallographic orientations on a surface. This information can be obtained from the analyses of the results of elastic and inelastic electron scattering data. There are three main ingredients that carry the information: 1) backscattered electrons (BSE); 2) secondary electrons (SE); 3) characteristic x-ray radiation.

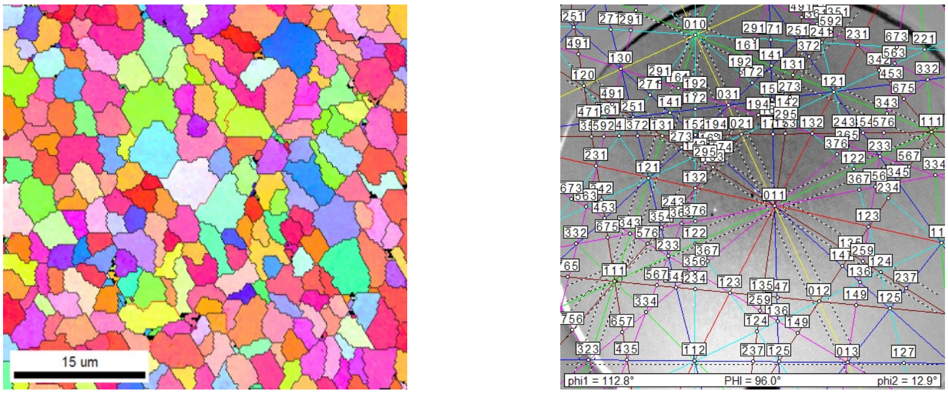

(a) (b)

Fig. 6.9 (a) - crystallographic orientation map of the splat-cooled U-12 at.% Mo alloy. EBSD mapping revealed only γ-U phase and UC (small black areas). (b) - Kikuchi pattern collected from the UC region.

BSE – high energy electrons (E>50 eV) which are elastically scattered with an angle which exceeds 90º. Scattering efficiency of chemical elements increases with the increase of atomic number *Z*, therefore BSE are used to detect compositional contrast, special configuration of a detector allows to detect topographical information. The most interesting piece of information which can be retrieved from the elastic electron scattering is the orientational map obtained from Back Scattered Electron Diffraction, EBSD. Angular resolution of the current devices allows distinguishing orientation of 20 nm grains [151]. Electron diffraction requires a highly polished sample surface. It is oriented at a shallow angle of 20º with regard to the electron beam (acceleration voltage 10-30 kV, beam current of 1-50 nA). Special computer software performs analyses of the obtained Kikuchi patterns, it determines the best orientational fit taking into account possible orientations and parameters of the considered phase [152]. Consequently, EBSD allows obtaining phase and distribution map. Fig. 6.9 shows an example of an EBSD crystallographic orientation map collected from the splat-cooled U 12 at.% Mo splat.

SEs occur as a result of the ionization of the specimen atoms. They have low energies ($E < 50$ eV) and originate from a surface/subsurface region. Therefore SEs provide detail topographical information of a specimen. Comparison of the images produced from the BSE and SE analyses helps to understand the origin of the microscopical features, topological effects can be distinguished from the composition ones, see Fig. 6.10 (a, b).

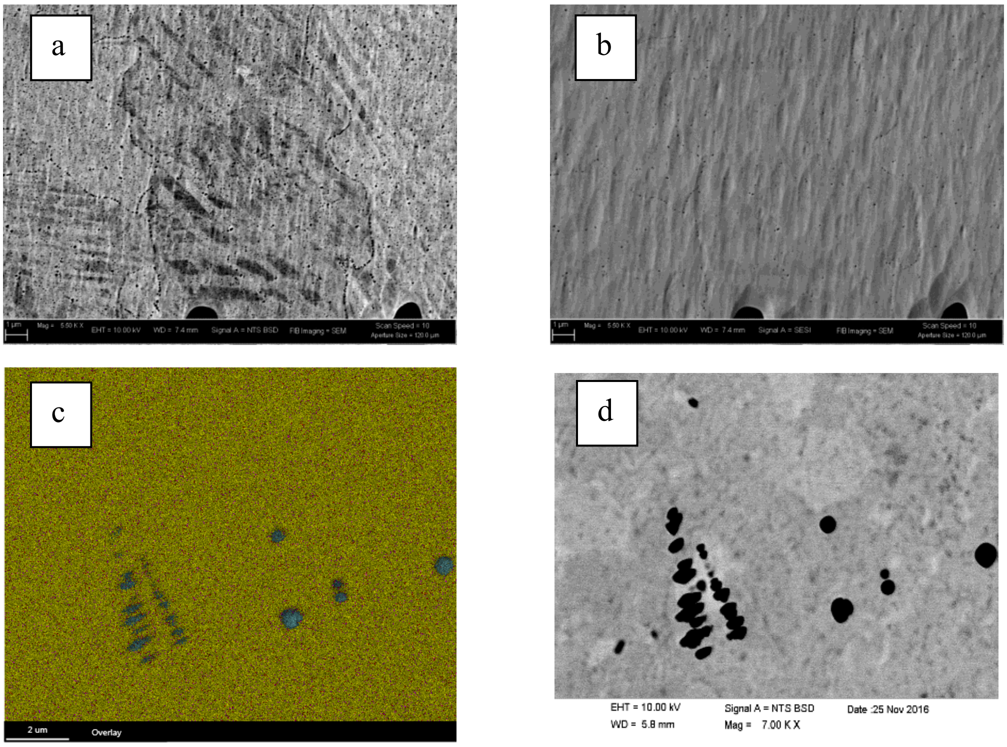

Fig. 6.10 Comparison of the BSE (a) and SE (b) images obtained from the surface of the U-15at.%Ti alloy with 10kV electron beam. (c) EDS map of Ti (blue, K electron edge) and U (yellow, M edge) compared with the BSE image of the same region (d).

Qualitative studies also require information about the homogenous/inhomogeneous distribution of elements on a surface (chemical characterization). Energy dispersive spectroscopy (EDS) is the usual technique used for such purpose. Interaction of the electron beam with electrons leads to emission of characteristic X-ray photons with element-specific energies, which allows performing elements mapping. There are a number of factors that influence estimate of the relative abundance of different elements in the material:1) overlapping X-ray emission peaks; 2) radiation energy; 3) composition; 4) nature of the sample; 5) density. The application of a quantitative correction procedure improves the estimate of the sample composition. Fig. 6.10 (c, d) presents the BSE picture (c) and EDS map (d) obtained from the same surface region. It shows that black inclusions from Fig. 6.10 (d) correspond to Ti-rich segregations (blue) which are distributed in the U-Ti medium.

6.2.2.2. Surface preparation and study

SEM studies of uranium-based alloys is complicated due to surface oxidation. Some alloying elements improve resistance against oxidation, nevertheless, preparation of the samples requires patience as well as creativity. The usual procedure which was used for U-Ti and U-Nb alloys is grinding in ethanol with different grit size SiC paper (800, 1200, 2000, 4000). The following step is mechanical polishing with ethanol-based lubricant together with standard commercially available diamond abrasive suspensions (3 μm and 1 μm, starting from the coarse one). This technology allows obtaining sufficient surface quality for the regular BSE/SE/EDS analysis.

The problem is persisting for EBSD. Even thin surface layer of oxide prevents observation of EBSD patterns, therefore more advanced techniques have to be applied in the case of uranium-containing samples. There are three approaches which were tested on U-Mo and U-Nb samples: 1) ion milling in the Gatan PIPS (Precision Ion Polishing System); 2) electrochemical polishing by ElectroPol – 5 by Struers (different alloying require specific etching solution); 3) ion milling by FIB (focused Ion Beam) [153]. Investigation of the U-15at.%Nb, U-15at.%Mo, and U-4at.%Mo splats allowed authors to conclude that PIPS is convenient for the alloys containing mainly γ-U phase (U-15at.%Mo). Transfer of the sample through air did not lead to the formation of oxide which would prevent electron diffraction, sufficient quality EBSD image was formed. Alloys with α or matrix of α+γ require different preoperational route, consisting in combination of electrochemical polishing, giving a smooth surface, and in-situ Focused Ion Beam (FIB) milling using Ga ions.

A similar procedure was used for the U-Ti and U-Nb alloys, which exhibit γ-U phase. The specimens for the EBSD measurements were prepared by grinding and polishing down to 0.25 μm diamond paste, followed by ion beam polishing using a Leica EM RES102 system. The metallographical study of the specimens was then carried out immediately to avoid oxidation effect on the prepared surface. Microstructure analysis was carried out using the Cross Beam SEM Zeiss Auriga with field emission gun (FEG), FIB and equipped by EDAX/TSL EBSD system. The orientation patterns were collected with a step size of 0.1 μm and at the acceleration voltage of 10 kV. Detail analyses will be given in the results and discussions.

6.3. Studies of the physical properties

6.3.1. Heat capacity

Knowledge of the temperature dependence of specific heat (heat capacity) is useful for the interpretation of material properties. It is used for the identification of phase transitions of various orders, which give pronounced anomalies in $C(T)$. The Sommerfeld coefficient of electronic heat capacity, a parameter which can be extracted from the $C(T)$ data, allows to quantify the electronic density of states (DOS) at the Fermi level, closely related to many physical properties (magnetic, transport, etc.). At present heat capacity can be easily measured on the samples which have mass of the order of milligrams, using the microcalorimetry technique, based on a relaxation method. The Quantum Design Company developed a technique that allowed automated measurement of specific heat within the Physical Property Measurement System (PPMS). Accurate investigation of the small specimens was insured by the comparison with conventional relaxation calorimeter based on the Bachmann approach [154].

PPMS heat capacity system controls added and removed heat while monitoring the following sample platform temperature changes. In other words, during equal time sample undergoes heating and cooling. Each heating-cooling cycle is followed by a robust fitting of the temperature response of the platform.

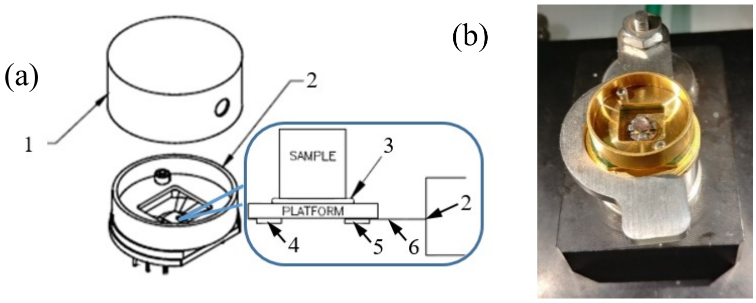

Fig. 6.11 (a) – schematic representation of the PPMS heat capacity puck [155]: 1) thermal radiation shield; 2) thermal bath (puck frame); 3) apiezon grease; 4) thermometer; 5) heater; 6) connection wires. (b) – heat capacity puck with $(UH_3)_{0.70}Ti_{0.30}$ bulk piece mounted on the sample platform (it was obtained from hydrogenation of a bulk sample).

The fitting "two-τ" model takes into account: 1) thermal relaxation between sample platform and sample; 2) relaxation between sample platform and sample bath (a scheme of the PPMS heat capacity puck is presented on the Fig. 6.11 (a)). Simulation of the platform-sample and sample-puck heat exchange is performed using the following formulas [155]:

$$C_{platform}\frac{dT_p}{dt} = P(t) - K_w\left(T_p(t) - T_b\right) + K_g\left(T_s(t) - T_p(t)\right)$$

$$C_{sample}\frac{dT_s}{dt} = -K_g\left(T_s(t) - T_p(t)\right)$$

Specific heat was measured for samples with different shapes: 1) splats – ultrafast cooled alloys; 2) bulk specimens – as-cast alloys; 3) hydrides. The sample masses which were used for studies range between 5 mg and 35 mg which is appropriate for the PPMS heat capacity option (from 1 to 200 mg). A small amount of Apiezon grease has been used to ensure good thermal contact between the heat capacity platform and sample.

6.3.2. Magnetic properties

Investigation of magnetic properties of hydrides and alloys was performed by ACMS option of PPMS and MPMS (magnetic property measurement system). Both systems allow to measure magnetic susceptibility in the temperature range of 2-400 K. MPMS with extraction options and 7 T superconducting magnet was used for DC investigation of the temperature dependences of $\chi(T)$ (in other words, magnetization

$M(T)$). It provides the highest detection sensitivity over the whole temperature range with capability of resolving magnetic field changes in the order of 10^{-15} T. This sensitivity is due to the SQUID sensing device based on two Josephson junctions. Studies of magnetic hysteresis were carried out by means of the ACMS option of PPMS equipped with 9 T and 14 T superconducting magnets. These devices were also used for the study of the AC susceptibility, which yields information about the magnetization dynamics.

Determination of the magnetic moment for the ACMS and extraction MPMS options are based on the same physical principle – Faraday law. Drive motors oscillate the sample near a detection coil, the magnetic moment of the sample is proportional to the current induced in the detection coil. ACMS options supports high drive motor speed of 1 m/s which reduces the time required for measurement, that is the main reason why it was chosen for the $M(H)$ measurements. 14 T PPMS is useful for the saturation magnetization test. All of the presented measurements were performed on powder with randomly oriented grains fixed by a glue (this approach was used for hydrides). On the other hand, hard polycrystalline samples were glued directly to the sample holder. Superconducting coils provide a static magnetic field with a maximum value of 7, 9, or 14 T, depending on the system chosen.

6.3.3. Transport properties

Transport properties represent another information channel bringing information on both lattice and electronic sub-system. Electrical resistivity data combined with magnetic and heat capacity generally allow to classify materials into several known groups, as spin-glass, Kondo, Heavy Fermion, non-Fermi liquid, first and second-order superconductors. Thermal conductivity and Seebeck coefficient (thermoelectric power) extend understanding of the mechanisms of heat transport and heat carriers.

Electronic and heat transport were studied for selected hydrides and alloys. The main characteristics of choice is the phase purity. The samples with *bcc* U phase were considered from the perspective of electron transport and appearance/change of the superconducting transition temperature and critical field. Detail study of the transport properties were performed for the bulk hydride with the cubic Laves structure (UTi_2H_5). Thermal transport and thermoelectric power of the hydride were obtained for the broad temperature range (2-300 K).

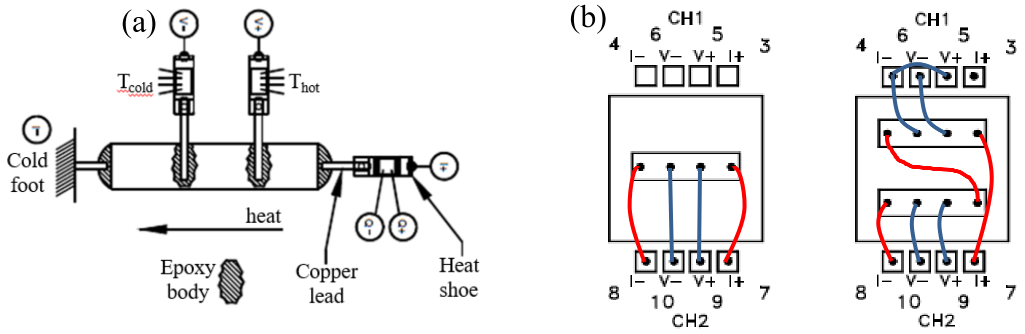

Fig. 6.12 (a) –schematic view of the thermal and electrical connection for the TTO measurement. For Seebeck and thermal conductivity measurement heat is applied to one end of the sample using electrical heated with predefined power. Then measurement of T_{hot} and T_{cold} is performed at respective thermometer shoes. (b) and (c) – schematic view of electrical connections used for ACT and ACT with ^{3}He measurements (red – current contacts, blue – voltage contacts).

Measurements were conducted on the PPMS with thermal transport option (TTO) and AC transport option (ACT). TTO enables simultaneous investigation of the thermal conductivity κ, thermoelectric power α and resistivity ρ. In TTO, the thermal conductivity is dedused from the temperature drop between the heater shoe and cold foot, see Fig. 6.12 (a). In other words, user specified heat pulse is applied from one of the ends of a specimen, in the same time system monitors the temperature difference between the "cold" and "hot" end. TTO calculates the thermal transport from the resulting temperature difference ΔT, applied heater power and sample geometry. The temperature gradient leads to a drop in electrical voltage, which is measured as the Seebeck coefficient.

Electrical resistivity measurement performed by means of the TTO gives results, which are similar to those obtained from ACT. The ACT option was used mainly for the study of the fast cooled samples (splats), it allows to perform the measurement faster. Investigation of the electrical resistivity in the temperature range of 0.4-2 K was performed by the ACT option with ^{3}He refrigerator. TTO and AC transport options measure electrical resistivity with the same high-performance hardware. The precision current source has a resolution of 0.02 μA and a maximum current of 2 A. The voltage detector has similar ranges. The ACT option supplies an AC bias current from 1 Hz up to 1 kHz providing measurement sensitivity greater than the DC instruments (signal filtering can be used).

6.3.4. Studies of ac susceptibility under pressure

The changes of the magnetic properties under pressure were investigated for selected hydride. A convenient technique for determination of the small changes of T_C in a ferromagnet is measurement of *ac* susceptibility, χ_{ac}. It was performed using home-made miniature detection coils (described here [156]). The strength of *ac* excitation field can change to some extent with the geometrical factors inside the cell (dependent on applied pressure), but is approximately 0.5 mT. The pressures were applied by means of two-layered CuBe/NiCrAl pressure cell (C&T Factory Co., Ltd.) with the highest nominal pressure of 3 GPa [157]. Since the pressure-transmitting medium was Daphne oil 7373 [158] the maximum pressure change at the lowest temperature was $\Delta p \approx 0.3$ GPa (for $p<2.5$ GPa) and $\Delta p \approx 0.5$ GPa (for $p>2.5$ GPa) [159]. The pressures were set at room temperature and defined by the thermally stabilized manganin wire.

7. Results and discussion

7.1. Fast-cooled U-Ti and U-Nb alloys

7.1.1. Structure an transport properties of U-Ti and U-Nb alloys

7.1.1.1. Crystal structure and microstructure

In the first part of this section crystal structure and microstructure of the ultra-fast cooled U-Ti and U-Nb alloys are discussed. These alloys were produced by the splat cooler described in section 6.1.2. The high cooling rate (≈10^6 K/s) allows to overcome the formation of equilibrium phases shown in the phase diagram (Fig. 4.4 (a)). Analyses of the diffraction patterns obtained from the surface of the splats indicated that the α-U phase dominates in the alloys with Ti concentration < 15 at.%. The γ-U *bcc* phase dominates for higher Ti concentrations.

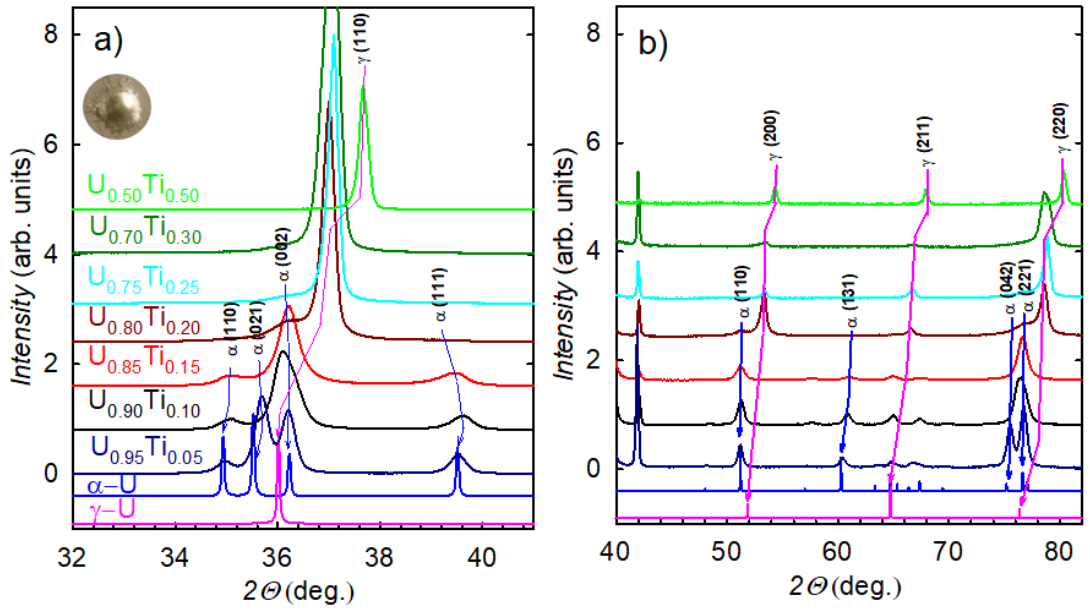

Fig. 7.1 X-ray diffraction patterns of the fast-cooled U-Ti alloys in the concentration range from 5 to 50 at. % of Ti. The left panel (a) presents the details of the diffraction patterns between 32 and 41 deg. On the right panel intensities of the experimental data were multiplied by 5, because intensities of the peaks located between 40 and 82 deg. exhibit significantly lower intensities with respect to the strongest reflection located near 37 deg. Both figures have same colour scheme, where: 1) pink plot corresponds to the calculated structure of γ-U with literature lattice parameter taken from [160]; 2) blue plot represents the α-U structure [161]; 3) the plots starting from the dark blue

represent the experimental data. Progression of the main reflections of the structures is highlighted by the arrows.

Fig. 7.1 (a) demonstrates the concentration variations of main reflections of α-U and γ-U phase. α-U undergoes drastic change of the lattice constant *b* which is already seen in pure U splat. In comparison with the literature data, U splat exhibits 0.041 Å smaller parameter (see Table 4). Structure refinement performed for the $U_{0.95}Ti_{0.05}$ splat results in parameters which are close to the ones observed for the U splat, in respect to the reported data [162] *b* decreases from 5.869 Å to 5.837±0.002 Å. This feature will be addressed later. Further increase of the Ti concentration gives the same trend, thus for $U_{0.85}Ti_{0.15}$ $b = 5.728 \pm 0.003$ Å, which is 0.141 Å smaller than for α-U [161]. The reduction of *b* can be followed by the shift of the relevant reflections α(021) and α(131), which move to higher angles with increase of the Ti concentration (see Fig. 7.1 (a, b)). There is not much pre-existing structure information available on the quenched U-Ti alloys, but the available report on water quenched alloy with 3.7 at.% of Ti gives $b = 5.833$ Å [163], which is close to the value observe on $U_{0.95}Ti_{0.05}$. According to the nomenclature introduced by Lehmann and Hills the modification of α-U with reduced *b* is referred to as α′-U [164]. In contrast to change of *b* modification of *a* and *c* is not that noticeable. *a* exhibits slight increase, for $U_{0.85}Ti_{0.15}$ it equals to 0.017 Å (with respect to α-U [161]), while *c* remains almost unchanged taking into account the possible error of the refinement and experiment.

Table 4 Lattice parameters of the U-Ti splats with Ti concentration ≤50 at.%.

For $U_{1-x}Ti_x$ x*100 corresponds to Ti concentration in at.%	*a* (α-U), Å	*b* (α-U), Å	*c* (α-U), Å	*a* (γ-U), Å	Grain size of the main phase, Å	
					α-U	γ-U
Literature α-U [161]	2.854	5.869	4.955	--	--	--
U splat	2.846 ±0.002	5.828 ±0.002	4.931 ±0.002	--	--	--
Water quenched	2.868	5.833	4.970	--	--	--

For $U_{1-x}Ti_x$ x*100 corresponds to Ti concentration in at.%	*a* (α-U), Å	*b* (α-U), Å	*c* (α-U), Å	*a* (γ-U), Å	Grain size of the main phase, Å	
					α-U	γ-U
$U_{0.963}Ti_{0.037}$ [163]						
$U_{0.95}Ti_{0.05}$	2.859 ±0.001	5.837 ±0.002	4.963 ±0.001	--	500±5	--
$U_{0.90}Ti_{0.10}$	2.862 ±0.005	5.763 ±0.012	4.955 ±0.007	3.532 ±0.003	487±5	--
$U_{0.85}Ti_{0.15}$	2.871 ±0.002	5.728 ±0.003	4.957 ±0.002	3.532 ±0.003	285±5	--
$U_{0.80}Ti_{0.20}$	--	--	--	3.440 ±0.003	--	574 ±5
$U_{0.75}Ti_{0.25}$	--	--	--	3.431 ±0.003	--	576 ±5
$U_{0.70}Ti_{0.30}$	--	--	--	3.437 ±0.01	--	512 ±5
$U_{0.50}Ti_{0.50}$	--	--	--	3.377 ±0.003	--	844 ±5

Thorough study of the unalloyed U splat indicates that small well-dispersed grains of γ-U phase can be present between the α-U grains [165]. The presence of the grains is not recognizable from the X-ray diffraction pattern of the splats. The main reason is the low concentration of the phase, on the other hand, analysis is complicated due to the strong texture.

X-ray diffraction was performed on the surface of the as-formed splat, because any attempt to crush the sample leads to a significant broadening of the peaks. Comparison of the U splat with Ti alloyed specimens reveals the following distinct features: 1) concentrations of UC and UO_2 spurious phases, appearing for U metal, are significantly reduced even in $U_{0.95}Ti_{0.05}$ (see Fig. 7.2). The UC admixture originates from the starting U metal, in which 0.2 wt. percent of impurities represent mainly C and Al (UC is a weak Pauli paramagnet) ; 2) the main impurity phase present in U_{1-}

$_{x}$Ti$_{x}$ alloys is TiC which appears around 41.8 deg (see Fig. 7.1 (b), Fig. 7.2); 3) intensity of the main peaks of the patterns could be enhanced by γ-U phase.

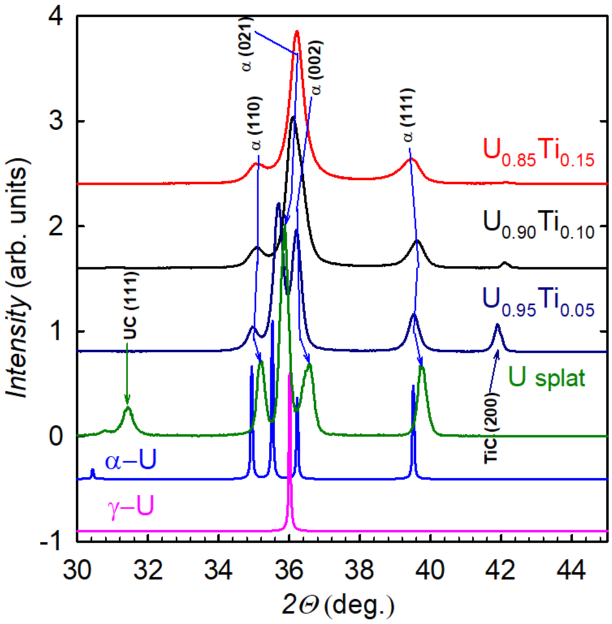

Fig. 7.2 Comparison of the diffraction patterns measured on the surface of unalloyed U and U$_{1\text{-}x}$Ti$_{x}$ splats. The progress of the main reflection of α-U phase is depicted by the arrows. Color scheme taken similar to Fig. 7.1.

The texture issue is the main reason why reliable lattice parameters of γ-U are reported only for splats with Ti concentration > 15 at.% (see Table 4). Diffraction pattern of $U_{0.80}Ti_{0.20}$ splat contains a broad assymetric peak of α-U located between 35.6 and 36.6 deg. The intensity of the peak is 10 times lower than the intensity of the main peak which corresponds to γ-U phase (see Fig. 7.1 (a)). Lattice parameter of the phase a=3.440±0.001 Å, it is 0.092 Å smaller than the lattice parameter reported in [160]. The reason of the reduction of the lattice parameter is related with the difference of the sized of U (0.156 Å, [166]) and Ti (0.147 Å, [167]). In the retained *bcc* solid solution, smaller Ti occupies 1/5 of the U sites leading to the shrinkage. Further increase of the Ti concentration extends this tendency. Study of the $U_{0.75}Ti_{0.25}$ and $U_{0.70}Ti_{0.30}$ splats does not show any sign of α-U. TiC is the only impurity phase which was confirmed by the EDX study (Fig. 7.4 (c, d)). Rietveld refinement of the pattern obtained on $U_{0.70}Ti_{0.30}$ splat is shown on Fig. 7.3, it confirmed the texture with preferred orientation in the (110) direction perpendicular to the sample surface. The EBSD map proved the formation of distinctive grains of γ-U (see Fig. 7.4 (a)). SEM study of the sample also show that UC particles are present on the surface (see Fig. 7.4 (b)), but their concentration is low to be detected by X-ray diffraction.

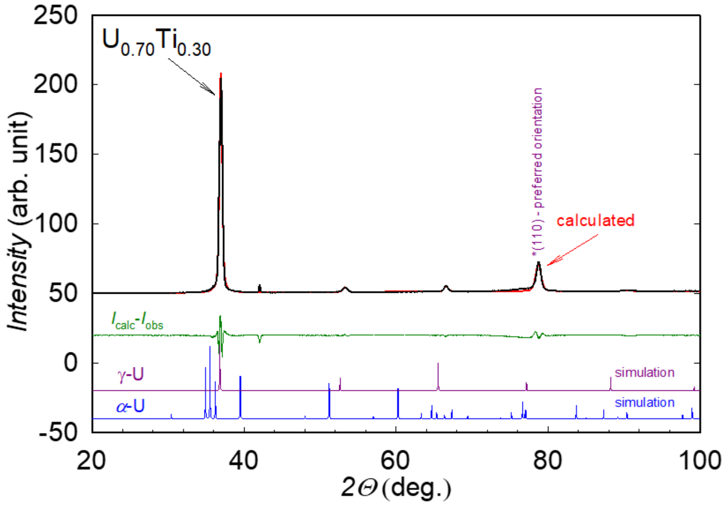

Fig. 7.3 Result of the Rietveld refinement of the diffraction pattern measured on $U_{0.70}Ti_{0.30}$. Red and black plots respectively correspond to calculated and experimental patterns. I_{calc}-I_{obs} – indicates the plot of the residual intensity (green).

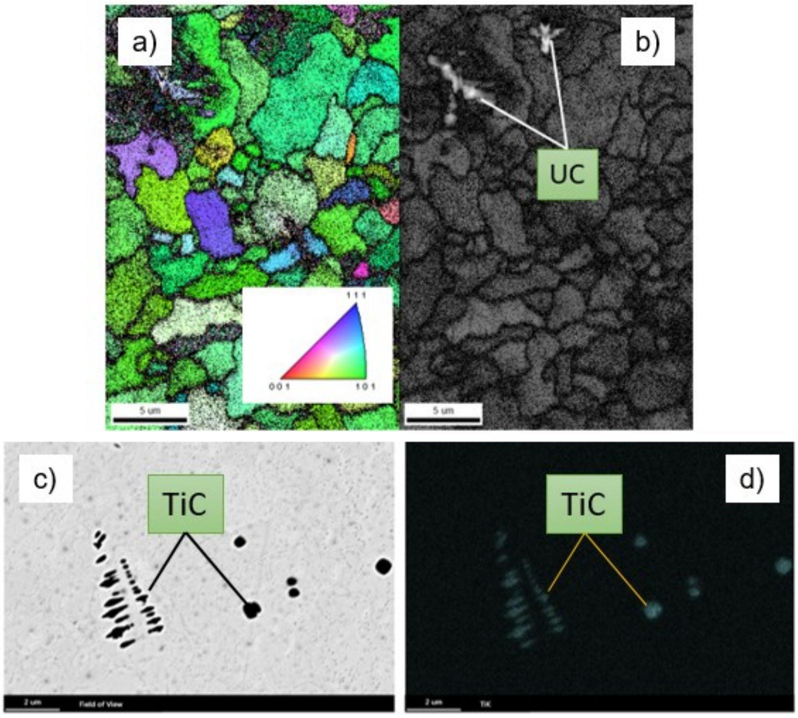

Fig. 7.4 (a) - EBSD orientation map of γ-U grains measured on the surface of $U_{0.70}Ti_{0.30}$ splat (inset indicates color scheme of the orientations); (b) UC particles on the surface of the same splat; (c) BSE image of $U_{0.85}Ti_{0.15}$ splat with identified TiC precipitates; (d) EDS map of Ti (blue, K electron edge) on the surface of $U_{0.85}Ti_{0.15}$ splat compared with the BSE image of the same region (c).

The lattice parameter of γ-U phase in the splats with 20, 25, 30 and 50 at.% Ti equals to 3.440 ± 0.003 Å, 3.431 ± 0.003 Å, 3.437 ± 0.01 Å, and 3.377 ± 0.003 Å, respectively (see Table 4). Considerable peak broadening observed on the alloy with 30 at.% of Ti gives a higher experimental error. It can be attributed to chemical inhomogeneity and defects induced by fast cooling. Early studies of the alloys with high concentration of Ti do not report dominance of the *bcc* phase even for 30 at.% of the element [116, 117], which shows the advantage of using the splat cooler. X-ray study of the furnace cooled (slow cooled) bulk $U_{0.70}Ti_{0.30}$ alloy also did not show apparent sign of the γ-U phase, structural refinement reveals U_2Ti accompanied by 20 % of α-U with $a = 2.869 \pm 0.002$ Å, $b = 5.854 \pm 0.002$ Å, $c = 4.972 \pm 0.002$ Å (see Fig. 7.5). Lattice parameters of α-U phase are higher than the ones observed for the $U_{0.95}Ti_{0.05}$ splat, in other words, furnace cooling leads to stabilization of the equilibrium phases.

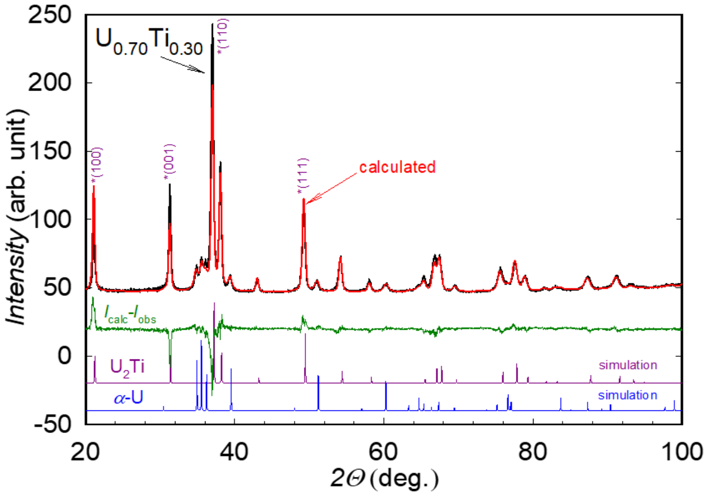

Fig. 7.5 Result of the Rietveld refinement of the diffraction pattern measured on furnace cooled $U_{0.70}Ti_{0.30}$ alloy.

Fast cooling of the U-Nb alloys produces different results, it can lead to the formation of more distorted phases of U. Below 15 at.% Nb alloying refinement of data indicates formation of the monoclinic α″-U phase (sp. gr. *C2/m* with the angle $\gamma \neq 90^{\circ}$). A higher concentration of Nb undoubtedly stabilizes the tetragonally distorted form of γ-U which is denoted as γ^0-U phase (sp. gr. *I4/mmm*). Let us look at development of the structures. The diffraction pattern of the $U_{0.95}Nb_{0.05}$ splat loses, when compared with pure U splat, the intensity of the peaks located between 41° and 75°, which can be related to a more pronounced texture of the alloyed splat (see Fig.

7.6 (a)). Structure refinement shows a reduction of *b* by 0.059 Å from the equilibrium lattice parameter [161], *a* and *c* remain practically unchanged (see Table 5). While 5 at.% alloying leads to stabilization of the α′ phase, increase of Nb concentration to 10 and 13 at.% leads to the α″ phase. Lattice parameters obtained from the refinement of $U_{0.90}Nb_{0.10}$ and $U_{0.87}Nb_{0.13}$ exhibit minor deviations from the ones which were observed on the $U_{0.95}Nb_{0.05}$ (see Table 5), monoclinic structure gives an additional degree of freedom which improves the quality of their refinement. The study of the water and air-cooled material performed by Tangri [126] presented similar results: 1) the water quenched alloy with 10 at.% of Nb exhibits the α″ phase (air-cooled shows the α′ phase); 2) air and water-cooled alloys with 13 at.% of Nb exhibit the α″ phase.

Table 5 Lattice parameters of the U-Nb splats with Nb concentrations ≤20 at.%.

For $U_{1-x}Nb_x$ x*100 corresponds to Nb concentration in at.%	*a* (α-U), Å	*b* (α-U), Å	*c* (α-U), Å	*a* ($\gamma \mid \gamma^0$ - U), Å	*c* (γ^0 - U), Å	Grain size of the main phase, Å	
						α-U	$\gamma(\gamma^0)$-U
Literature α-U [161]	2.854	5.869	4.955	--		--	--
U splat	2.846 ±0.002	5.828 ±0.002	4.931 ±0.002	--	--	--	--
$U_{0.95}Nb_{0.05}$	2.863 ±0.002	5.810 ±0.001	4.966 ±0.002	--	--	539 ±5	--
$U_{0.90}Nb_{0.10}$ (with α″-U)	2.866 ±0.006	5.793 ±0.007	4.987 ±0.020	--	--	284 ±5	--
$U_{0.87}Nb_{0.13}$ (with α″-U)	2.883 ±0.002	5.825 ±0.003	4.978 ±0.002	--	--	206 ±5	--
$U_{0.85}Nb_{0.15}$	--	--	--	3.504 ±0.003	3.377 ±0.007	--	271 ±5
$U_{0.83}Nb_{0.17}$	--	--	--	3.483 ±0.003	3.389 ±0.004	--	593 ±5

For $U_{1-x}Nb_x$ x*100 corresponds to Nb concentration in at.%	*a* (α-U), Å	*b* (α-U), Å	*c* (α-U), Å	*a* (γ | γ^0 - U), Å	*c* (γ^0 - U), Å	Grain size of the main phase, Å	
						α-U	γ(γ^0)-U
$U_{0.80}Nb_{0.20}$	--	--	--	3.456 ±0.005	--	--	452 ±5

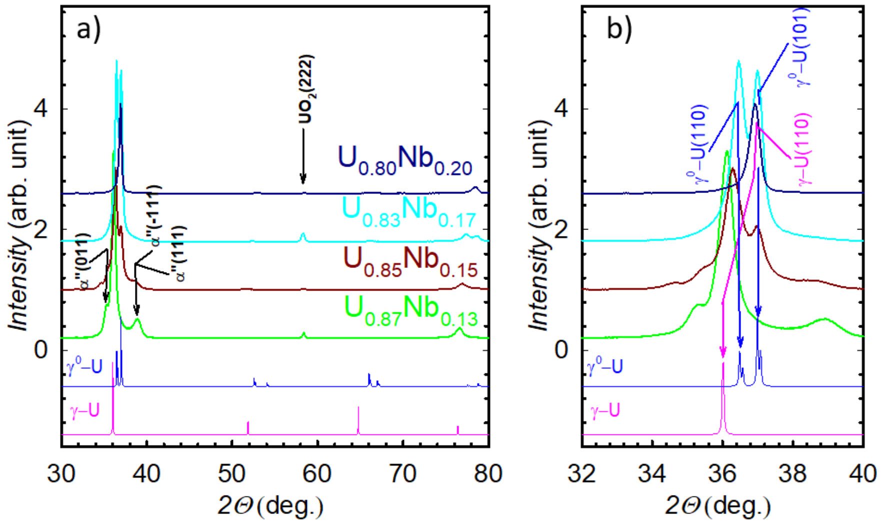

Fig. 7.6 (a) – comparison of the diffraction patterns of the fast cooled U-Nb alloys and pure U (Nb concentration equals 5,10 and 13 at.%). (b) – details of the main reflections of α-U and α˝-U located in the range 30 - 41 deg. Pink and blue lines at the bottom indicate calculated γ-U [160] and α-U [161] XRD patterns.

The lattice parameters of the α˝ phase reported by Tangri [126] are slightly different from the refined ones (see Table 5), for 13 at.% alloying *a* and *b* are respectively smaller by 0.033 and 0.054 Å, and *c* is larger by 0.017 Å. From the development of the most intense peaks located between 32° and 41° it is also possible to see that $U_{0.90}Nb_{0.10}$ has a different appearance than $U_{0.95}Nb_{0.05}$ (see Fig. 7.6 (b)). For $U_{0.95}Nb_{0.05}$ the peak which is present around 39.5° corresponds to α(111), on the pattern of $U_{0.90}Nb_{0.10}$ the peak is broadened and shifted to higher angles by 0.2°. As such the peak is better fitted by the doublet of the monoclinic structure α˝(-111) and α˝(111). In addition, the peaks α(021) and α(002), which are distinguished on the pattern of $U_{0.95}Nb_{0.05}$ transform into non-symmetrical "singlet" of α˝(102) and α˝(200) for $U_{0.90}Nb_{0.10}$. Similar changes are observed on the pattern of the $U_{0.87}Nb_{0.13}$ splat (see

Fig. 7.6 (b)). On the other hand, refinement gives values of the gamma angle of the monoclinic structure close to the reported by Tangri water quenched alloys: 1) for $U_{0.90}Nb_{0.10}$ it equals 90.82º±0.05º (90.88 for quenched alloy with 11.2 at.% Nb [126]); 2) for $U_{0.87}Nb_{0.13}$ gamma equals 91.72º±0.05º (91.2º [126]).

Increase of the Nb concentration up to 15 at.% results in the stabilization of the tetragonal γ^0-U. For $U_{0.85}Nb_{0.15}$ there are two peaks between 35.8º and 37.4º which correspond to the $\gamma^0(110)$ and $\gamma^0(101)$ reflections (see Fig. 7.7 (a, b)). Comparison of the intensities of the α″(011) and α″(111) peaks indicates a significant reduction of the amount of the monoclinic phase when Nb concentration raised from 13 to 15 at.% (see Fig. 7.7 (a)). EBSD study of the $U_{0.85}Nb_{0.15}$ splat confirms the diffraction results (see Fig. 7.8 (a, b)), 93% of the identified area designate γ^0-U (green area on Fig. 7.8 (b)). This outcome is comparable with the other works, Tangri observed the γ^0 phase in the air-cooled samples with 15 at.% Nb, water quenching leads to stabilization of the γ^0 phase as a major phase with 16.8 at.% Nb [126]. Anagnostidis observes γ^0 only for quenched alloys beyond 15.7 at.% Nb [168].

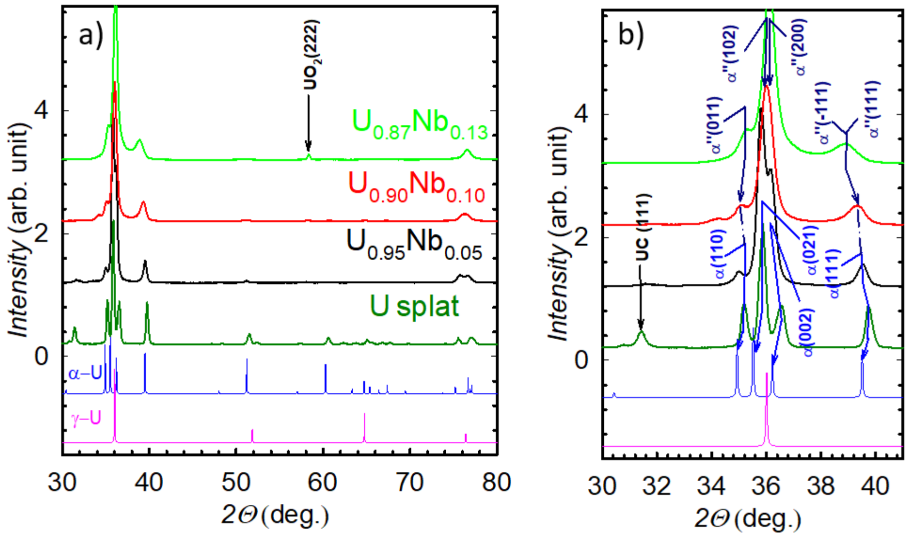

Fig. 7.7 (a) – diffraction patterns of splats with following Nb concentrations: 13, 15, 17 and 20 at.%. (b) – details of the measured diffraction data between 32º and 40º. Blue and pink lines at the bottom correspond to calculated γ [160] and γ^0-U XRD patterns. Values of *a* and *c* were taken from the refinement of $U_{0.83}Nb_{0.17}$.

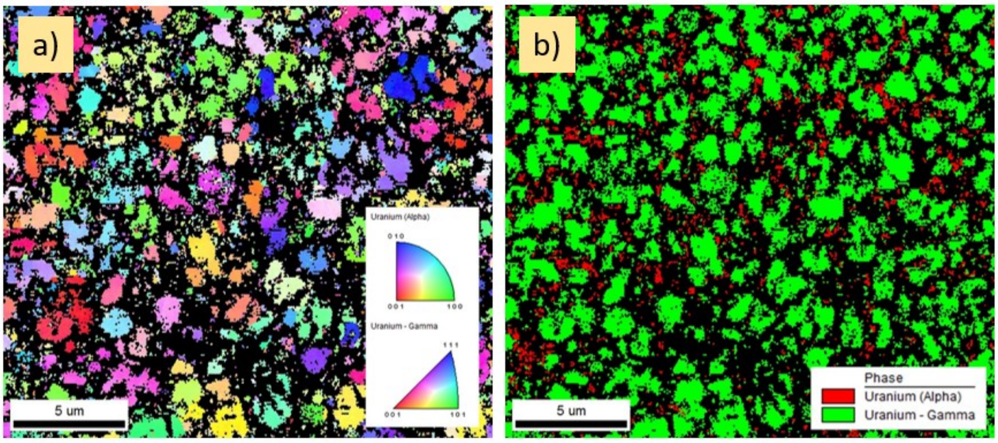

Fig. 7.8 EBSD maps of crystallographic orientation (a) and phase distribution (b) of the $U_{0.85}Nb_{0.15}$ splat. The inverse pole figure plots (inset of (a)) represent relative crystallographic orientation of α″-U and γ^0-U. The green, red and black colors of (b) respectively correspond to γ^0-U, α″-U and undefined area due to pure electron diffraction.

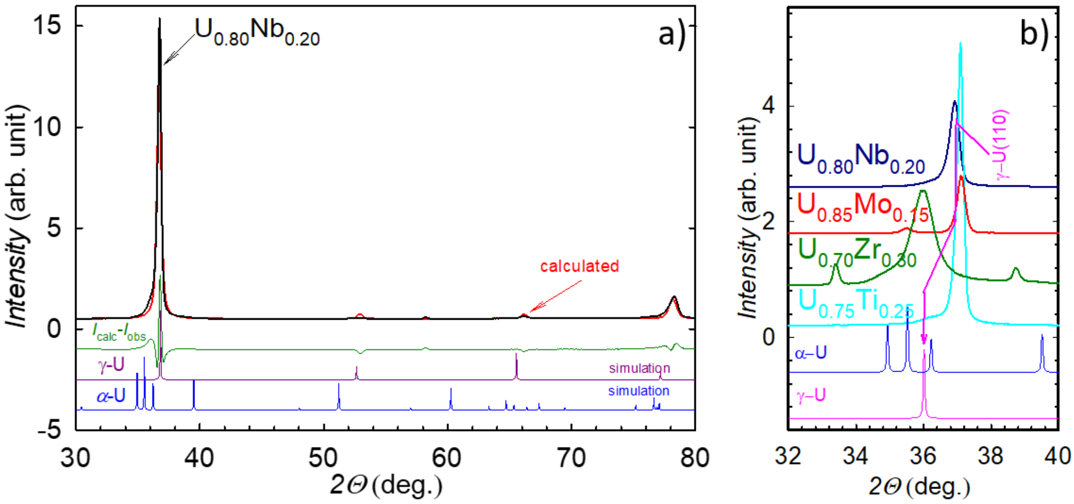

Fig. 7.9 (a) – Rietveld refinement of the diffraction pattern measured on $U_{0.80}Nb_{0.20}$. Red and black plots respectively correspond to calculated and experimental patterns. I_{calc}-I_{obs} – indicates the plot of the residual intensity (green). (b) – comparison of the diffraction patterns of $U_{0.70}Zr_{0.30}$, $U_{0.75}Ti_{0.25}$, $U_{0.80}Nb_{0.20}$ and $U_{0.85}Mo_{0.15}$ splats which exhibit γ-U phase (ZrC is present for $U_{0.70}Zr_{0.30}$).

X-ray diffraction pattern of $U_{0.83}Nb_{0.17}$ splat does not show any signs of α type of structure, on the Fig. 7.7 (b) it is visible that α″(011) and α″(111) peaks which are still present for $U_{0.85}Nb_{0.15}$ vanish for the 17 at.% alloyed splat. UO_2 is the only identified impurity phase (Fig. 7.7 (a)). The determined lattice parameters are present in Table 5, they are equal to the reported ones taking into account experimental error

[126]. Further increase of Nb concentration up to 20 at.% allows to stabilize the γ-U phase. Rietveld refinement shown in Fig. 7.9 (a) yields the lattice parameter $a =$ 3.456 ± 0.005 Å. Another property of the Nb alloyed splats is the texturing, similar as in the U-Ti alloys. In comparison with the Mo alloyed splats which were studied earlier [165], the Ti and Nb ones are less efficient stabilizers of the γ-U phase, the opposite is true in relation to the Zr alloying. Patterns of the splats with the minimum required concentration of T (T = Mo, Zr, Ti, Nb) are shown on Fig. 7.9 (b), 25 at.% Ti alloying leads to the smallest lattice parameter of 3.456 Å.

7.1.1.2.Transport properties of U-Ti and U-Nb alloys.

A direct insight into the electronic properties of the Nb and Ti alloyed splats was obtained via investigation of electrical resistivity $\rho(T)$. The results of the measurements performed on the U-Ti splats are presented in Fig. 7.10. With respect to the pure U splat, a considerable difference between the absolute value and slope of $\rho(T)$ appears for $U_{0.90}Ti_{0.10}$ already. Pure U splat exhibits a positive resistivity slope $\frac{\mathrm{d}\rho}{\mathrm{d}T}$ typical for metals. It is also similar to the resistivity of bulk U with the α-U phase. Starting from 12.4 μΩcm at T = 3.3 K, $\rho(T)$ of the pure U splat smoothly increases with increasing T. Below 50K it can be described by $\rho = \rho_0 + aT^2$ with $a = 16.3*10^{-4}$ μΩcm/K^2. From the perspective of the Kadowaki-Woods relation $R_{\mathrm{KW}}=\frac{a}{\gamma^2}$ (where γ is the Sommerfeld coefficient), the value $R_{\mathrm{KW}} = 1.3*10^{-5}$ μΩcm (mol K/mJ)^2 naturally places the U splat among correlated systems.

The splat $U_{0.90}Ti_{0.10}$ has more than ten times higher residual resistivity of 151.9 μΩcm and roughly ten times smaller slope (estimated between 50 K and 150 K). The shape of $\rho(T)$ still resembles a regular metal and the change of the slope supports the information on the crystal structure. The resistivity shape of the splat could be described by two phases, one with a positive slope that originates from the α-U phase, while the Ti alloyed γ-U phase contributes by the tendency to a negative slope. For the splat with 15 at.% of Ti ($U_{0.85}Ti_{0.15}$), the increase of the concentration of γ-U phase rises the contribution of the negative slope component and $\rho/\rho_{300\mathrm{K}} \approx 1$.

$U_{0.85}Ti_{0.15}$ exhibits residual resistivity by 14.7 μΩcm higher than $U_{0.90}Ti_{0.10}$. The most significant change of the resistivity slope, turning into weakly negative, is observed for $U_{0.80}Ti_{0.20}$ (Fig. 7.10, left plot). Here $\rho(T)$ slowly decreases from 129.2

μΩcm (at $T = 2$ K) to 118.7 μΩcm (at $T = 300$ K). The lower value of the residual resistivity could be perhaps related to almost single-phase nature. It exhibits only a trace of the most intense α(021) peak. However, the accuracy of absolute values is limited by 10-20% error in the determination of the geometrical factor, given mainly by the somewhat variable thickness. The splats with Ti concentrations exceeding 20 at.% yield a higher residual resistivity, but $\rho(T)$ is almost flat. $U_{0.70}Ti_{0.30}$ and $U_{0.50}Ti_{0.50}$ exhibit residual resistivity of 136.4 μΩcm and 169 μΩcm, respectively, which similarly decreases at 300 K by only 3-4 %. Comparison of the temperature dependences of resistivity $\rho(T)$ suggests that: 1) there is an interrelation between the phase composition and type of $\rho(T)$ for the studied U-Ti splats, as is clearly seen from the change of the residual resistivity of the mixed α+γ phase $U_{0.90}Ti_{0.10}$ and $U_{0.85}Ti_{0.15}$ splats with respect to the almost purely γ phase $U_{0.80}Ti_{0.20}$ splat (similar tendency was reported for the U-Mo splats [62]); 2) in the γ phase splats the increase of Ti concentration leads to higher residual resistivity ρ_0. The strong disorder can be considered as the reason of the negative temperature coefficient ($\frac{\mathrm{d}\rho}{\mathrm{d}T} < 0$) observed for $U_{1-x}Ti_x$ splats over very wide concentration range. Similar changes of the temperature coefficient of resistivity were observed for $V_{1-x}Ti_x$, $Nb_{1-x}Ti_x$, $Nb_{1-x}Ti_x$ [169]. It is evident that the U-Ti alloys belong to a quite broad class of strong-scattering alloys with very short mean free path.

We can summarize that the U-Ti as well as other *bcc* U-based alloys, which allow for a high concentration of alloying elements without segregation of another phase (as the splat cooled alloys) have resistivity features dominated by the strong atomic disorder. In this respect, we do not deal with particularly actinide-specific feature, although the presence of enhanced density of states at the Fermi level can make impurity scattering effects very efficient (e.g. by providing high density of final states). However we deal with effect inherent, besides numerous solid solutions [63], also to metallic glasses [57]. Focusing on details, we see that we actually deal with two phenomena. One is the rapid enhancement of residual resistivity, which is faster than enhancement of the value at 300 K. Apparent violation of the Matthiessen's rule, i.e. loss of additivity of electron scattering on "impurities" with electron-phonon scattering can be seen as a consequence of approaching the Mott limit – the electron mean free path cannot be shorter than inter-atomic distances.

The other and more subtle (but equally general [63]) effect is the negative resistivity slope developing for high degree of disorder. Although originally seen as due to special position of the Fermi level, at present quantum interference effects are taken responsible for the negative slope [66]. Phenomena which go beyond the framework of relaxation time approach, increase resistivity by the enhanced probability of electrons to be scattered back. This effect is gradually suppressed by electron-phonon scattering, being in principle inelastic, hence destroying the quantum coherence. Low-temperature studies of resistivity indicate that all of the studied U-Ti splats are superconductors. The critical temperatures of the transition are presented in Table 6. Maximum transition temperature $T_c = 1.98$ K was observed for the $U_{0.80}Ti_{0.20}$ splat. $U_{0.85}Ti_{0.15}$ exhibits notably lower critical temperature of 0.76 K. Normalized resistivities with respect to the value in the normal state shows that microstructural features of the splats affect the appearance of the transition (see Fig. 7.11 (a)). This splat exhibits a broad transition, the width of which can be characterized by difference between the temperature where it starts and finishes: $\Delta T = T(\rho_{\mathrm{start}})- T(\rho_{\mathrm{end}}) = 0.3$ K. The broad transition can reflect inhomogeneous distribution of Ti atoms as well as mixing of two phases. The second proposition is supported by the study of U-Mo splats with different rations of α to γ phase content and respectively different T_c values.

The transition temperature of $U_{0.75}Ti_{0.25}$ is reduced comparing to $U_{0.80}Ti_{0.20}$ by 0.86 K, but starting from $U_{0.70}Ti_{0.30}$ it increases again. For $U_{0.70}Ti_{0.30}$ and $U_{0.50}Ti_{0.50}$ the temperatures are respectively equal to $T_c = 1.33$ K and $T_c = 1.78$ K (see Table 6 and Fig. 7.17 (b)). Application of magnetic fields reduces, as usual, the transition temperatures (Fig. 7.11 (a, b, c, d)), and the superconductivity is entirely suppressed exceeding the critical field. Detailed analyses of the field dependence $T_c\,(H)$ will be given later. Electrical resistivity of the U-Nb splats shows similar trends. Studied alloys with γ^0 ($U_{0.85}Nb_{0.15}$) and γ ($U_{0.80}Nb_{0.20}$) phases exhibit lower absolute values of $\rho(T)$ (left graph on Fig. 7.12), but both temperature dependencies have negative temperature coefficient $\frac{\mathrm{d}\rho}{\mathrm{d}T} < 0$ (right graph on Fig. 7.12). The increase of the Nb concentration brings more disorder and increase of residual resistivity, for $U_{0.85}Nb_{0.15}$ and $U_{0.80}Nb_{0.20}$ it, respectively, equals to 89 μΩcm and 109 μΩcm (see Table 6). An interesting feature of the 20 at.% Nb and Ti splat is the similarity of the slopes.

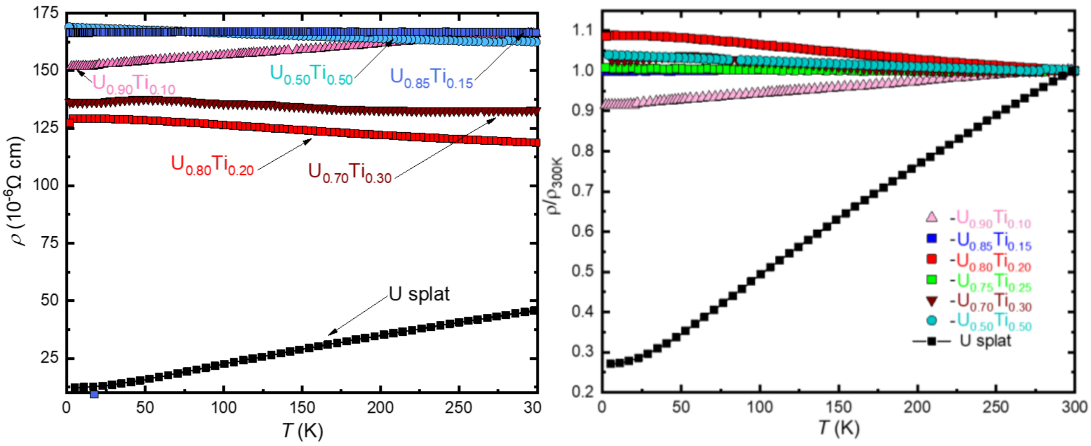

Fig. 7.10 Electrical resistivity ρ(T) of the U-Ti splats with different Ti concentration (from 10 to 50 at.%). The left graph depicts absolute values of ρ(T) while the right one the values normalized with respect to the room temperature resistivity ($\rho/\rho_{300\mathrm{K}}$).

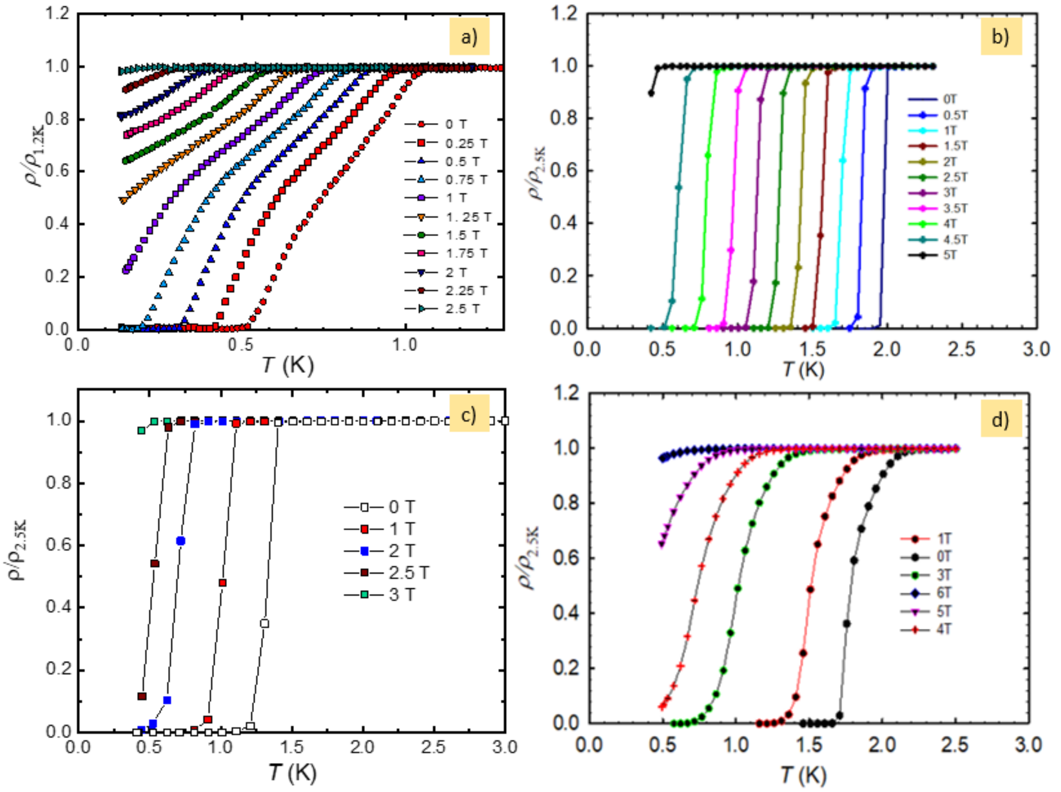

Fig. 7.11 Magnetic field dependence of electric resistivity of the selected U-Ti splats measured in the vicinity of the temperature of superconducting transition: a) $U_{0.85}Ti_{0.15}$; b) $U_{0.80}Ti_{0.20}$; c) $U_{0.70}Ti_{0.30}$; d) $U_{0.50}Ti_{0.50}$. Magnetic fields are indicated in the legends of the corresponding graphs.

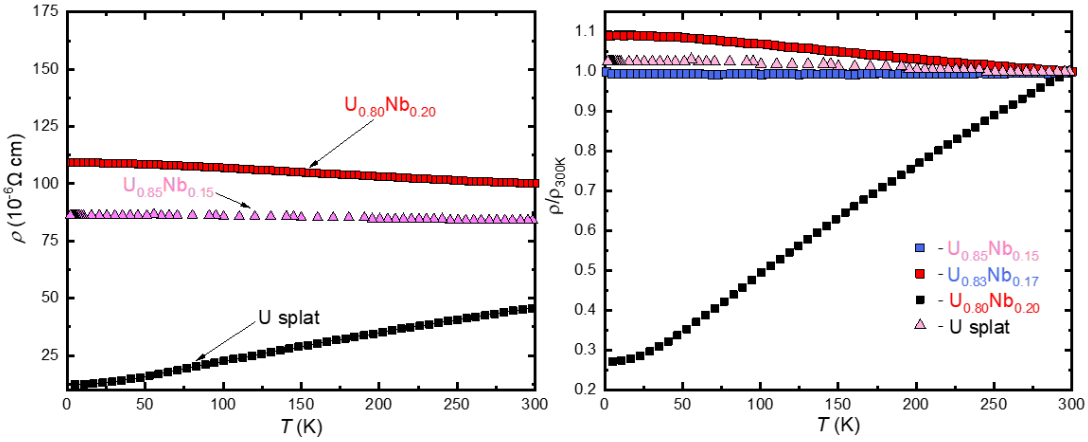

Fig. 7.12 Electrical resistivity $\rho(T)$ of the $U_{0.85}Nb_{0.15}$, $U_{0.83}Nb_{0.17}$ and $U_{0.80}Nb_{0.20}$. The left graph depicts absolute values of $\rho(T)$, right graph compares values of resistivity normalized with respect to the room temperature value (ρ/ρ_{300K}).

Table 6 Electrical resistivity parameters of U-Ti and U-Nb splats compared with the $U_{0.85}Mo_{0.15}$, $U_{0.70}Zr_{0.30}$, and U splat. $U_{0.85}Mo_{0.15}$ and $U_{0.70}Zr_{0.30}$ represent the splats with retained γ-phase. $\mu_0H_{c2}^*$ determined using the Werthamer-Helfand-Hohenberg theory.

Composition	ρ_{300K} (μΩcm)	ρ_0 (μΩcm)	T_c (K)	ΔT (K)	μ_0H_{c2} (T)	$\mu_0H_{c2}^*$ (T)	$-\mu_0dH_{c2}/dT$ (T/K)
$U_{0.85}Ti_{0.15}$	167.7	166.6	0.76	0.30	1.5	1.12	2.1
$U_{0.80}Ti_{0.20}$	129.2	118.7	1.98	0.05	6.03	4.71	3.4
$U_{0.75}Ti_{0.25}$	--	--	1.12	0.2	3.87	2.56	3.27
$U_{0.70}Ti_{0.30}$	132.7	136.4	1.33	0.2	3.96	2.92	3.42
$U_{0.50}Ti_{0.50}$	162.5	169	1.78	0.5	7.16	6.88	3.95
$U_{0.85}Nb_{0.15}$	83	86	1.91	0.15	6.71	4.6	3.42
$U_{0.83}Nb_{0.17}$	--	--	1.85	0.25	--	--	--
$U_{0.80}Nb_{0.20}$	99.9	109.1	1.96	0.22	5.95	4.48	3.27
$U_{0.85}Mo_{0.15}$[62]	89	95	2.11	0.02	6.7	5.3	3.6
$U_{0.70}Zr_{0.30}$[66]	73		0.80		0.35	0.30	2.8
U splat[62]	53	12.4	1.24		0.30	0.30	0.32

U-Nb splats also exhibit superconducting transition. $U_{0.85}Nb_{0.15}$ becomes superconducting below 1.91 K with $\Delta T = 0.15$ K (see Table 6). In comparison with $U_{0.85}Ti_{0.15}$ the critical temperature is thus substantially higher. The reason can be the phase composition, $U_{0.85}Nb_{0.15}$ contains mainly the γ^0 phase, which seems to be generally a stronger superconductor. This assumption is also supported by the study of U-Mo splats with the γ^0 phase [62]. For $U_{0.83}Nb_{0.17}$ the transition temperature equals to 1.85 K, but $\Delta T = 0.25$ K can mean a higher inhomogeneity. The γ phase splat $U_{0.80}Nb_{0.20}$ superconducts below the highest temperature among the studied alloys ($T_c = 1.96$ K). The influence of magnetic field on the resistivity of U-Nb splats is shown in Fig. 7.13. Nevertheless, one should bear in mind that ΔT is not a good probe into inhomogeneity, when ΔT is flat as a function of concentration, transitions can be sharp even for inhomogeneous cases.

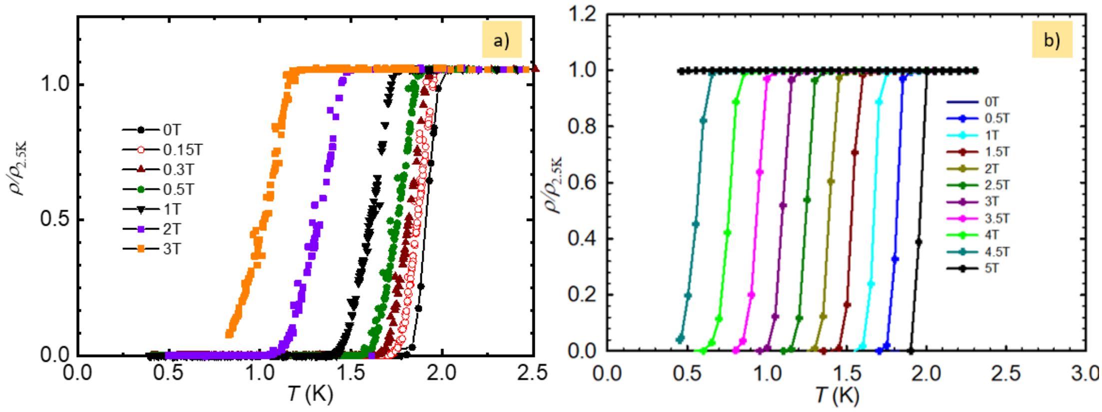

Fig. 7.13 Electrical resistivity $\rho(T)$ of $U_{0.85}Nb_{0.15}$ (a) and $U_{0.80}Nb_{0.20}$ (b) measured in various magnetic fields indicated in the legends.

Study of heat capacity of the U-Ti and U-Nb splats gives an outlook of the electronic structures for corresponding materials. Below 10 K, C_p/T vs. T^2 representation of specific heat data was found to decrease linearly, giving in extrapolation to $T = 0$ K the Sommerfeld coefficient γ (line plots in Fig. 7.14 (a, b, c)). Determination of the Debye temperature θ_D was performed using $C_p/T = \gamma + \beta T^2$ from the data measured below 10 K (where $\theta_D = (12\pi^4 R/5\beta)^{1/3}$).

Sommerfeld coefficient γ of the U-Ti splats weakly but systematically increases with increase of the Ti concentration (see Table 7). For $U_{0.85}Ti_{0.15}$ $\gamma = 13.4$ mJ/mol U K^2 is close to the values determined for U splat and bulk [170] (around 11 mJ/mol K^2). In comparison to U-Mo splats the change of the contribution of electronic specific heat with an increase of Ti concentration is lower. 30 at.% of Ti is required to approach γ measured on $U_{0.85}Mo_{0.15}$ (respectively 15.6 and 18.8 mJ/mol U K^2 [62], Table 7), the change of γ can also be followed from Fig. 7.14 (a). Evaluated Debye temperatures Θ_D decrease with rise of Ti concentration, for $U_{0.85}Ti_{0.15}$ and $U_{0.70}Ti_{0.30}$ the temperature accordingly equal 157 K and 143 K (see Table 7).

U-Nb splats exhibit similar tendencies, γ increases with increasing of Nb concentration. There is a considerable change of the Sommerfeld coefficient from 15 to 17 at.% alloying (see Fig. 7.14 (b)). $U_{0.85}Nb_{0.15}$ has γ=13.5 mJ/mol U K^2, which is close to the value of $U_{0.85}Ti_{0.15}$. On the other hand, for $U_{0.83}Nb_{0.17}$ γ equals 16.8 mJ/ mol U K^2. The highest value of γ=17.8 mJ/ mol U K^2 was revealed for splat with 20 at.% of Nb. Therefore, the Debye temperatures Θ_D of the Nb alloyed splats decrease from 151 K to 131 K (respectively for $U_{0.85}Nb_{0.15}$ and $U_{0.80}Nb_{0.20}$, Table 7).

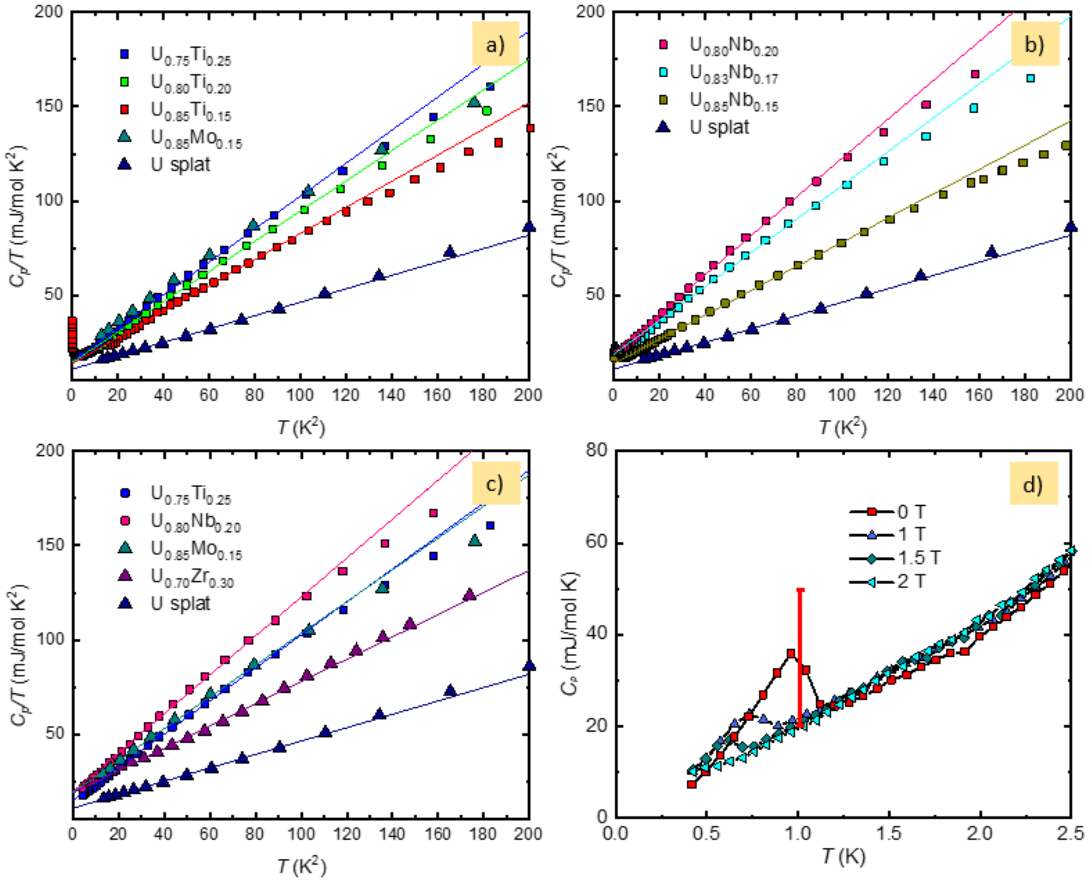

Fig. 7.14 Low-temperature specific heat of the U-Ti and U-Nb splats. (a), (b), (c) - C_p/T vs. T^2 representation of the heat capacity data with a linear fit for determination of the Sommerfeld coefficient; (d) – specific heat of $U_{0.70}Ti_{0.30}$ measured in different magnetic fields. Red bar indicates ΔC=29.7 mJ/mol U K estimated according to BCS theory. The presented data are normalized per mole U.

For the studied U-Ti and U-Nb splats increase of the Sommerfeld coefficient is a clear indication of the rise of the density of states at the Fermi level related to narrowing of 5*f*-band due to the change of the interatomic U-U spacing. Among the pure γ-U splats the most significant change of low-temperature specific heat underwent $U_{0.80}Nb_{0.20}$, it is followed by $U_{0.75}Ti_{0.25}$ (see Fig. 7.14 (c)), nevertheless the value does not reach γ measured on $U_{0.85}Mo_{0.15}$ (18.8 mJ/ mol U K^2 [62]). Lowering of the Debye temperature indicates the softening of the lattice. Moreover, the Debye temperatures of the U-Ti and U-Nb splats with γ-U structure are considerably lower from the α-U with $\theta_D = 179$ K [66]. Similar lattice softening was observed for α-Pu (153 K) and δ-Pu (103 K) [62].

The variations of the γ-values can be attributed to a modest volume expansion between the α- and γ-type of phases, yielding a narrowing of the 5*f* band. On the other hand, as the concentration of uranium, bringing the 5*f* states, decreases with further alloying (at least if normalized per formula unit), the increase of γ cannot extend to low U concentrations, unless the 5*f* states localize due to the enhanced U-U spacing. Indeed experimentally we see that it is not the case, which is undoubtedly due to the 5*f* hybridization with the *d*-states of the early *d*-metals, which are overlapping the 5*f* band in the energy scale.

Calorimetric study of the superconducting phase transition was conducted for $U_{0.70}Ti_{0.30}$ (see Fig. 7.14 (d)). It exhibits a characteristic λ-type anomaly of the second-order phase transition. According to the weak coupling approximation to the Bardeen–Cooper–Schrieffer (further BCS) theory the difference between the specific heat in superconducting state and "normal" state can be described by $\Delta C = C_s - C_n = 1.43\ \gamma\ T_c$. The difference between the estimated value ΔC_{th} (red bar in Fig. 7.14 (d)) and experimental ΔC_{exp} can be understood as the result of experimental setting (insufficient number of temperature points). However, as ΔC_{exp} is close to ΔC_{th} we can be confident that superconductivity is a bulk, not spurious, property. Magnetic field suppresses the anomaly and shifts the transition temperature to lower values, while it vanishes above the field of 2 T. The resistivity measurements display superconducting transition still at 2.5 T (see Fig. 7.11 (c)).

Table 7 Summary of the Sommerfeld coefficient γ, Debye temperatures Θ_D and β of the splats determined from the fits of the low-temperature specific heat.

Composition	γ (mJ/ mol U K^2)	Θ_D (K)	β (mJ/mol K^4)
$U_{0.85}Ti_{0.15}$	13.4	157	0.58763
$U_{0.80}Ti_{0.20}$	13.7	144	0.65027
$U_{0.75}Ti_{0.25}$	14.1	142.8	0.66785
$U_{0.70}Ti_{0.30}$	15.6	142.6	0.66986
$U_{0.85}Nb_{0.15}$	13.5	151	0.55208
$U_{0.83}Nb_{0.17}$	16.8	136	0.76665
$U_{0.80}Nb_{0.20}$	17.8	131	0.84808
U splat	11	179	0.33889
$U_{0.70}Zr_{0.30}$	16.9	165	0.43268
$U_{0.85}Mo_{0.15}$	18.8	139	0.72373

At this point, we have the necessary information for the examination of the field dependence of T_c of U-Ti and U-Nb splats. An important parameter is the slope of the upper critical field at T_c, expressed as $-\mu_0 dH_{c2}/dT$. The lowest resistance against the magnetic field was found for $U_{0.85}Ti_{0.15}$ (see Fig. 7.15). It displays $-\mu_0 dH_{c2}/dT = 2.1$ T/K, which is the smallest slope among all the studied U-Ti and U-Nb splats (see Table 6). For higher concentrations of Ti, the values gradually increase, reaching 3.95 T/K for $U_{0.50}Ti_{0.50}$. Comparing $U_{0.80}Nb_{0.20}$ and $U_{0.80}Ti_{0.20}$ we observe similar behavior, very close T_c values as well as upper critical fields $\mu_0 H_{c2}$ and its critical slope (see Table 6). The upper critical field of the weak electron-phonon coupling superconductors is obtained in the Werthamer–Helfand–Hohenberg (WHH) theory for weak coupling superconductors. For low temperature limit (T–>0) it is obtained as $H_{c2}(0) \approx 0.7*T_c*(-dH_{c2}/dT)$ [171]. For the studied splats, the WHH upper critical fields do not match well the real behaviour, as shown later. The usual reason is the insufficiency of the weak coupling BCS theory. The more general strong coupling theory of superconductivity, which gives e.g. a *k*-dependence of the superconducting gap, do not yield such simple universal relations, therefore it is still useful to use the weak coupling limit as a benchmark.

The deviations from WHH were found already for U-Mo alloys [62]. We can use the method proposed there, to extrapolate to $T = 0$ using a quadratic polynomial. The values of the upper critical fields estimated by WHH theory ($\mu_0 H_{c2}^*$) and quadratic polynomial ($\mu_0 H_{c2}$) are presented in Table 6. Exceeding the values for $U_{0.85}Mo_{0.15}$ with the γ-phase, the U-Ti and U-Nb splats exhibit the upper critical field in the range of 6 to 8 T (see Fig. 7.15). $U_{0.70}Ti_{0.30}$ with $\mu_0 H_{c2} = 3.96$ T represents a minimum in the U-Ti system. From the perspective of the response of superconductivity to magnetic field, the studied alloys are similar to A15 superconductors with strong coupling [172, 173], but the T_c value of those usually exceeds 10 K. However, the A15 superconductors do not have atomic disorder, which can reduce T_c significantly [62, 173].

Naturally, the question is how the superconductivity develops on the other side of phase diagram, where we deal with U diluted in the Ti matrix.

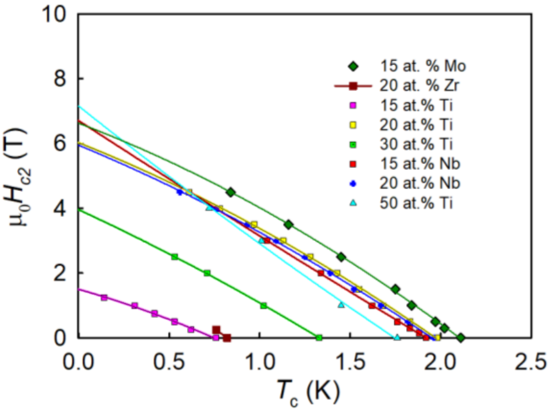

Fig. 7.15 Critical magnetic field H_{c2} vs. critical temperature T_c of U-Ti, U-Nb splats and γ-U alloys presented in [62, 66] ($U_{0.85}Mo_{0.15}$, $U_{0.80}Zr_{0.20}$). The line plots represent the quadratic polynomial fit of the data.

7.1.2. Structure, magnetic and transport properties of Ti rich alloy.

This section is based on article *"Anomalous Superconductivity of the U-Ti Alloys"* which is published in Journal of the Physical Society of Japan (Proc. Int. Conf. Strongly Correl. Electron Syst.) by V. Buturlim, O. Koloskova, P. Minarik, L. Havela (2020, doi:10.7566/JPSCP.30.011063.)

7.1.2.1. Crystal structure of $U_{0.20}Ti_{0.80}$.

Increasing the Ti concentration, the melting point of U-Ti alloys increases. Due to surface interdiffusion of the precursor into the Cu stage of the splat-cooler $U_{0.20}Ti_{0.80}$ was synthesized in bulk form (furnace cooled). The XRD pattern was obtained from the cut surface of the bulk specimen. It displays a strong crystallographic texture similar to the U-Ti splats. Fig. 7.16 presents the results of the Rietveld refinement analysis performed on the data set measured on the alloy with 80 at.% Ti (i.e. $U_{0.20}Ti_{0.80}$), there is clear domination of the grains with (110) and (200) directions. It reveals certain inhomogeneity reflected by the presence of two *bcc* phases with slightly different parameters and differing also in texture. It was confirmed by the EDX study. On the electron micrograph (inset of Fig. 7.16), bright regions correspond to $U_{0.20}Ti_{0.80}$, while the dark stripes exhibit $U_{0.17}Ti_{0.83}$. There is in addition a broadening of diffraction peaks, interpreted as lattice parameter gradient. We can assume it equal to $a = (3.33 \pm 0.01)$ Å.

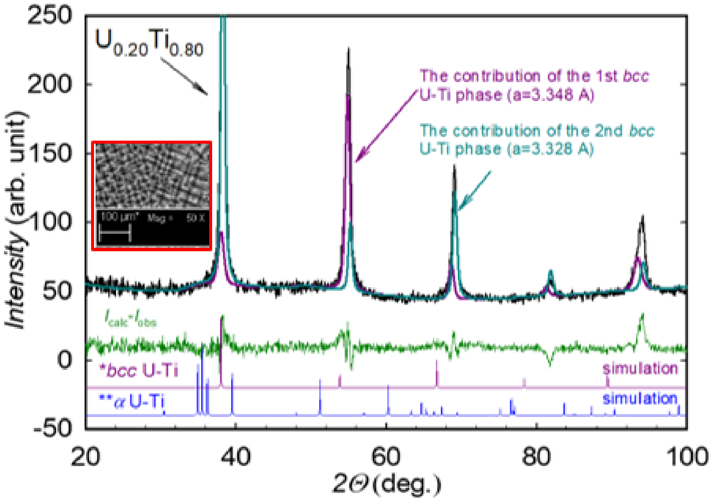

Fig. 7.16 The result of the Rietveld refinement of the diffractogram measured on the cut-surface of U with 80 at.% Ti. The inset presents the backscattered electron image of the 80 at.% Ti alloy.

7.1.2.2. Magnetic and transport properties of $U_{0.20}Ti_{0.80}$.

While the *bcc* U-rich alloys are as a rule weak Pauli paramagnets with susceptibility value close to that of α-U [174], the situation for U diluted in Ti had to be checked experimentally. The temperature dependence of the magnetic susceptibility shows that $U_{0.20}Ti_{0.80}$ is also a weak Pauli paramagnet with practically temperature-independent value, on the level of $3.25 \cdot 10^{-9}$ m^3/mol (Fig. 7.17 (a)). It is close to the values measured for the room-temperature *hcp* Ti and orthorhombic α-U phases ($1.9\cdot10^{-9}$ m^3/mol and $4.8\cdot10^{-9}$ m^3/mol, respectively) [175]. U-5*f* and Ti-3*d* states are lying at similar energies, they have good conditions for mutual hybridization, washing out U-moments. We, therefore, conclude that no U magnetic moments can be formed. At low temperatures, $U_{0.80}Ti_{0.20}$ exhibits a superconducting transition. Its critical temperature is considerably higher than for U-rich alloys, $T_c = 3.74$ K was determined from $\rho(T)$ (see Fig. 7.17 (b)).

The electrical resistivity of the Ti-rich alloys was actually studied long ago, nevertheless, authors question the phase purity of the material. The presence of U_2Ti phase was reported in the case of Ti concentration smaller than 65 at.% [176], it was shown earlier that due to fast cooling splats do not contain U_2Ti phase. The authors also highlight the fact that $U_{0.20}Ti_{0.80}$ alloy has the highest superconducting-transition temperature equal to $T_c = 3.80$ K confirmed by our study. Further, we will discuss properties of this "high T_c" superconductor.

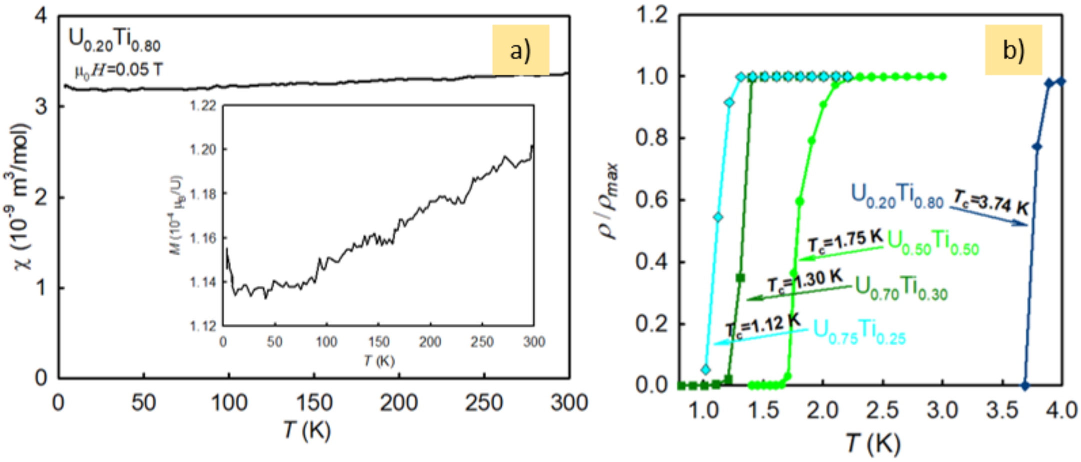

Fig. 7.17 (a) Magnetic susceptibility of the $U_{0.20}Ti_{0.80}$ alloy measured in magnetic field $\mu_0H = 0.05$ T. The inset presents temperature dependence of the magnetization of the $U_{0.20}Ti_{0.80}$ alloy (in $\mu_0H = 0.05$ T); (b) Normalized low-temperature electrical resistivity of the *bcc* U-alloys with various concentration of Ti.

Having observed such significant enhancement of T_c, one has to prove that the superconductivity is an intrinsic bulk property. With such aim, the specific heat of $U_{0.20}Ti_{0.80}$ alloy was measured down to $T = 2$ K. Results can be seen in the inset of Fig. 7.18 (a). At high temperatures, the $C_p(T)$ reaches the classical limit of 3R (where R is the gas constant - 8.31 J/mol K). In the *T*-range 200-300 K, the data follow the Debye model with the Debye temperature $\Theta_D \approx 290$ K. At low temperatures, the specific heat exhibits a pronounced λ-type anomaly. Application of an external magnetic field leads to the shift of the anomaly to lower temperatures (see Fig. 7.18 (a)). Specific heat measurements indicate a possible enhancement (if normalized per mole of U) of the Sommerfeld coefficient of electronic specific heat, $\gamma = 45$ mJ/mol U K^2 (9 mJ/mol K^2). This is a bit higher value with respect to *bcc* $V_{0.20}Ti_{0.80}$ which exhibits $\gamma = 6.9$ mJ/mol K^2 [177]. The jump in specific heat is higher than the value estimated according to the BCS theory, in other words, $\Delta C/\gamma T_c = 1.99$ while the weakly coupling BCS prediction equals to 1.43. This result proves not only the bulk character of superconductivity but also its strong-coupling character.

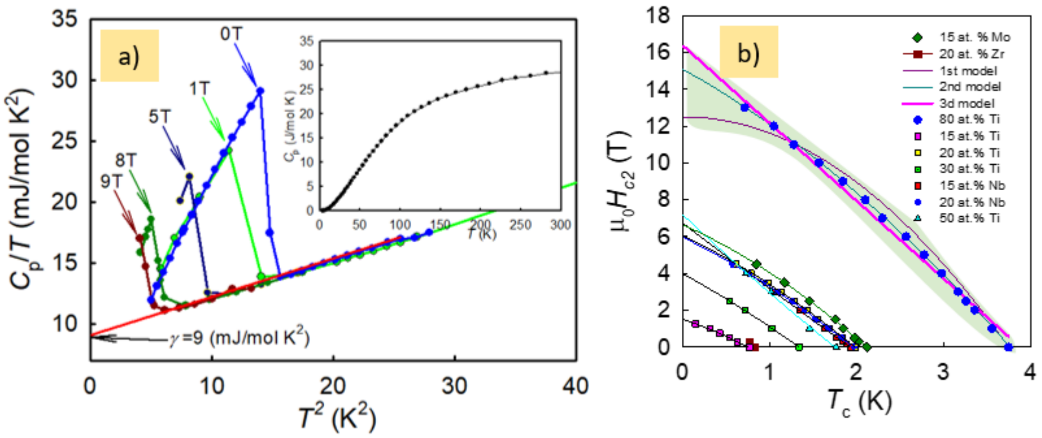

Fig. 7.18 (a) λ-type specific-heat anomaly observed on the $U_{0.20}Ti_{0.80}$ alloy measured in various magnetic fields $\mu_0 H$ (0 - 9 T). The inset presents the specific heat C_p (T) of the $U_{0.20}Ti_{0.80}$ alloy measured in $\mu_0 H = 0$. (b) The critical magnetic field H_{c2} vs the transition temperature T_c of the U-T alloys (T=Ti, Nb, Mo, Zr) with various concentrations of the transition metals T.

The H_{c2} vs. T_c plot representing the phase diagram of superconductivity of $U_{0.80}Ti_{0.20}$ in the context of U-rich alloys is given in the Fig. 7.18 (b). It is evident that $U_{0.80}Ti_{0.20}$ has the H_{c2} value dramatically higher. Can we estimate the extrapolated value in the low-temperature limit? The simple way is to use weak coupling theory and Werthamer-Helfand-Hohenberg (WHH) expression, giving the limit value H_{c2} (0) $\approx 0.7 \cdot T_c \cdot (-dH_{c2}/dT)$. The critical slope $-\mu_0 dH_{c2}/dT = (4.22 \pm 0.09)$ T/K, which gives $\mu_0 H_{c2}(0) \approx 11$ T ($-\mu_0 dH_{c2}/dT$ was obtained from the linear fit, Fig. 7.18 (b) “3rd model"). This disagrees with resistivity measurement, indicating that the material is still superconducting at $T_c = 0.67$ K in magnetic field $\mu_0 H = 13$ T. “The 1st model” plotted in the Fig. 7.18 (b) represents the fit of the data to a parabolic law $H_c(T) \approx$

$H_c(0)[1 - (T/T_c)^2]$ with $\mu_0H_{c2}(0) = (12.5 \pm 0.3)$ T. It apparently does not describe the experimental trend either. This all indicates the strong coupling situation at $U_{0.20}Ti_{0.80}$, for which no simple analytical form can be deduced. Relying on phenomenology without particular model, using a quadratic polynomial, including a linear term, better accounts for the linear part of the data. Good agreement was obtained with $\mu_0H_{c2}(0) = (16.35 \pm 0.23)$T ("2nd model" in the Fig. 7.18 (b)). For a compound with $T_c = 3.74$ K, this value is anomalously high. The obtained critical slope $-\mu_0 dH_{c2}/dT$ and critical field μ_0H_{c2} are close to the values reported for the Fermi liquid superconductor U_6Fe [$(-\mu_0 dH_{c2}/dT) = 3.42$ T/K and $\mu_0H_{c2}(0) = 10$ T], but actually such material well known for very high critical fields. One has to realize that the slope exceeding 2 T/K usually appears in high-field A15 and Chevrel-phase superconductors with transition temperature $T_c > 10$K [178].

7.2. *Crystal structure and magnetic properties of U-Ti and U-Nb hydrides*

7.2.1. Hydrogen induced changes of crystal structure

Investigation of the phase compositions of the U-Ti and U-Nb splats highlights the reduction of surface reactivity, showing up in much higher oxidation resistance of the alloys. Hydrogenation experiments show that alloying also increases the stability in a hydrogen atmosphere at ambient conditions. At hydrogen pressure of 0.1 MPa bulk U metal transforms into fine pyrophoric powder, while U-T (here T=Mo, Zr) splats require pressure of at least 0.45 MPa H_2 for the formation of the hydrides, which are stable in the air [174]. It looks like a property of the alloyed *bcc* U materials, therefore U-Ti and U-Nb splats were hydrogenated at 10 MPa, higher pressure reduces the time required for the reaction.

Hydrogenation of the U-Ti splats leads to the formation of a hydride with ≈3 H atoms per U, therefore the following notation will be used for identification of the hydrides with different concentrations of Ti: $(UH_3)_{1-x}Ti_x$, where $x = 0.10$; 0.15, 0.20, 0.25, 0.30. Analysis of the phase composition of the $(UH_3)_{1-x}Ti_x$ hydrides indicates that two forms of UH_3 hydride form. The main phase is the β-UH_3 form, the reflections of the phase are clearly visible on the diffraction patterns of $(UH_3)_{0.90}Ti_{0.10}$ and $(UH_3)_{0.85}Ti_{0.15}$ (see Fig. 7.19). The refined lattice parameter a_β for the phase in $(UH_3)_{0.90}Ti_{0.10}$ and $(UH_3)_{0.85}Ti_{0.15}$ hydrides equals to 6.608±0.001 Å and 6.613±0.002 Å, respectively. Even though Ti is smaller than U (1.47 Å and 1.56 Å, respectively), the lattice parameter stays constant or perhaps even slightly increases with increasing Ti concentration. This feature can be related with the presence of α-UH_3 phase (see Fig. 7.19). For the hydrides, the estimated content of the phase increases from ≈10 to ≈30 wt.%. We may tentatively assume that Ti diffuses into α-UH_3, which can be related to a small decrease of the lattice parameter a_α. For $(UH_3)_{0.90}Ti_{0.10}$ $a_\alpha = 4.131 \pm 0.001$ Å, while for $(UH_3)_{0.85}Ti_{0.15}$ $a_\alpha = 4.120 \pm 0.001$ Å. Another reason for unexpected lattice parameter variations can dwell in the partly polar character of metallic bonds. The electron transfer from U towards H can reduce the size of U atoms in a compound with H, while alloying T atoms would be affected less or not at all [45]. Hence Ti atoms could be actually larger than U atoms in compounds with hydrogen.

XRD patterns show that the hydrides produced from the splats with the dominant γ-U phase tend to lose crystallinity. The change of the crystalline size is already visible for the hydrides with 10 and 15 at.% of Ti, as reflected in the XRD peak broadening (see Fig. 7.19). For these hydrides the crystallite size of α-UH_3 changes from ≈300 Å to ≈150 Å, for β-UH_3 it changes from ≈250 Å to ≈180 Å. A dramatic change of the crystalline size happens at 20 at.% Ti, as $(UH_3)_{0.80}Ti_{0.20}$ exhibits the average grain size only ≈60 Å (obtained from the refinement of the X-ray pattern in MAUD software described here [179]). And this tendency continues further. The pair distribution function analysis revealed that $(UH_3)_{0.70}Ti_{0.30}$ contains nanocrystals with the size of ≈20 Å. The three low angle peaks of β-UH_3 are transformed into broad single-peak located between 20° and 40°. The sharp tip of the peak comes from the XRD pattern of α-UH_3 with much larger gran size, see Fig. 7.19.

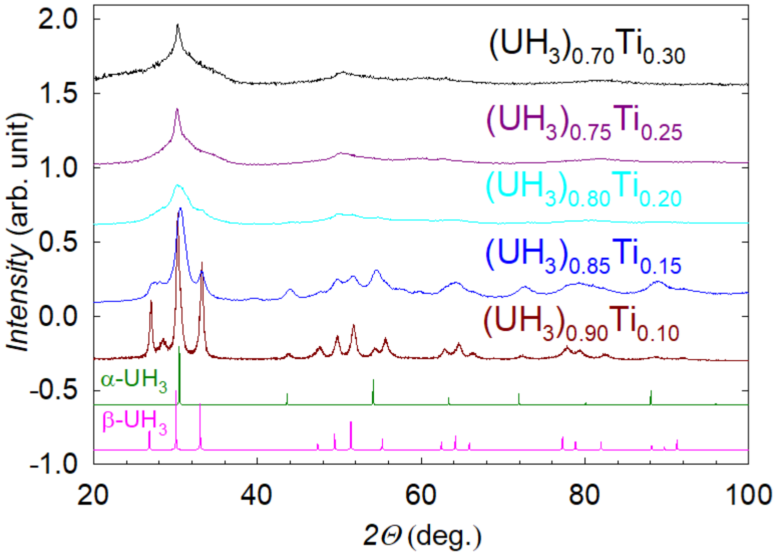

Fig. 7.19 X-ray diffraction patterns of U hydrides with different content of Ti. The two bottom plots correspond to the simulated patterns of α-UH_3 (a_α = 4.142 Å) and β-UH_3 (a_β = 6.643 Å).

The crystallinity of the U-Ti hydrides with Ti concentration ≥ 20 at. % is similar to the Mo-alloyed hydride $(UH_3)_{0.85}Mo_{0.15}$, it also exhibits several broad peaks which were initially perceived as a sign of amorphization (see Fig. 7.20). XRD pattern of the hydride was simulated assuming the β-UH_3 structure and grain size of 8 and 13 Å [174], later transmission electron microscope study confirmed nanocrystalinity of $(UH_3)_{0.85}Mo_{0.15}$. From the comparison presented in Fig. 7.20 it is clear that U-Ti hydrides are different from $(UH_3)_{0.80}Zr_{0.20}$, which is single-phase α-UH_3. The fact that the diffraction study does not show Ti metal segregation indicates that the doping elements remain in the lattice of the hydrides.

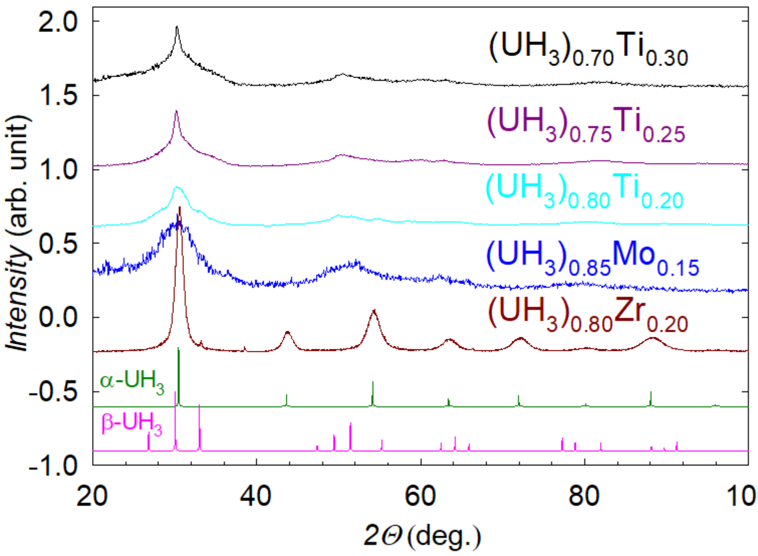

Fig. 7.20 Comparison of the X-ray diffraction patterns of U-Ti hydrides with nanocrystalline $(UH_3)_{0.85}Mo_{0.15}$ and crystalline $(UH_3)_{0.80}Zr_{0.20}$.

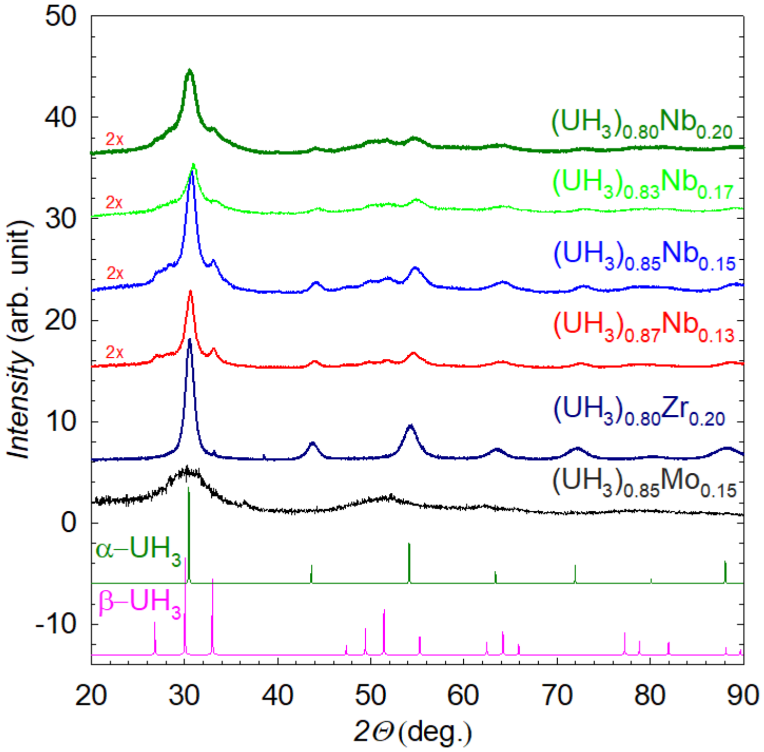

Fig. 7.21 X-ray diffraction patterns of U hydrides with different concentration of Nb compared with nanocrystalline $(UH_3)_{0.85}Mo_{0.15}$ and crystalline $(UH_3)_{0.80}Zr_{0.20}$. The two bottom plots correspond to the simulated patterns of α-UH_3 (a_α = 4.142 Å) and β-UH_3 (a_β = 6.643 Å).

The U-Nb hydrides exhibit structure tendencies similar to the U-Ti hydrides. $(UH_3)_{0.87}Nb_{0.13}$ contains both α-UH_3 and β-UH_3 phases, which are present in the respective fraction of 40 and 60 wt.%. The lattice parameters $a_\alpha = 4.122 \pm 0.002$ Å and $a_\beta = 6.116 \pm 0.002$ Å are smaller than for the undoped hydrides [38]. Analysis of the diffraction data of $(UH_3)_{0.85}Nb_{0.15}$ and $(UH_3)_{0.83}Nb_{0.17}$ indicates that Nb continues to stay in the hydride lattice, the lattice parameters show further decrease to, respectively, $a_\alpha = 4.107 \pm 0.001$ Å and $a_\beta = 6.605 \pm 0.002$ Å and $a_\alpha = 4.101 \pm 0.001$ Å and $a_\beta = 6.597 \pm 0.002$ Å. The relative intensity of the α-UH_3 peaks is also reduced, the estimated content of α-UH_3 changes from to 35% and 30% (see Fig. 7.21). $(UH_3)_{0.80}Nb_{0.20}$ also contains α-UH_3 and β-UH_3 phases, but the low background/peak intensity ratio makes the estimate of the phase composition and lattice parameters less reliable. The grain size of β-UH_3 dramatically changes at 15 at.% Nb doping. For $(UH_3)_{0.87}Nb_{0.13}$ it equals ≈120 Å, starting from $(UH_3)_{0.85}Nb_{0.15}$ it remains on the level of ≈50 Å. It does not reach nanocrystallinity of $(UH_3)_{0.85}Mo_{0.15}$.

7.2.2. Magnetic properties of the U-Ti and U-Nb hydrides

U-alloys are usually weak Pauli paramagnets which superconduct at low temperature (for more details, see section 7.1.1.). Measurements of the magnetic susceptibility of $U_{0.70}Ti_{0.30}$ and $U_{0.10}Ti_{0.90}$ indicate no magnetic order. In contrast, hydrides of the U-Ti alloys order magnetically. The temperature dependences of magnetization measured in different fields indicate that all U-Ti hydrides exhibit a ferromagnetic transition (see Fig. 7.22 (a-f)). The data obtained in the field of 0.05 T were used for determination of the Curie temperatures T_C. Its value changes non-monotonously as a function of Ti concentration (see Fig. 7.23 (a)). $(UH_3)_{0.90}Ti_{0.10}$ orders below ≈175 K. Increase of the Ti concentration increases the transition temperature, $(UH_3)_{0.85}Ti_{0.15}$ becomes ferromagnetic at $T_C \approx 182$ K, which is the highest transition temperature observed within the series. This hydride also exhibits a weak ferromagnetic impurity which sets in around 280 K. The impurity phase was not identified from the X-ray diffraction studies. It is clear that the contribution of the impurity magnetization results in the irreversibility of the zero field cooled (ZFC) and field cooled (FC) $M(T)$ curves around the transition temperature (see Fig. 7.22 (b)), for the hydrides with 10, 20, 25 and 30 at.% of Ti the ZFC and FC curves coincide which excludes the possibility of spin-glass transition (see Fig. 7.22 (a, c, d, f)).

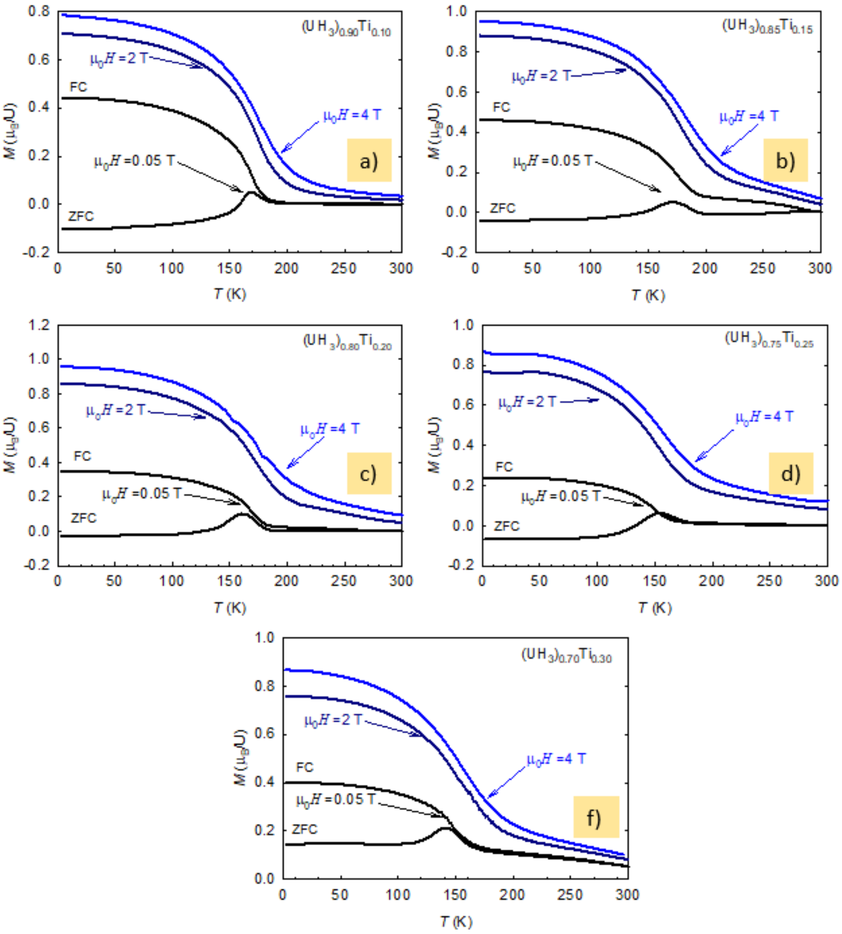

Fig. 7.22 Temperature dependences of magnetization of $(UH_3)_{1-x}Ti_x$ measured in various magnetic fields (0.05 T; 2 T; 4 T). $\mu_0 H = 0.05$ T was applied for investigation of the magnetization in zero field cooled (ZFC) and field-cooled regimes. Magnetization curves indicate that hydrides exhibit ferromagnetic ordering with the range of Curie temperatures of 150-180 K.

For the hydrides with Ti concentration over 20 at.% the transition temperatures gradually decrease: 1) $(UH_3)_{0.80}Ti_{0.20} \rightarrow T_C \approx 173$ K; 2) $(UH_3)_{0.75}Ti_{0.25} \rightarrow T_C \approx 155$ K; 3) $(UH_3)_{0.70}Ti_{0.30} \rightarrow T_C \approx 151$ K. Comparison of the temperature dependences of magnetization $M(T)$ of $(UH_3)_{1-x}T_x$ (T = Mo, Zr, Ti, Nb) measured in $\mu_0 H = 0.05$T shows that hydrides with Ti undergo transition at the lowest temperatures (see Fig. 7.23 (b)) In general the magnetization measured in 0.05, 2 and 4 T (field cooled mode) increases with decreasing temperature, only $(UH_3)_{0.75}Ti_{0.25}$ exhibits slight reduction of $M(T)$ noticeable in fields of 2 and 4 T. This effect can be possibly explained by increasing magnetic anisotropy with decreasing T, which would turn some of the moments from the direction of the field to an easy magnetization direction. It could be also related to a magnetic impurity, as e.g. solid oxygen in the chamber, with ordering temperature close to 50 K. A similar effect was observed in the magnetization dependencies of some $(UH_3)_xMo_{1-x}$ hydrides [180]. Another noticeable feature is the magnetic impurity of $(UH_3)_{0.70}Ti_{0.30}$ with T_C close to 300 K, best visible in the magnetization measured in 0.05 T. The fact that 2 and 4 T suppresses the contribution of the impurity phase explains the reason why it is not seen in X-ray diffraction data, the amount of the phase is small.

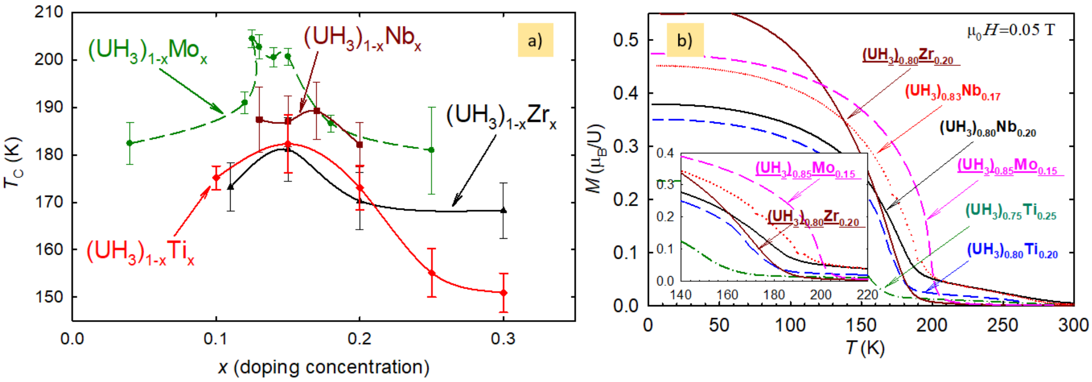

Fig. 7.23 (a) Dependencies of the Curie temperatures vs. concentrations of the transition elements in $(UH_3)_{1-x}T_x$. The Curie temperatures were defined as the mean value between the inflection point of the $M(T)$ dependence in 0.05 T and the intersection point of the tangent (i.e., extrapolation of the highest slope) with the baseline. (b) comparison of the temperature dependences of magnetization $M(T)$ measured in $\mu_0 H = 0.05$ T. The inset presents details in the range 0-0.4 μ_B/U and 140-220 K.

The temperature dependencies of magnetic susceptibility $\chi(T)$ allowed determining the effective paramagnetic moment (μ_{eff}) and paramagnetic Curie temperature Θ_p. Due to the presence of high-temperature ferromagnetic impurity susceptibility measured in 4T and a short temperature range was used for evaluation of the values. Paramagnetic Curie temperature of $(UH_3)_{0.80}Ti_{0.20}$ is ≈17 K higher than T_C, this hydride exhibits $\Theta_p = 189.6 \pm 1.7$ K and $\mu_{eff} = 3.4 \pm 0.4$ μ_B/U. For $(UH_3)_{0.70}Ti_{0.30}$ considerable decrease of Θ_p down to 159.6 ±1.9 K is accompanied by an increase of μ_{eff} up to 3.9±0.5 μ_B/U. While the estimation of Θ_p looks reliable the values of the effective magnetic moments are significantly higher than reported for $(UH_3)_{1-x}Mo_x$ [180], our estimation of the value for the hydrides with 15 and 18 at.% of Mo respectively gives μ_{eff} of 2.6 and 2.5 μ_B/U, which are close to the data given for β-UH_3 [136]. Much higher values of the effective moments of $(UH_3)_{1-x}Ti_x$ are related to the fact that magnetic susceptibility of the hydrides was affected by the ferromagnetic impurity, it reduced reliability of the Curie constant.

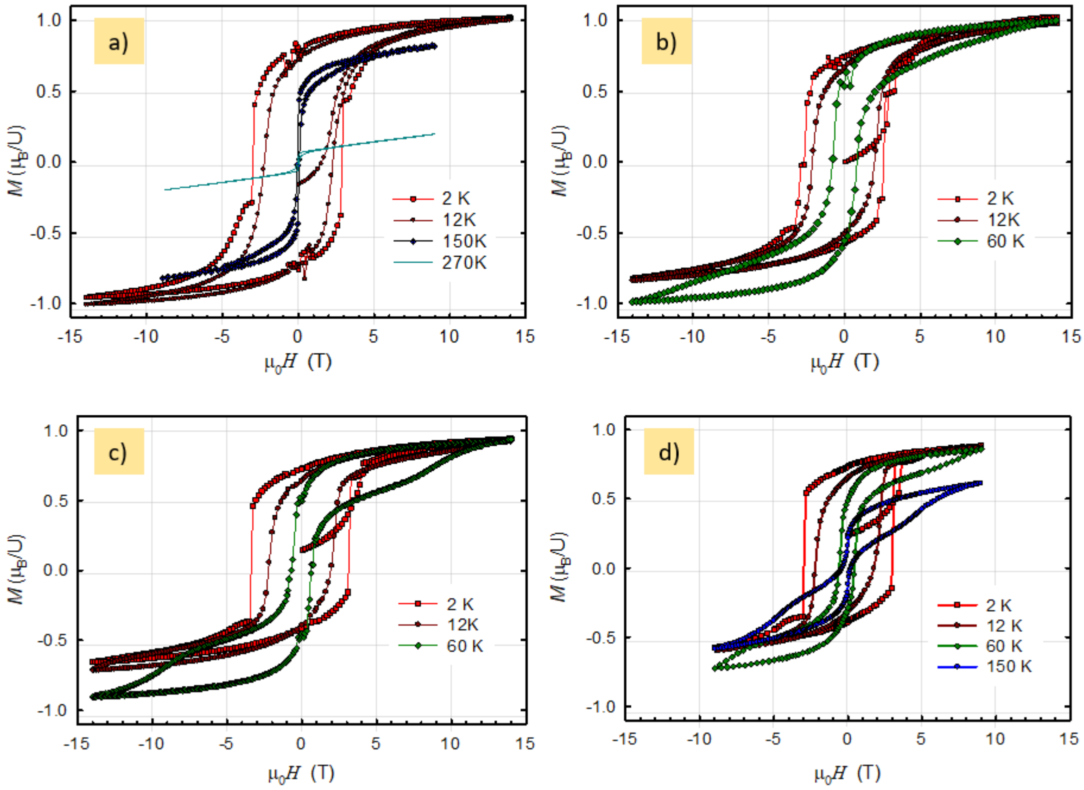

Fig. 7.24 Field dependencies of magnetization measured at different temperatures: 1) (UH$_3$)$_{0.85}$Ti$_{0.15}$; 2) (UH$_3$)$_{0.80}$Ti$_{0.20}$; 3) (UH$_3$)$_{0.75}$Ti$_{0.25}$; 4) (UH$_3$)$_{0.70}$Ti$_{0.30}$.

Field dependence of magnetization measured in various temperatures indicate that U-Ti hydrides exhibit wide hysteresis loops (see Fig. 7.24). The maximum coercive field was naturally observed in the lowest temperature (2 K). There is no systematic change of the coercive field of the hydrides with the raise of the Ti concentration. It is better seen from a comparison present on Fig. 7.25 (a). The maximum coercive field was observed for (UH$_3$)$_{0.75}$Ti$_{0.25}$ (≈ 3.4 T), the minimum for (UH$_3$)$_{0.80}$Ti$_{0.20}$ (≈ 2.6 T). There are two primary sources of the large coercivity of the studied materials: 1) pinning of the small domain walls on defects; 2) random distribution of easy-magnetization direction. While the first source is common for all ferromagnetic materials, the second one can be attributed to nano-crystalline and amorphous materials which exhibit high disorder. In the hydrides the second mechanism should play a distinctive role according to the crystal structure analysis.

Field dependencies of the U-Ti hydrides are similar to U-Mo hydrides [90] which exhibit slow saturation with a single remagnetization step in the negative and positive field (see Fig. 7.25 (a)). On the other hand, U-Zr hydrides [45] with α-UH_3 type of structure display a sequence of erratic steps. The comparison of the hysteresis loops of U-Ti, U-Mo and U-Zr hydrides is present in Fig. 7.25 (d), it highlights the similarity between U-Ti and U-Mo hydrides. Magnetization loops of the discussed hydrides are similar to the so-called HARD materials (High Anisotropy Random Distribution) [181]. The step-like change of the magnetization can be explained by the simultaneous remagnetization of exchange-coupled grains [45]. Slow saturation followed by the magnetization steps were also observed in the virgin curves of all U-Ti hydrides (see Fig. 7.26 (a) where the virgin curve of $(UH_3)_{0.85}Ti_{0.15}$ is present). An increase of temperature gradually shrinks the loops and removes the steps, which suggest easy thermal activation of the domain walls. The decreasing coercive fields with temperature increase follow $-aT^{1/2}$ introduces in the Egami model which testifies thermal activated movements of domain walls [182], but the low temperature saturation predicted by the Egami model is not present in our data (see Fig. 7.26 (b)).

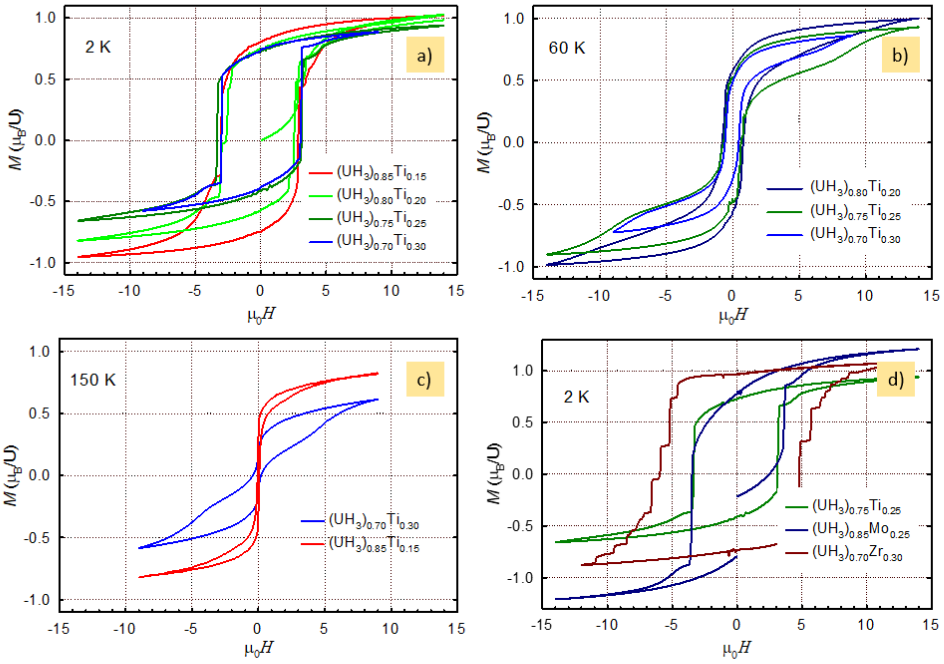

Fig. 7.25 (a-c) Comparison of the hysteresis loops of U-Ti hydrides measured at various temperatures. (d) Hysteresis loop of $(UH_3)_{0.75}Ti_{0.25}$ compares with nanocrystalline $(UH_3)_{0.85}Mo_{0.15}$ and crystalline $(UH_3)_{0.70}Zr_{0.30}$.

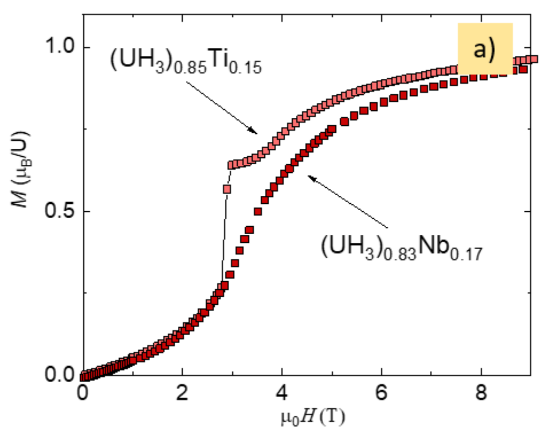

Fig. 7.26 (a) Virgin curve of $(UH_3)_{0.85}Ti_{0.15}$ and $(UH_3)_{0.83}Nb_{0.17}$. (b) Values of the coercive fields on the U-Ti hydrides follow the $1-\eta T^{1/2}$ scaling.

For quantification of the materials we also defined saturation magnetization M_S. Experimental data reasonably well scale to $1/H^2$, therefore a phenomenological relation accounting for anisotropy $M(H)=M_S[1-a/(c+H)^2]$ was used for the description of the descending branch of the hysteresis loops. The estimated saturation moments do not deviate much from 1 μB/U: M_S equals 1.05 μB/U, 1.0 μB/U and 0.95 μB/U for $(UH_3)_{0.80}Ti_{0.20}$, $(UH_3)_{0.75}Ti_{0.25}$, $(UH_3)_{0.70}Ti_{0.30}$, respectively.

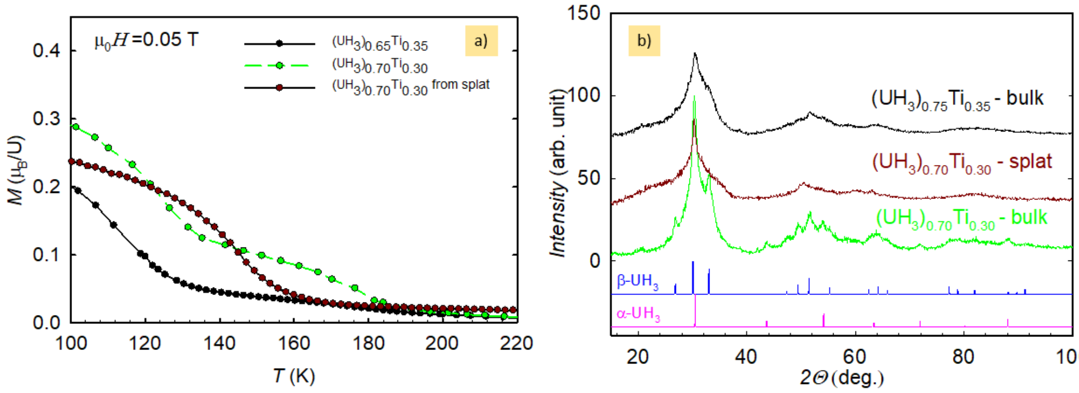

Fig. 7.27 (a) Temperature dependences of magnetization $M(T)$ of hydrides synthesizes from bulk $U_{0.70}Ti_{0.30}$ and $U_{0.65}Ti_{0.35}$ and splat $U_{0.70}Ti_{0.30}$. (b) Comparison of the X-ray diffraction patterns of the hydrides shown on $M(T)$ dependence (left panel).

Investigation of the hysteresis loops of the U-Ti hydrides measured at 150 K indicates that their shapes are considerably different (see Fig. 7.25 (c)). Hysteresis loop of $(UH_3)_{0.85}Ti_{0.15}$ is considerably narrower in comparison to $(UH_3)_{0.70}Ti_{0.30}$ (respective coercive fields are $H_c \approx 0.05$ and $H_c \approx 0.39$). $(UH_3)_{0.70}Ti_{0.30}$ exhibits a change in the slope which appears symmetrically (around $|\mu_0 H| \approx 5$ T). The first possible reason for the anomaly is the presence of not hydrogenated material (which is paramagnetic), the exchange coupling between ferromagnetic and paramagnetic component can lead to the non-monotonous change of *M*(*H*), such effect was observed on U-V hydrides with identified V particles [183]. The other sources of the anomaly can be a soft ferromagnetic phase or inhomogeneous distribution of the alloying element which results in the distribution of the Curie temperatures within one specimen. For clarification of this issue hydrides of the bulk $U_{0.70}Ti_{0.30}$ and $U_{0.65}Ti_{0.35}$ alloys were studies. *M*(*T*) dependence measured at 0.05 T shows that splat-$(UH_3)_{0.70}Ti_{0.30}$ exhibits a broad transition from 160 to 140 K, on the other hand, *M*(*T*) of the bulk-$(UH_3)_{0.70}Ti_{0.30}$ two ferromagnetic transitions. The first one sets in between 185 and 175 K, the second one becomes visible below 145 K (see Fig. 7.27 (a)). Despite the presence of the two phases in the bulk-$(UH_3)_{0.70}Ti_{0.30}$ its 150 K hysteresis loop looks like the one of $(UH_3)_{0.85}Ti_{0.15}$, the ferromagnetic phase which sets in below 145 K does not influence it in the way that was observed for splat-$(UH_3)_{0.70}Ti_{0.30}$. This suggests that chemical inhomogeneity and the presence of paramagnetic phase do not influence *M*(*H*) considerably. Comparison of the X-ray diffraction patterns of the hydrides indicates that a significant decrease of the crystallite size (from 70 Å to 20 Å) can account for the anomalous *M*(*H*) (see Fig. 7.27 (b)). The other interesting finding is related to the hydride of bulk $U_{0.65}Ti_{0.35}$ ($(UH_3)_{0.65}Ti_{0.35}$), the increase of the Ti concentration removes α-UH_3 phase from the X-ray diffraction pattern (see Fig. 7.27 (b)), which also diminish the magnetic phase which orders below 185 K. It allows to assume that the phase is of α-UH_3 type and it does not accommodate Ti as easy as β-UH_3 type, because its transition temperature locates close to the reported one.

U-Nb hydrides are also ferromagnetic, their Curie temperatures T_C changes nonlinearly with the increase of Nb concentration (see Fig. 7.23 (a)), we do not observe the broad maximum in the concentration dependence of T_C as for the U-Ti, U-Mo and U-Zr hydride. The main reason is that only hydrides with Nb concentration ≥ 13 at.% were studies. Nb alloying from 13 to 17 at.% is almost not reflected in the transition temperature, it respectively changes from 187.4 K to 189.2 K. $(UH_3)_{0.80}Nb_{0.20}$ orders below ≈182, which is the largest of temperature change in the series. U-Nb hydrides also exhibit ferromagnetic impurity which sets in around 260 K and results in the irreversibility of the zero-field cooled (ZFC) and field cooled (FC) *M*(*T*) curves around the transition temperature (see Fig. 7.28 (a-d)).

Paramagnetic Curie temperature of U-Nb hydrides decreases with the increase of Nb concentration. $(UH_3)_{0.87}Nb_{0.13}$ exhibits Θ_p =213.7 ± 1.1 K and μ_{eff} = 2.25 ± 0.1 μ_B/U. For $(UH_3)_{0.85}Nb_{0.15}$ the values equal Θ_p =210.7 ± 0.9 K and μ_{eff} = 2.54 ± 0.1 μ_B/U. $(UH_3)_{0.83}Nb_{0.17}$ exhibits a slight decrease of paramagnetic Curie temperature which equals to 211.8 ± 1.1 K, while effective moment further increases μ_{eff} = 2.67 ± 0.1 μ_B/U). The changes can be followed from the fits of $\chi(T)$ presented on Fig. 7.29, the change of Θ_p follows the change of T_C. Effective moments of the hydrides with Nb concentration <20 at.% are close to the moments of U-Mo hydrides [180] falling into the range of 2.2-2.7 μ_B/U. For $(UH_3)_{0.80}Nb_{0.20}$ we found that Θ_p dramatically drops to 193.2 ± 1.5 while effective moment becomes overestimated (≈3.6 ± 0.2 μ_B/U). This effect can be related to the influence of the ferromagnetic impurity which affected $\chi(T)$ in the range studied.

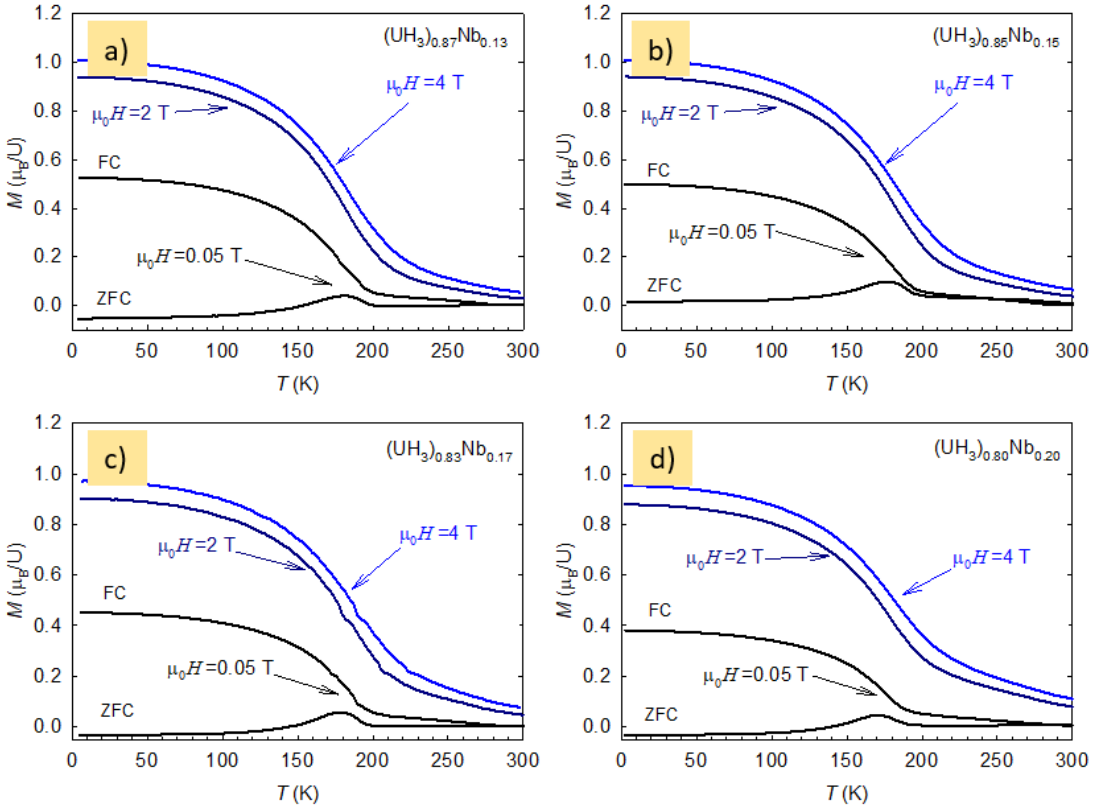

Fig. 7.28 $M(T)$ dependences of $(UH_3)_{1-x}Nb_x$ measured in various magnetic fields (0.05 T; 2 T; 4 T). μ_0H=0.05 T was applied for investigation of the magnetization in zero field cooled (ZFC) and field-cooled regimes. Magnetization curves indicate that hydrides exhibit ferromagnetic ordering with the range of Curie temperatures of 180-190 K.

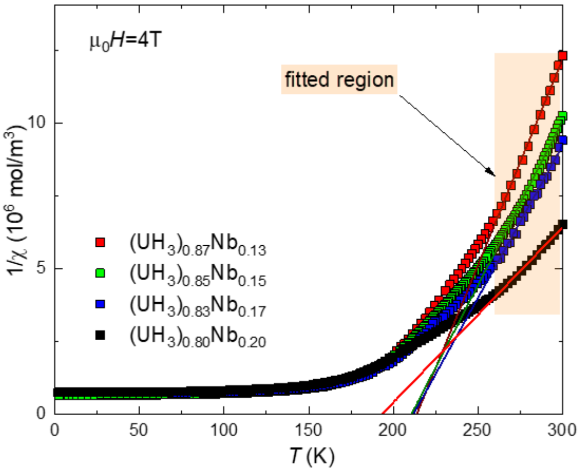

Fig. 7.29 Temperature dependence of the magnetic susceptibility $\chi(T)$ of U-Nb hydrides measured in $\mu_0 H = 4$ T (in field-cooled mode). The data in the temperature range from 260 to 300 K were used for the determination of the paramagnetic moment (μ_{eff}) and paramagnetic Curie temperature Θ_p.

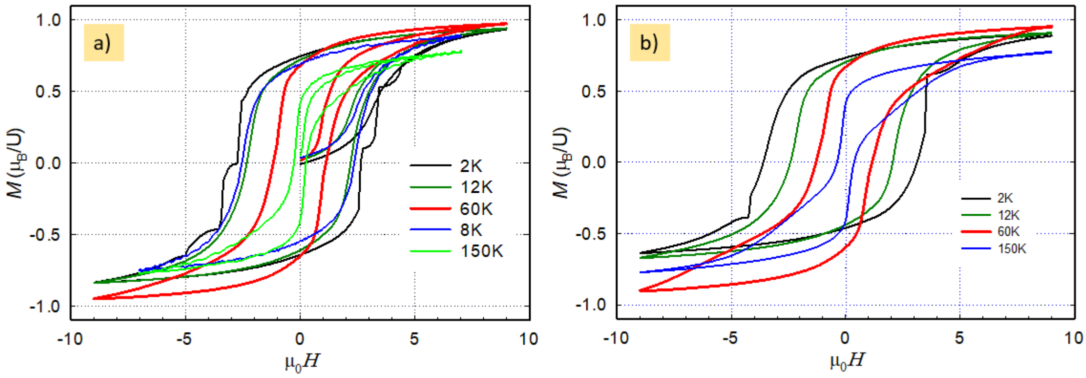

Fig. 7.30 Field dependencies of magnetization M($\mu_0 H$) measured at different temperatures: a) $(UH_3)_{0.83}Nb_{0.17}$; b) $(UH_3)_{0.80}Nb_{0.20}$.

Investigation of the field dependences of magnetization of U-Nb hydrides indicates that they exhibit wide hysteresis loops with a shape which is similar to the U-Ti and U-Mo hydrides. The coercive field observed at 2 K changes from 2.7 T (measured on $(UH_3)_{0.83}Nb_{0.17}$) to 3.65 T (measured on $(UH_3)_{0.80}Nb_{0.20}$, see Fig. 7.30). The widths of the corresponding hysteresis loops decrease with the increase of the temperature. While the 2 K hysteresis loop of $(UH_3)_{0.83}Nb_{0.17}$ exhibits two steps in the change of magnetization (see Fig. 7.30 (a)), $(UH_3)_{0.80}Nb_{0.20}$ exhibits a monotonous decrease of magnetization in the decreasing field with small step-change (in increasing field the step change is larger). The hysteresis loops measured at 12 K do not exhibit sudden change of the magnetization, at this temperature they are very similar to the U-Ti hydrides. It suggests that the main mechanisms responsible for the anomalies in the

2 K hysteresis loops are the same for all studied hydrides. Nevertheless, they exhibit a different degree of thermal activation, in other words, 2 K is enough for reduction of the coherence length of the coupling between grains in $(UH_3)_{0.80}Nb_{0.20}$, for U-Ti and U-Mo hydrides grains remain coupled leading to sharp remagnetization. The other reason for the difference can be related to the differences in the amount of glue used for the fixation of the measured powder. The same explanation applies for the difference in the virgin curve of $(UH_3)_{0.83}Nb_{0.17}$ and $(UH_3)_{0.85}Ti_{0.15}$. In contrast to the later hydride $(UH_3)_{0.83}Nb_{0.17}$ exhibits a "continuous" change of magnetization with the increasing field (see Fig. 7.26 (a)). Hysteresis loops of U-Nb hydrides measured at 60 and 150 K are also very similar (see Fig. 7.30). Estimated values of saturation magnetization M_S are close to values defined for U-Ti hydrides. $M_S \approx 0.98\ \mu_B$/U for $(UH_3)_{0.83}Nb_{0.17}$ and $M_S \approx 0.99\ \mu_B$/U for $(UH_3)_{0.80}Nb_{0.20}$.

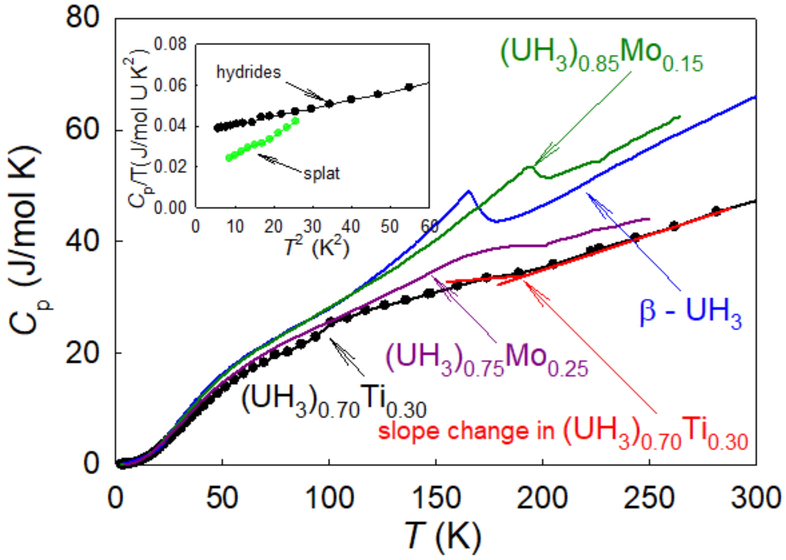

Fig. 7.31 Temperature dependencies of specific heat of $(UH_3)_{0.70}Ti_{0.30}$, $(UH_3)_{0.85}Mo_{0.15}$ [180] and β-UH_3 [38]. The red lines indicated the change of the slope of $(UH_3)_{0.70}Ti_{0.30}$ above the transition temperature. The inset presents the comparison of C_p/T vs. T for the hydride and splat with 30 at.% of Ti.

In order to summarize this section, let us look at the change of the properties of the hydrides with alloying. The effect of the lattice expansion of *bcc* U-Ti alloy upon hydrogenation is best seen in the change of the low-temperature specific heat. Inset of Fig. 7.31 presents the data measured on hydride and splat with 30 at.% of Ti, in the C_p/T vs. T representation, we clearly see the doubling of the Sommerfeld coefficient γ from 15.6 mJ/ mol U K^2 (for splat) to 36 6 mJ/ mol U K^2 (for hydride, 1.6

mJ/ mol K^2 contributes Ti taking into account that its γ = 3.35 mJ/ mol K^2 [3]). Later value is close to γ measured on β-UH_3 (29 mJ/mol K^2 [184] or 33.9 mJ/mol K^2 [42]). The presence of the impurity of the α-UH_3 form should not influence the result, recent study of $(UH_3)_{0.80}Zr_{0.20}$ hydrides which exhibit α-UH_3 structure reveals γ of 32.2 mJ/mol U K^2, which highlights the similarity of the density of electronic states at the Fermi level in α-UH_3 and β-UH_3 [45]. From the perspective of the specific heat modifications $(UH_3)_{0.70}Ti_{0.30}$ is similar to $(UH_3)_{0.75}Mo_{0.25}$ and $(UH_3)_{0.70}Zr_{0.30}$ which exhibit $\gamma \approx$ 34 mJ/mol U K^2. The enhancement of the Sommerfeld coefficient points out to an increase of density of states at the Fermi level which is usually attributed to the increase of the U-U spacing and 5*f* band narrowing [180]. High-temperature specific heat of $(UH_3)_{0.70}Ti_{0.30}$ does not display distinct anomaly at the transition temperature like β-UH_3 and $(UH_3)_{0.85}Mo_{0.15}$. Nevertheless, there is a considerable change in the slope of C_p (T) below 185 K, close to the ferromagnetic ordering (see Fig. 7.31).

The change of the transition temperature T_C with concentration for U-Nb and U-Ti hydrides exhibit the same tendencies which were observed for U-Mo and U-Zr hydrides (see Fig. 7.23 (a)). Curies temperature increases to the critical concentration of transition element (≈13-17 at.%), then it reduces. The first idea would be to assume that due to the large overlap of the U-5*f* and Ti-3*d* (Nb-4*d*) energies we can expect a strong hybridization of the respective electron bands and corresponding modification of the magnetic properties. On the other hand, it looks like the concentration of the transition element rather than the element itself plays a significant role. Theoretical studied highlight that in U hydrides 5*f*-6*d* hybridization is significantly reduced in contrast to U metal. It is also pointed out that U-6*d* states are moved deep below the Fermi level and hybridize with H-1*s* electrons [29]. Therefore, at low concentrations alloying could support the positive effect of the depopulation of the 6*d* states due to the increase of the U to H ratio, but above the critical concentration 5*f* and 3*d* (4*d*) hybridization becomes detrimental, which was suggested in our recent paper [183].

7.3. Physical properties of hydrogen-stabilized UTi_2H_x

This subchapter is based on the following articles:

1. *"Laves phase UTi_2 stabilized by hydrogen and its magnetic properties"* which is published in Phys. B Condens. Matter. by V. Buturlim, L. Havela, S. Sowa, M. Paukov, D. Drozdenko, M. Dopita, P. Minarik, S. Mašková (2017, doi:10.1016/J.PHYSB.2017.10.027.
2. *"Spin fluctuations in hydrogen-stabilized Laves phase UTi_2H_5"* which is published in Philos. Mag. by V. Buturlim, M. Falkowski, M. Paukov, O. Koloskova, D. Drozdenko, M. Dopita, P. Minárik, S. Mašková, P. Doležal, L. Havela (2019, doi: 10.1080/14786435.2019.1605222

7.3.1. Crystal structure of $U_{0.30}Ti_{0.30}$ and $U_{0.34}Ti_{0.66}$

Preparation of splats was successful for Ti concentrations ≤ 50 at.%, for alloys with higher concentration we hydrogenated bulk specimens. XRD patterns were measured from the cut surfaces of the specimens and fitted using the MAUD software package [179]. Fig. 7.32 (a) illustrates the XRD patterns of the U-Ti alloys with 66 at.% of Ti, for comparison study of the alloy with 30 at.% of Ti was also performed. The U_2Ti phase is formed in the case of $U_{0.34}Ti_{0.66}$ ($a = b = 4.822$ Å, $c = 2.860$ Å), but there is some intensity discrepancy for (110) and (101) peaks. The structural analysis which takes into account the presence of the *bcc* U-Ti solid solution with $a = 3.343$ Å improved the quality of the refinement and partly removed the inconsistency of the simulated and experimental intensities (see Fig. 7.32 (b)). It is worth to mention, that U_2Ti is the only one intermetallic compound present in the phase diagram of U-Ti system, it exhibits structure type AlB_2 (sp. gr. *P6/mmm* [185]). On the other hand, the diffraction pattern of the bulk $U_{0.70}Ti_{0.30}$ exhibits a mixture of two phases, namely U_2Ti and α-U, in the approximate ratio of 8 to 1. An increase of the U amount leads to an increase of the lattice parameters for U_2Ti ($a = b = 4.84$ Å, $c = 2.848$ Å), in the same time the "intensity problem" disappears. α-U has $a = 2.853$ Å, $b = 5.852$ Å, $c = 4.959$ Å. The results qualitatively correspond to the equilibrium phase diagram (see Fig. 4.4 (a)).

On the contrary to the information from Ref. [185], the room temperature hydrogenation of $U_{0.70}Ti_{0.30}$ (which contains U_2Ti) led to the formation of the hydride which consists of nano-crystalline β-UH_3-based material (a = 6.635 Å) accompanied by a smaller fraction of α-UH_3 type (a = 4.147 Å). This hydride is presented on Fig. 7.33 (a) and marked as $(UH_3)_{0.70}Ti_{0.30}$. The nanocrystalline type of structure is analogous to the hydrides of the *bcc* U splats with Ti, Nb (described earlier) and Mo [186].

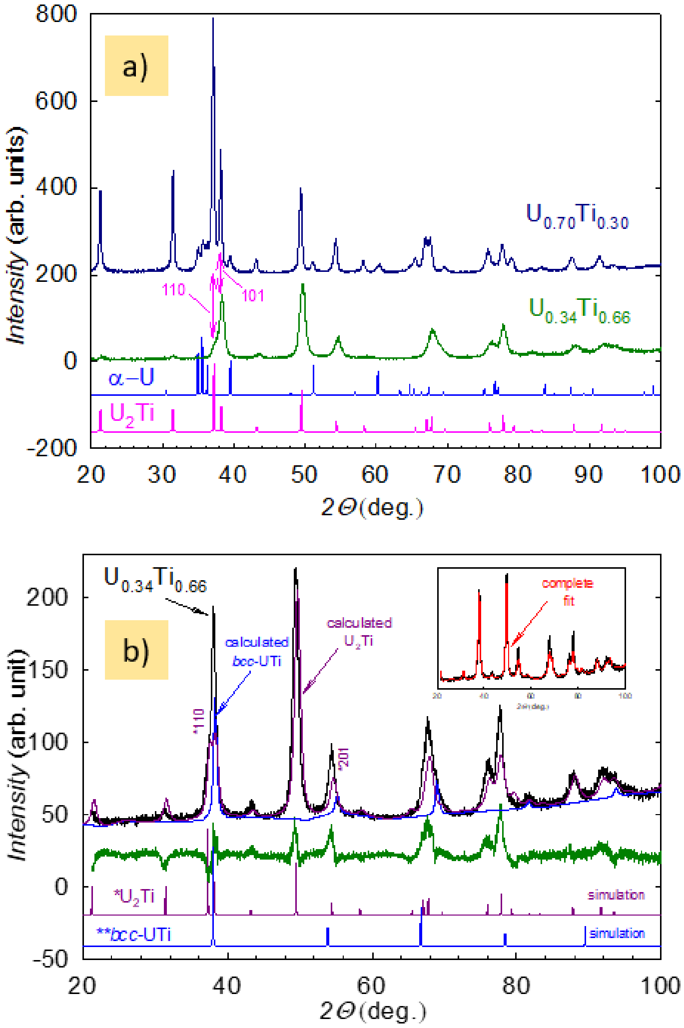

Fig. 7.32 (a) XRD patterns of the bulk U-Ti alloys with 66 and 30 at.% of Ti. The bottom plots represent simulated patterns of U_2Ti and α-U. (b) Refinement of the structure of $U_{0.34}Ti_{0.66}$ which takes into account the presence of U_2Ti and *bcc* U-Ti solid solution.

The hydrogenation of the ingot with the same concentration of Ti (30 at.%) at high temperatures produces the hydride, which has a structure of conventional β-UH_3 (a = 6.643 Å), with spurious UO_2 and UC phases (brown patter on Fig. 7.33 (a)). We also identified a small amount of an additional phase, which can be defined as the cubic Laves phase UTi_2 (sp. gr. *Fd*-3*m*), taking a = 8.578 Å. We assume that it is the hydride reported in [144]. It is essential to highlight that UTi_2 is not present in the equilibrium phase diagram of U-Ti system. Further, we intend to show that it was stabilized by the presence of hydrogen, which cannot be detected by XRD. Hence we label it as UTi_2H_x. As properties of such new Laves phase were so far unknown (only structure reported in the reference above), it was tempting to focus on synthesis and study of this material, affiliated to the group of well-known uranium Laves phases, believed to be complete and studied thoroughly.

A much higher fraction of UTi_2H_x was obtained by the hydrogenation of a precursor $U_{0.34}Ti_{0.66}$, which was itself multiphase. The technical details of the hydrogentation are described in section 6.1.3.3. The majority phase in (I) $U_{0.34}Ti_{0.66}H_x$ is the Laves phase, again with $a = 8.588$ Å. However, in this case the desired hydride is contaminated by β-UH_3. Application of high H_2 pressure at the synthesis of (II) enhanced the amount of β-UH_3 while the peaks of UTi_2H_x became broader (see Fig. 7.33 (a)). The last sample, (III) $U_{0.34}Ti_{0.66}H_x$, does not contain UH_3, but α-U ($a = 2.859$ Å, $b = 5.850$ Å, $c = 4.969$ Å) is present as a spurious phase. This was confirmed by the energy dispersive microanalysis (EDX) using the scanning electron microscope (SEM) Zeiss Auriga (see Fig. 7.33 (b)). The EDX line profiles, although somewhat shifted to the left, clearly identify the white grains as the U-rich (Ti poor) regions. These uranium clusters are inhomogeneously distributed through the whole volume of (III) $U_{0.34}Ti_{0.66}H_x$.

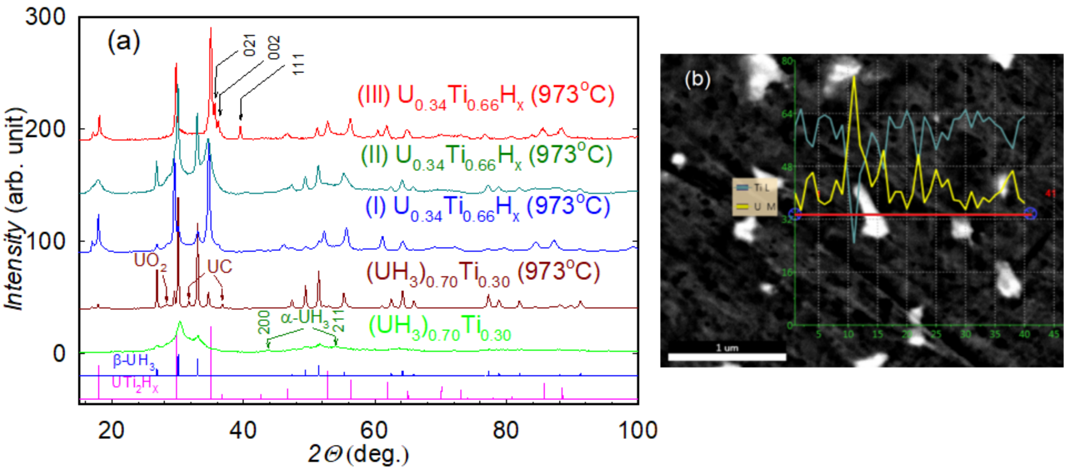

Fig. 7.33 (a) XRD patterns of the hydrides obtained using various synthesis routes: 1) light green plot - hydride produced by room temperature hydrogenation; 2) brown, blue, green and red plots correspond to hydrides obtained by high-temperature hydrogenation. The black arrows indicate the α-U reflections, the green ones

correspond to α-UH_3. (b) Backscattered electron image of (III) $U_{0.34}Ti_{0.66}H_x$ with the line EDX scan, where the yellow and blue line represents the concentration in at.%. of U, and Ti, respectively.

The lattice parameter of UTi_2H_x in (III) $U_{0.34}Ti_{0.66}H_x$ equals to 8.503 Å. Hence it seems likely that UTi_2H_x can have a certain stability range, with the H concentration being variable. Due to the presence of the additional phases, we can not determine the precise amount of absorbed H_2 gas. We can use information from the neutron diffraction studies of the $UTi_2D_{5.7}$ yielding $a = 8.48$ Å [187], which is close to the value observed for the (III) hydride, therefore we assume that for this hydride $x \approx 5$. The values of lattice parameters suggest that UTi_2H_x in the (I) and (II) samples may contain even more hydrogen. It is quite a realistic scenario taking into account that $ThZr_2H_x$ with the $MgCu_2$ type of structure forms in the range of $1.8<x<6.7$ [143]. The other option would be antistructure Ti atoms in the U positions, compensating α-U as the impurity phase in (III). On the other hand, one has to realize that α-U can also accommodate a few percent of Ti, as given by the phase diagram, which reduces the necessity for compensation.

7.3.2. Magnetic properties of the UTi_2 hydrides

The temperature dependence of magnetization of individual hydrides reflects the fact that none of the materials obtained was entirely single phase, but one can deduce the intrinsic properties of UTi_2H_x and their alterations. Temperature dependencies of magnetization $M(T)$ indicate that the samples exhibit two ferromagnetic phase transitions (see Fig. 7.34 (a)). The one which appears around 175 K is undoubtedly related to the UH_3-type of material, which exhibits only a small shift of ordering temperature due to Ti incorporated in the hydride. The other feature is the second transition around 54 K. It is easier to recognize the transition in the case of (I) and (II) $U_{0.34}Ti_{0.66}H_x$. We can associate this transition with the UTi_2H_x phase, as it becomes most pronounced in the sample (I), where the Laves phase dominates in XRD patterns. One can even notice that the hydride with the broader transition (II) exhibits more broadening of the corresponding XRD peaks, which can reflect the distribution of the lattice parameter (microstrain).

The appearance of ferromagnetism for these hydrides is not surprising, the shortest U-U distances of 3.72 Å are on the magnetic side of the Hill plot. On the other hand, such clear ferromagnetism is absent in $U_{0.34}Ti_{0.66}H_x$ (III). Its shortest U-U distance also lies in the range where Hill predicted a magnetic ground state ($d_{U\text{-}U}$ = 3.68 Å nevertheless, it is paramagnet with the Curie-Weiss behavior. A reason for such behavior can be seen perhaps in the character of Ti as element, exhibiting similar electronegativity as U (respectively 1.5 and 1.4 [188]). The Ti-3*d* states having a large energy overlap with the U-5*f* band, contributing by the 3*d*-5*f* hybridization to the 5*f*-magnetism suppression. We cannot also exclude antistructure atoms of Ti in the U sublattice, as the atomic radii of U and Ti are closer than in the case of Laves phases with late 3d metals, such as Fe, Co, Ni. On the other hand, hydrogen can moderate the ground state, as well, namely by a charge transfer. Strong ferromagnetism of β-UH_3 can also be considered as an example of such a case [186]. Further in this work the ferromagnetic hydride in (I) and (II) samples is referred to as UTi_2H_6, for nonmagnetic hydride in (III) we use the following formula UTi_2H_5.

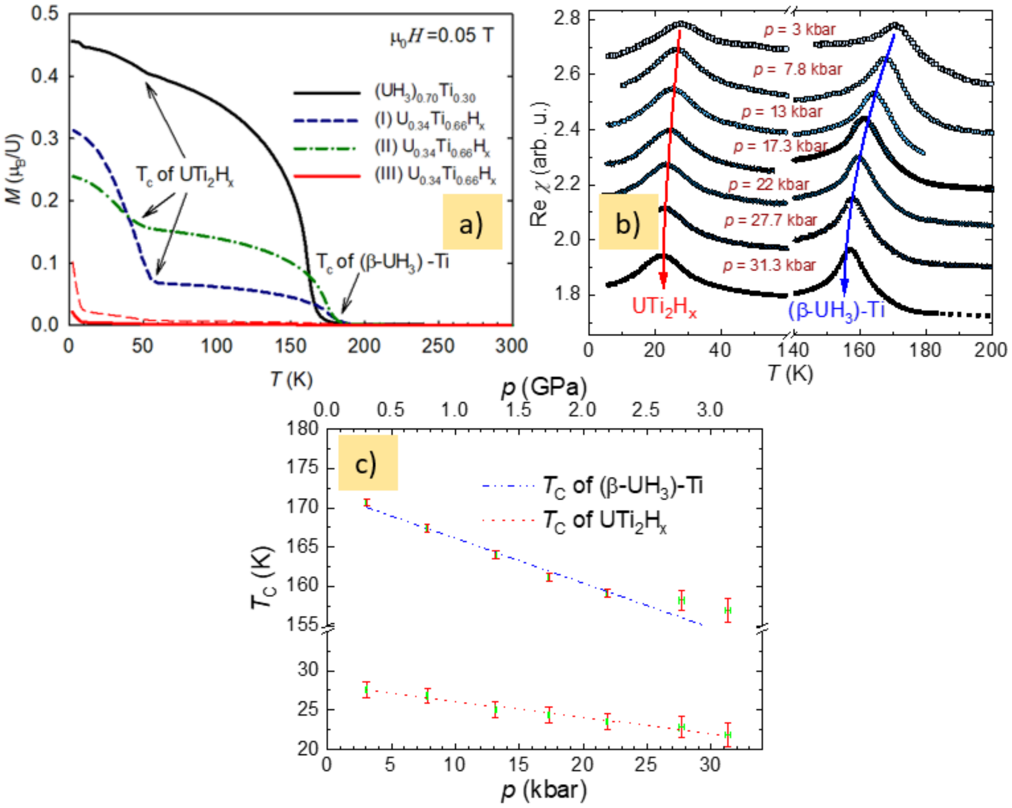

Fig. 7.34 (a) Temperature dependence of the magnetization in magnetic field μ_0H = 0.05 T for the hydrides synthesized at T = 973 K. The dashed red line corresponds to the magnetization of the (III) $U_{0.34}Ti_{0.66}H_x$ multiplied for clarity by the factor of 5. (b)

Details of the pressure variations of the real part of *ac* susceptibility, $\chi_{ac}(T)$, for (II) $U_{0.34}Ti_{0.66}H_{x=6}$. For clarity, some of the data were vertically shifted. The red and blue arrows indicate the change of T_C for (β-UH_3)-Ti and UTi_2H_x The maximum pressure change at the lowest temperature was $\Delta p \approx 0.3$ GPa (for $p < 2.5$ GPa) and $\Delta p \approx 0.5$ GPa (for $p > 2.5$ GPa). (c) Pressure variation of T_C of (β-UH_3)-Ti and UTi_2H_6. The dotted lines represent the linear fits.

On the other hand, the higher inter Uraniums distance $d_{U\text{-}U}$ and the effect of hydrogen presence could be the reasons of the enhanced magnetism of UTi_2H_6. The effect of the change of the $d_{U\text{-}U}$ was inspected via the studies of *ac* magnetic susceptibility $\chi_{ac}(T)$ under hydrostatic pressure. It is a good technique for the detection of the small changes of T_C. In the real part of *ac* susceptibility $\chi_{ac}(T)$ ferromagnetic transitions lead to the development of the district peaks below 175 K and 30 K, which shift to lower temperature with the increase of pressure (see Fig. 7.34 (b)). The peaks develop as result of the interplay of magnetization increase with decreasing T and freezing the moments due to magnetic anisotropy. For low driving *ac* fields magnetization becomes “frozen” few Kelvins below T_C, when the width of hysteresis curve exceeds the amplitude of the driving magnetic field [156]. Therefore the positions of the peaks do not really correspond to T_C, which is a few degrees higher, close to the inflection point on the high-temperature slope of the peaks. For analysis of the change of the transition temperature we have used the sharp maxima of the peaks due to the fact that it gives better relative precision for the T_C determination. At maximum pressure of 3.1 ± 0.5 GPa the transition temperature of UTi_2H_6 reduces down to 21.8 K, linear fit provides pressure derivative of UTi_2H_6 equal $dT_C/dp = -0.020 \pm 0.001$ K/GPa (see Fig. 7.34 (c)). The logarithmic derivative $1/T^*dT_C/dp \approx -0.00092$ GPa^{-1} which has a more physical meaning, in absolute value it is almost by a factor of 3 lower than another Laves compound with $T_C \approx 160$ K, UFe_2 [189]. For (β-UH_3)-Ti the values are $dT_C/dp = -0.057 \pm 0.004$ K/GPa and $1/T^*dT_C/dp \approx -0.00036$ GPa^{-1}. It worth indicating that (β-UH_3)-Ti exhibits values quite different from the ones which were found in our recent study of $(UH_3)_{0.82}Mo_{0.18}$ with $1/T^*dT_C/dp \approx 0.000114$ GPa^{-1} [156]. The reason can be, besides an intrinsic resistance of magnetic moments and their interactions to the volume compression, also in variations in volume compressibility (bulk modulus), which are not known.

In the studied range, the ferromagnetic transition UTi_2H_6 was not suppressed even in the highest pressure, which makes not magnetic UTi_2H_5 event more interesting, therefore its properties were studied in more details. This was facilitated by the fact that the hydride could be obtained in large monolithic pieces.

Magnetic susceptibility, $\chi(T)$, measured in several magnetic fields exhibits generally increasing value with decreasing temperature, but one can notice several anomalies (see Fig. 7.35), particularly observable in low magnetic fields. We can associate them with a small amount of ferromagnetic impurities, present on the level < 1%. In particular, the phases UTi_2H_6 (with T_C = 54 K) and (UH_3)-Ti (with T_C = 175 K) (see inset of Fig. 7.35) could be identified. The estimate is based on the assumption of 1 μ_B/U moments. Measurements in low magnetic fields (0.05 T) do not show full spontaneous magnetization, but definitely its major part if performed in the field-cooled mode, which is the case here.

The presence of ferromagnetic impurities makes analysis of paramagnetic susceptibility of UTi_2H_5 somewhat tricky. A standard impurity elimination procedure, based on the assumption of field-independent impurity magnetization, is not applicable, because weak itinerant ferromagnetic U hydrides exhibit a significant field dependence of magnetization in the ordered state. Therefore we used, so as to estimate the parameters of the Curie-Weiss susceptibility, the $\chi(T)$ data only for $T > 200$ K. Fig. 7.36 (a) shows that $1/\chi(T)$ in this range can be indeed approximated by a straight line, from which the effective magnetic moment μ_{eff} = 3.1 μ_B/U and paramagnetic Curie temperature of Θ_p = -200 K can be deduced.

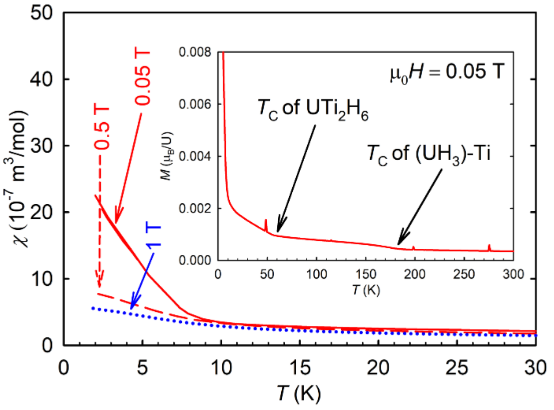

Fig. 7.35 Temperature dependence of the magnetic susceptibility of UTi_2H_5, measured in μ_0H = 0.05, 0.5, and 1 T in the field-cooled mode. The inset presents the

magnetization over an extended temperature range for $\mu_0 H = 0.05$ T, exhibiting anomalies due to the presence of spurious phases, identified as UTi_2H_6 and (UH_3)-Ti.

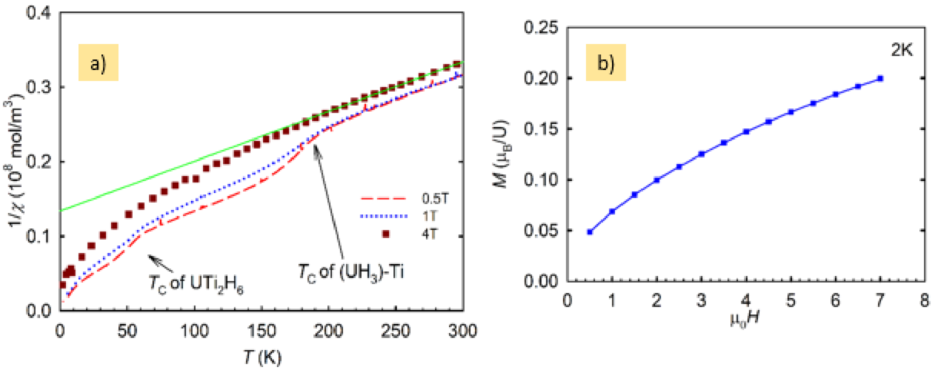

Fig. 7.36 (a) The inverse magnetic susceptibility $1/\chi$ measured in the magnetic fields of 0.5, 1, and 4 T. The green line represents the Curie-Weiss fit mentioned in the text. (b) The temperature dependence of magnetization of UTi_2H_5 at $T = 2$ K.

At low temperatures, where the contribution of ferromagnetic impurities saturates, $\chi(T)$ sets to a dramatic increase, which could be so far followed down to $T = 2$ K. The increase is, however, gradually suppressed in magnetic fields on the scale of several Tesla, which implies a non-linear, saturating magnetization as a function of field. That was indeed observed experimentally on isothermal magnetization measurement (see Fig. 7.36 (b)). An estimate of magnetization originating from the two ferromagnetic impurities represents only ≈ 0.01 μ_B/U, that is why the majority of the magnetization observed can be assumed intrinsic.

7.3.3. Thermodynamic properties of UTi_2H_5

The non-magnetic ground state of UTi_2H_5 can find its explanation from the studies of the thermodynamic, electron and heat transport properties. The temperature dependence of specific heat at constant pressure $C_p(T)$ is shown on Fig. 7.37. One can notice a tendency to saturation in the range 100-180 K, where the asymptotic value could be estimated as 80 J/mol K. This value corresponds to the classical limit of specific heat 3*R/mol atom K, considering 3 atoms in formula unit (i.e. without the H atoms), and an additional electronic specific heat $\gamma * T$, with the γ-value, 256 mJ/mol K^2, deduced below. In this part the data approximately follow the Debye model with the Debye temperature $\Theta_D = 250$-300 K.

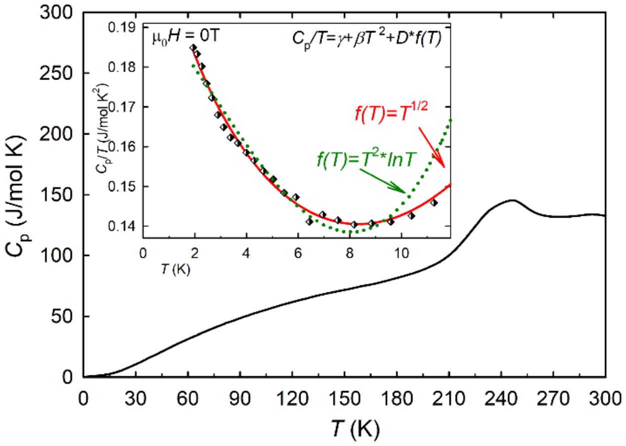

Fig. 7.37 Temperature dependence of specific heat C_p of UTi_2H_5 in the temperature range 2 – 300 K. The inset shows a detail of specific heat in the $C_p/T\,(T)$ representation. The diamonds represent the experimental points, while the dotted and solid lines correspond respectively to non-interacting and weakly interacting spin fluctuations.

Optical phonon modes related to H vibrations, described as Einstein modes, are typically contributing only at much higher temperatures. However, we cannot observe how the additional specific heat of optical modes sets gradually in. The reason is the pronounced anomaly around 240 K, observable also in electrical resistivity and thermopower (see below), which is tentatively attributed to a lattice effect, classified as melting of the hydrogen sublattice. This effect, observed also in transport properties, will be discussed later.

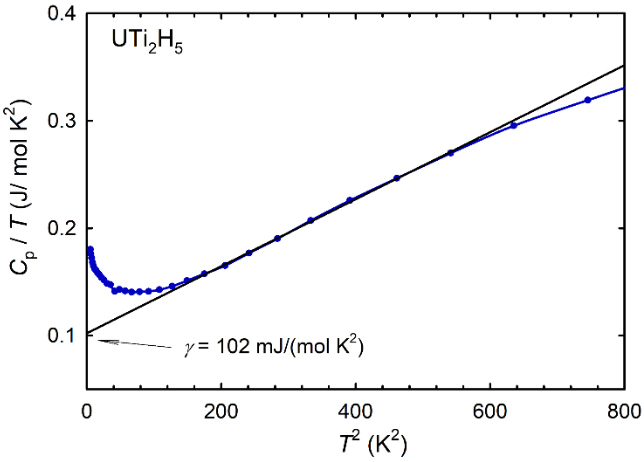

Fig. 7.38 Temperature dependence of specific heat in the $C_p/T\,(T^2)$ representation. The straight line indicates the fit used to estimate the high-temperature γ-value and Θ_D.

Very interesting is the behavior at low temperatures, seen in the C_p/T versus T representation in the inset of Fig. 7.37 and for the $C_p/T(T^2)$ plot in Fig. 7.38. The dominant effect is the pronounced upturn, which develops below 10 K. In regular metals $C_p(T)$ can be described as $C_p = \gamma T + \beta T^3$ and is therefore monotonously decreasing with decreasing T. Deviations can be ascribed to different mechanisms. In a situation close to the onset of magnetic order, such upturn means a substantial magnetic entropy concentrated to low temperatures. In case of static disordered moments, the upturn is a sensitive function of magnetic field: it is typically suppressed by fields not exceeding than 1 T. However, such upturn can be also related to the dynamics of moments, i.e., spin fluctuations. We have used two different additional terms, which can describe the contribution of spin fluctuations to a simple metallic specific heat. The first contribution to C_p/T, which has the form $f(T)=T^2\ln T$, is known as the contribution of non-interacting spin fluctuations (dotted line in the inset of the Fig. 7.37) [81]. It approximately describes the data below 6 K, nevertheless better fit was obtained when the term $AT^{1/2}$ with negative A-value predicted for weakly interacting spin fluctuations was used ($f(T)=T^{1/2}$ – solid line in the inset of the Fig. 7.37) [81]. The data were also estimated using the terms which can describe spin glass and high-temperature Schottky anomaly, but the fits (not shown here) were incompatible with experimental data. Fig. 7.38 shows that the γ-value from temperatures above the upturn is reduced to 102 mJ/mol K^2. The coefficient β = $3.119 \cdot 10^{-4}$ J/mol K^4 obtained from the linear part gives another estimate of Θ_D = 265 K.

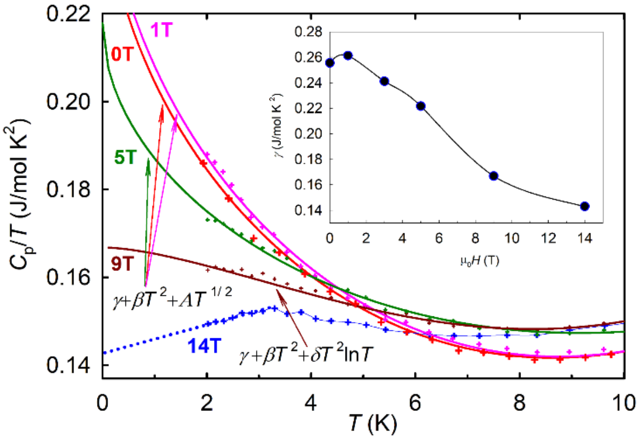

Fig. 7.39 C_p/T versus T for UTi_2H_5 in various applied magnetic fields. The solid lines for 0, 1, 5 T represent the fit using the weakly interacting spin-fluctuation model, the 9 T data were fitted using the non-interacting spin-fluctuation model. The field dependence of the γ-value is presented on the inset.

The γ-value obtained from the fit using weakly interacting spin fluctuation model is $\gamma = 256$ mJ/mol K^2, i.e. substantially higher than that of another Laves phase and archetypal spin-fluctuation materials UAl_2 ($\gamma = 142$ mJ/mol K^2) [50], and classifies the compound as a mid-weight heavy fermion. The spin-fluctuation contribution to specific heat should be affected by applied magnetic field, but the fields are much higher in this case than for the static disorder.

Table 8 Parameters obtained from the low-temperature C_p/T (T) data analysis for UTi_2H_5 in various applied magnetic fields. For details see the text.

$\mu_0 H$ (T)	γ mJ/ mol K^2	β mJ/ mol K^4	A mJ/ mol K$^{5/2}$	δ mJ/ mol K^4
0	256	0.00051	-0.0517	-
1	261	0.00052	-0.0538	-
5	218	0.00028	-0.0311	-
9	169	-0.00142	-	0.000545
14	-	-	-	-

The effect of magnetic field up to 14 T on specific heat is shown in Fig. 7.39. As a function of field one observes a weak but noticeable increase (inset of the Fig. 7.39), projected to the increase of extrapolated γ-value to 261 mJ/mol K^2. Proceeding to higher magnetic fields it becomes evident that the C_p/T values at very low temperatures are suppressed relatively more than at the beginning of the upturn, which amounts to formation of a broad maximum in $\mu_0 H = 14$ T, where the standard data analysis is not possible, γ-value was determined from the linear part which is manifested below $T = 3.3$ K. The data for $\mu_0 H = 9$ T has still C_p/T monotonously increasing with decreasing T below 8 K. However the gradual suppression by magnetic field starts to be visible. Hence the dependence $\gamma + \beta T^2 - AT^{1/2}$ cannot be used. The saturation at low temperatures is better captured by the dependence $\gamma + \beta T^2 + \delta T^2 \ln T$, which was used to obtain the γ estimate in Table 8.

7.3.3.1. Investigation of the “Ti-rich” Laves phase

In the context of the Laves phase UTi_2 stabilized by hydrogen it is interesting to explore what happens in case of Ti excess, which may lead either to antistructure atoms of Ti in the U positions or to segregation of Ti hydride, if we consider the two most plausible cases. Therefore we attempted to use the U to Ti ratio of 1:4 for hydrogenation. The technology of the hydrogenation is described in section 6.1.3.2., while the structure of the precursor bulk alloy $U_{0.20}Ti_{0.80}$ was discussed in section 7.1.2. Diffraction pattern indicates that the hydride also exhibits the cubic Laves structure with $d_{U\text{-}U} \approx 3.69$ Å (see Fig. 7.40 (a)), it is 0.01 Å larger than for UTi_2H_5. The Laves hydride is the main discovered phase, but there is also an impurity phase TiH_2 (sp. gr. *Fm-3m*). The refined crystaline size of the impurity phase equals ≈ 140 Å, which could explain the fact that TiH_2 was not recognized by the electron microscopy study. The analyses also did not show any segregation of Ti. The investigation by means of EDX show that the main phase contains ≈ 80 at.% of Ti, there are also fragments with Ti concentration of 75 at.%. It allows to assume that Ti atoms, to some extent, occupy U positions in the Laves structure. It is interesting that lattice parameter with respect to UTi_2H_5 is almost not affected by the Ti antistructure. It can highlight the role of hydrogen in the stabilization of the Laves hydride. Further in the text we call it UTi_4H_5.

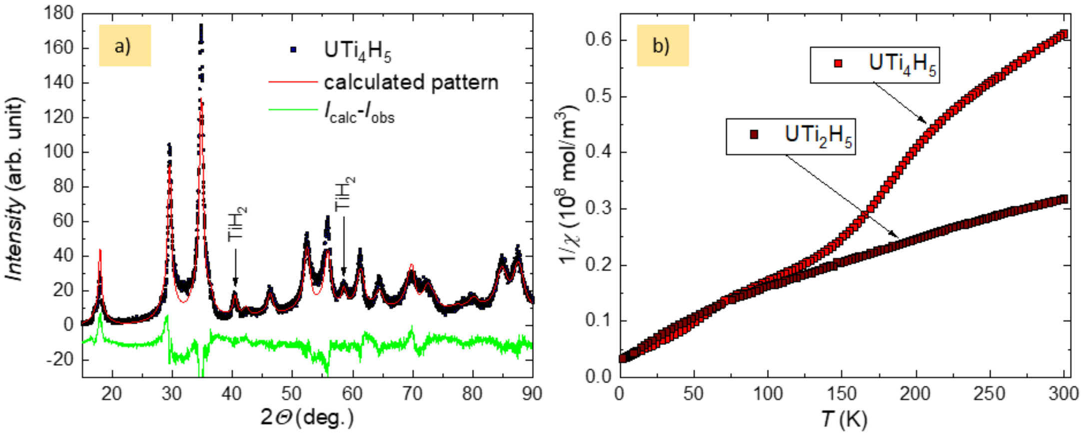

Fig. 7.40 (a) Results of the refinement of the crystal structure of UTi_4H_5 hydride. (b) Comparison of the magnetic susceptibility of UTi_4H_5 and UTi_2H_5 measured in magnetic field of 4T.

The inverse magnetic susceptibility of UTi_4H_5 is shown on Fig. 7.40 (b). It also exhibits nonmagnetic ground state with slight ferromagnetic impurity with $T_C \approx 50$ K and $T_C \approx 200$ K. The impurities are related to (UH_3)-Ti and UTi_2H_6 phases. In contrast to the magnetic susceptibility of UTi_2H_5, UTi_4H_5 exhibits a contribution of the high-temperature ferromagnetic impurity (UH_3)-Ti even in the magnetic field of 4 T. Therefore only inverse magnetic susceptibilities $1/\chi(T)$ measured above 250 K were evaluated. Effective magnetic moment $\mu_{eff} \approx 4\ \mu_B$/U looks overestimated due to the influence of impurity, on the other hand, paramagnetic Curie temperature of Θ_p = -48 K is considerably higher than the value observed for UTi_2H_5 (≈ 200 K).

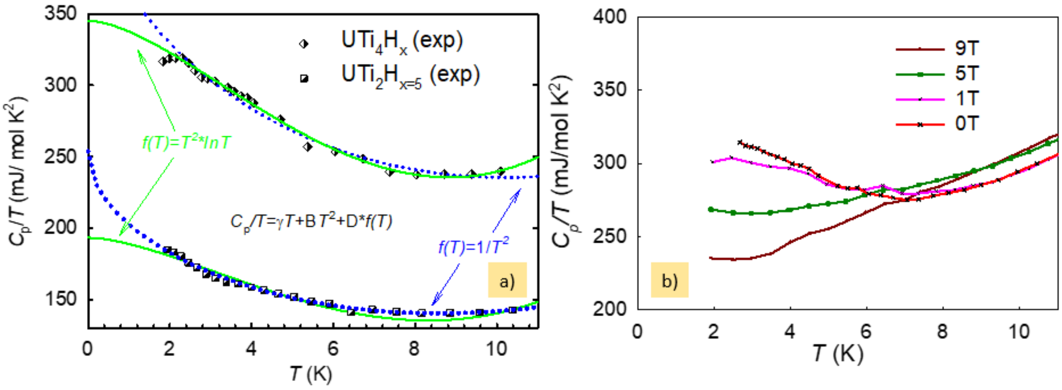

Fig. 7.41 (a) C_p/T versus T of UTi_2H_5 and UTi_4H_x fitted with non-interacting spin fluctuations $f(T)=T^2\ln T$ and weakly interacting spin fluctuations term $AT^{1/2}$ which could contribute to specific heat of a regular metal. (b) Field change of C_p/T versus T for UTi_4H_x.

This hydride also exhibits low-temperature anomaly in specific heat (see Fig. 7.41 (a)). In contrast to UTi_2H_5 C_p/T vs. T representation of C_p is better described by the contribution of the term which accounts for non-interacting spin fluctuations (i.e. $\delta T^2\ln T$). It allowed defining the Sommerfeld coefficient γ=345 mJ/mol K^2. The other striking difference is the modification of the field dependencies of the anomaly shape, magnetic field μ_0H = 9 T is sufficient to get the anomaly nearly suppressed (see Fig. 7.41 (b)). This data suggest that the increase of the Ti concentration leads to a decoupling of the spin fluctuations.

7.3.4. Transport properties of UTi_2H_5

The bulk shape of UTi_2H_5 allowed studying its transport properties. Temperature dependence of electrical resistivity $\rho(T)$ was measured in the range of 0.4 – 300 K (see Fig. 7.42). The technology of the measurements is described in section 6.3.3. The overall dependence is metallic, with a monotonous increase with increasing T, and it is rather flat. The high residual resistivity ρ = 280-290 μΩcm can be associated with certain disorder in the occupation of H sublattice. A dominant feature of $\rho(T)$ is the knee at ≈ 60 K, which often appears at materials (including U-based) classified as spin fluctuators. As an archetype we can again take the spin fluctuator UAl_2 [92]. A unique feature of UTi_2H_5 is the step at 240-260 K, which could be perhaps associated with the further increase of the disorder of the H sublattice (melting), which was indicated e.g. in some $REMn_2$ hydrides also having the cubic Laves phase structure ($a \approx 800$ pm) [190]. This effect is present both at heating and cooling and exhibits no hysteresis. It is accompanied by the pronounced anomalies in specific heat, Seebeck coefficient, etc., centred around $T = 240$ K. Such effect should also manifest in lattice properties. Therefore we studied variations of the crystal structure below room temperature.

Fig. 7.43 reveals that there is indeed a lattice effect, a temperature-induced expansion, taking place between approximately 220 and 260 K. The expansion in a is 15 pm, which amounts to the volume expansion $\Delta V/V_0 = 3*\Delta a/a_0 = 0.005$. The linear part of $a(T)$ below the transition allows to determine the coefficient of thermal expansion $\alpha_V = 3*\alpha = 3/a*\Delta a/\Delta T = 2.4*10^{-5}$ K^{-1}.

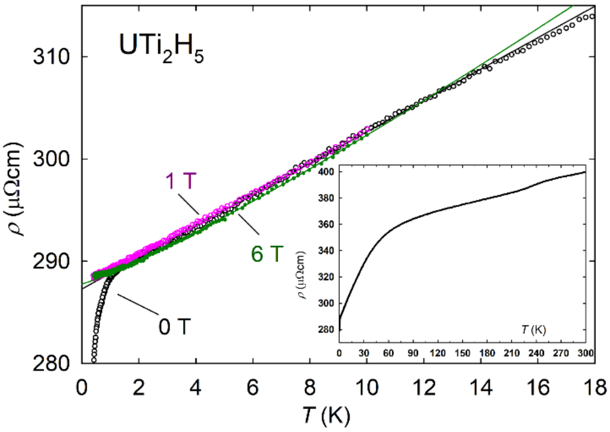

Fig. 7.42 Temperature dependence of electrical resistivity, $\rho(T)$, in the fields of 0, 1 and 6 T. The full lines show the fits mentioned in the text. The inset shows the zero-field data measured from 0.4 to 300 K.

Materials close to the verge of magnetic order exhibit specific character of low temperature resistivity, at which the progressing renormalization of Fermi liquid coefficient a in the aT^2 term, representing the e-e scattering, leads to a shrinkage of the Fermi liquid region. Then a different resistivity scaling (non-Fermi liquid) bT^α appears over a more extended temperature range at the quantum critical point, at which a long-range order appears at $T = 0$ K. The exponent α is reduced to 5/3 for 3D ferromagnetic quantum critical point, but can be further reduced by reduction of dimensionality or in an antiferromagnet [81]. However, the effect of magnetic fluctuations is well observable only for low residual resistivity. It is not the case here, the residual resistance ratio, $\rho_{300\mathrm{K}}/\rho_{4.2\ \mathrm{K}} = 1.4$, is unfavorable for a clear observation of the impact of *e-e* scattering on resistivity. $\rho(T)$ is monotonously decreasing from T = 50 K to 1.5 K in an approximately linear way. A detailed quantitative analysis revealed that the linearity is very well followed in a broad temperature range 1.5-15 K, where the fitting gave $\alpha \approx 0.99$. The linear behavior in this case cannot reflect anything like reduced dimensionality. We conjecture that this behavior is reflecting the interplay of inhomogeneity and magnetic correlations. Indeed, such a situation can give α as low as 1 if modeled by the impact of static and dynamic disorder in the Anderson-Hubbard model [191]. Below $T \approx 1.5$ K, $\rho(T)$ tends to turn down. This downturn is considerably reduced in $\mu_0 H = 0.1$ T and it is absent in 1 T. We assume that this effect is due to superconductivity of the spurious α-U phase, which has a low upper critical field H_{c2} [6]. Hence $\rho(T)$ remains linear down to the lowest temperatures, and parameters of the fit remain practically the same as for zero-field data. The situation changes somewhat in higher magnetic fields. Although the residual resistivity remains practically the same, the coefficient α is enhanced to 1.15 in $\mu_0 H = 6$ T, which reflects the curvature of the data shown in Fig. 7.42.

The impact of disorder is naturally seen also in thermal conductivity. Its value $\kappa = 4.25$ W/K m is low and is reached only at room temperature (see Fig. 7.44). The conventional maximum in $\kappa\ (T)$ occurring at low temperatures, where the thermal scattering effect is reduced [192], is absent in UTi_2H_5. Assuming the validity of the Wiedemann-Franz law, we attempted to decompose the total experimental thermal conductivity into the electronic $\kappa_{\mathrm{el}}(T)$ and lattice $k_{\mathrm{ph}} = \kappa(T) - \kappa_{\mathrm{el}}(T)$ contributions.

We assume that $\kappa_{\mathrm{el}}(T) = L_0 T/\rho(T)$, where $L_0 = \pi^2 k_B^2/3|e| = 2.45{*}10^{-8}\ \mathrm{W\Omega/K^2}$, $\rho(T)$ is the experimental electrical resistivity. The result, which is also included in Fig. 7.44, indicates that the total thermal conductivity is dominated by the phonon conductivity. In good metallic conductors, κ_{el} is considerably higher than κ_{ph}, because the Fermi velocity v_F of conduction electrons is much higher than the sound velocity v_s of phonons [193]. In our system both electrons and phonons should be affected by the disorder in a similar way. The fact that κ_{el} still remains smaller can indicate a low concentration of conduction electrons, which is more apparent in binary U hydrides UH_3, explained by a depopulation of electronic states with low effective mass (U-6*d*, 7*s*) [45]. The dominance of κ_{ph} is illustrated by the experimental Lorentz factor $L(T)/L_0 = \kappa(T)/\rho(T)$, which should be equal to 1 due to the Wiedemann-Franz law in the case of electronic transport only.

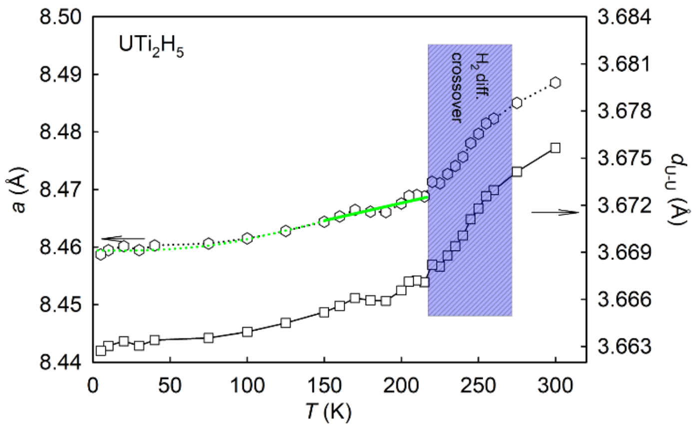

Fig. 7.43 Temperature dependence of the lattice parameter *a* and of the minimum U-U distance obtained from refinement of XRD patterns. The green line demonstrates the determination of the linear thermal expansion coefficient α.

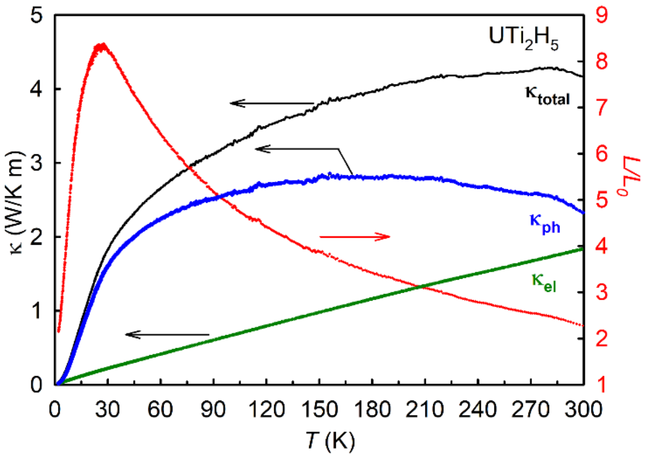

Fig. 7.44 Temperature dependence of thermal conductivity of UTi_2H_5 (black). The tentative decomposition into components shows the phonon (blue) and electron (green) conductivity. The temperature dependence of the relative Lorentz number is marked red.

The temperature dependence of thermoelectric power (Seebeck coefficient), *S*(*T*), is generally less straightforward to interpret. It should reflect both the energy derivative of the Fermi surface and the scattering probability, and should be linear in

T at high temperatures, where the type of scattering does not change with changing temperature and is essentially elastic. This is expressed by the Mott equation:

$$S = \frac{\pi^2}{3\mathrm{e}} \mathrm{k}_\mathrm{B}^2 T \left\{ \frac{\partial \ln \sigma(E)}{\partial E} \right\}_{\mathrm{E}=\mathrm{E}_\mathrm{F}}$$

S(*T*) of UTi_2H_5 (see Fig. 7.45) exhibits at high temperatures the anomaly attributed to the diffusion of H atoms, which was also seen in electrical resistivity and specific heat. Surprisingly, no visible anomaly was identified in thermal conductivity, which was determined in the same experimental run as the thermopower. The linearity of *S*(*T*) in the temperature range below the anomaly and probably also above is evident. The dominant feature at low temperatures is a minimum at ≈ 35 K, below which *S*(*T*) again increases to positive values. The *S*(*T*) should reach 0 in the $T \rightarrow 0$ limit, therefore we can expect that the dependence still turns down at the lowest temperatures. Indeed, few experimental points near the lowest limit may suggest that *S*(*T*) is turning down with decreasing *T* below 3.5 K. The absolute values vary only between -1 and +4 mV/K, not reaching values common in narrow-band materials. One of the reasons can be the disorder, possibly smearing out the density of states and the energy dependence of relaxation rate around the Fermi level.

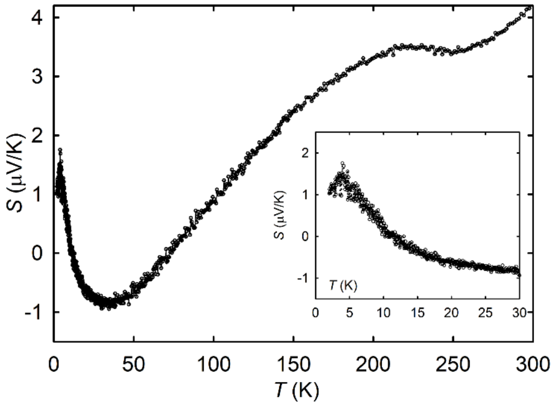

Fig. 7.45 Temperature dependence of thermopower, *S*(*T*), of UTi_2H_5. The inset shows the low-*T* detail.

Considering that UTi_2H_5 is in the proximity of the onset of magnetic ordering, we should seek an interpretation of the features observed in the context of known spin fluctuators. One can compare the data e.g., with spin fluctuator YCo_2, which exhibits a broad maximum in *S*(*T*) at 200 K [194], i.e., at the temperature where a knee in *ρ*(*T*) appears, which can be associated with electron scattering on spin fluctuations. Among U-based spin fluctuators, such a minimum was observed e.g. in UAl_2. Although in special cases such minima can be due to specific electronic structure, the universal occurrence at spin fluctuators suggests that they can be explained by a paramagnon drag, i.e., effect which is not the usual electron diffusion induced by a different Fermi-Dirac broadening at different temperatures. Such an effect was actually considered for UAl_2 in Ref. [31].

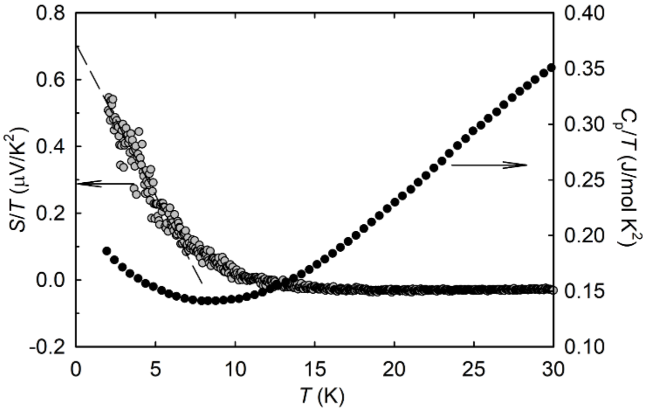

Fig. 7.46 Temperature dependence of thermopower in the S/T vs. T representation compared with specific heat data $C_p/T(T)$ on the same temperature scale.

It is interesting to remove the explicit dependence on T in the Mott equation by plotting S/T (see Fig. 7.46). The comparison with C/T, exhibiting the spin-fluctuation enhancement, reveals that both quantities are affected by spin fluctuations in a similar way. One can compare the ratio using the dimensionless number

$$q = \frac{S}{T}\frac{\mathrm{N_A}|\mathrm{e}|}{\gamma},$$

where the product of the electron charge e and N_A is the so-called Faraday number ($9.65*10^4$ C/mol). Assuming a simple Fermi gas or liquid model, $q = 1$ should be expected [195]. Using the values extrapolated to 0 K, $S/T = 7*10^{-7}$ V/K^2 and $\gamma = 0.256$ J/mol K^2, we obtain $q = 0.21$, i.e. the right order of magnitude. However, the possible existence of a magnetic phase transition below 2 K, which would lead to a maximum in $S(T)$, could still change the S/T value dramatically. Thermopower measurements to millikelvin temperatures would be necessary to resolve this issue.

There is extended experimental evidence that UTi_2H_5 is a spin fluctuator poised at the verge of magnetic ordering. Several phenomena can be taken responsible for this situation. First, the U-U spacing of 367.5 pm, exceeding the Hill limit 340-360 pm [36], is sufficient for stabilization of U magnetic moments and their ordering. Magnetic properties of U compounds are also supported by the incorporation of hydrogen. In addition to the volume expansion effect increasing $d_{U\text{-}U}$ it is also the effect of H bonding, which depopulates the U-6*d* states and reduces the 5*f*-6*d* hybridization, which is in favour of strong magnetism [45]. An opposite effect can be expected from the 5*f* hybridization with T-3*d* states, which can be rather strong. In UT_2 Laves phases with 3*d* metals, magnetic order appears at the end of the 3*d* series [36], as there is only very little energy overlap of e.g. Ni-3*d* states with the 5*f* states, which remain pinned at the Fermi level and are therefore located at much higher energies. Another island of magnetism appears around UFe_2, which is driven mainly by the Fe-3*d* states, but proceeding to the left in the 3*d* series the magnetism is lost, presumably due to shifting the 3*d* states up in energy and supporting thus the 5*f*-3*d* hybridization. For example, UMn_2 is a weak Pauli paramagnet [36]. In this context we can deduce that preventing the UTi_2 hydride with such large $d_{\text{U-U}}$ from magnetic ground state is the hybridization with the Ti-3*d* states.

From all the U-based Laves phases, the bulk properties of UT_2H_5 are most similar to UAl_2. For this compound, the lattice parameter a = 7.766 Å [196] implying $d_{\text{U-U}}$ = 3.36 Å, barely below the Hill limit. This compound follows the Curie-Weiss law at high temperatures, described by $\mu_{\text{eff}} = 3.1\ \mu_B$/U. Large negative Θ_p = -245 K is more due to single-ion moment instability than related to antiferromagnetic interactions. $\chi(T)$ becomes flat at intermediate temperatures (50-100 K) and a pronounced upturn appears at the low-temperature side [34]. In comparison, UTi_2H_5 behaves similarly, only the characteristic energies of spin fluctuations are lower. E.g. the Θ_p value is less negative (-200 K), the low-T upturn more pronounced. Stronger effect of electron-electron correlations can be seen in much higher Sommerfeld coefficient γ = 256 mJ/mol K^2, approximately doubled comparing to UAl_2 with 142 mJ/mol K^2, which has a similar, but less pronounced, low temperature upturn in C_p/T [50].

From other U compounds, one can find UTi_2H_5 analogous to e.g. U_2Co_2Sn. Similar to U Laves phases, also the U_2T_2X compounds (X is a *p*-metal) exhibit magnetic order for the late transition metals T [197]. Proceeding to less filled *d*-band, the 5*f*-*d* hybridization becomes stronger and the order is lost. U_2Co_2Sn is located close to the onset of magnetism on the non-magnetic side. Its properties studied down to the millikelvin range [198] are characterized by the upturn in $C_p/T\ (T)$ following the $-AT^{1/2}$ law. γ reaching 340 mJ/mol K^2 (1 mole contains 2 U atoms) is gradually suppressed by magnetic fields, followed to 13 T. Low-temperature $\rho(T)$ exhibits a non-Fermi liquid behavior with exponent reduced from $\alpha = 2$ to ≈ 1.8. We showed above that the disorder in UTi_2H_5 prevents from observing the dynamics of magnetic moments in electrical resistivity. The disorder instead projects into a specific interesting NFL behavior with exponent $\alpha = 1$.

Ref. [198] also attempts to analyze the analytical form of $\chi(T)$ upturn at low temperatures. The power law is different than the $1\text{-}AT^2$ found in UAl_2 [81]. But even the latter finding was disputed, a linear dependence was identified for UAl_2 by other authors [199]. Evidently, the susceptibility in low fields must be sensitive to defects like antistructure atoms, having possibly stable magnetic moments. High magnetic fields, on the other hand, suppress intrinsic spin-fluctuation features. Therefore we did not attempt to describe the low-T susceptibility analytically. The characteristic energy of spin fluctuations, T_{SF}, was estimated for UAl_2 from the quadratic coefficient of electrical resistivity at 25-30 K [200]. The disorder prevents us to perform similar analysis. We may, however simply assume that γ higher by a factor of 2 (meaning twice higher effective mass of electrons) can be roughly corresponding to twice lower T_{SF}, being thus in the range 10-15 K. Indeed, we see that the upturn in C/T starts to develop below this temperature. Similarly, the enhancement of S/T below such temperatures indicates that the estimate is consistent.

So far we can therefore classify UTi_2H_5 as a nearly magnetic spin fluctuator. However, we cannot rule out the possibility of magnetic order below $T = 2$ K, which can also affect the susceptibility observed. So far, only experiments down to the millikelvin range were performed when studying electrical resistivity, which is, however, affected by the spurious superconducting α-U phase.

In the present study we did not investigate details of H positions in $UTiH_5$. For this type of study the neutron diffraction experiment of analogous deuteride is necessary. We can rely on previous data in ref. [187], indicating a fractional (< 0.4) occupancy of two different types of tetrahedral D positions, 96*g* (U_2Ti_2) and 32*e* (UTi_3), while the third possible position 8*b* has the occupancy close to zero. The related atomic disorder should affect mainly the properties depending on long-range coherence of wave functions, i.e. the transport properties, which is indeed the case. The study [187] also explained the formation of the Laves phases of UTi_2H_x by helping to fulfil the geometrical condition for existance of Laves phases, namely the ratio between the atomic radii of A and B (in the general formula AB_2) elements being close to 1.225. The rather long distances U-D and Ti-D, which were found very similar to the situation in UD_3 and TiD_2, allow defining effective radii of U and Ti. Although the real atomic radii of U and Ti are too close to each other and the ration is much smaller than 1.225, such effective radii are quite higher especially for U and the ratio can be achieved. Such situation emphasizes the importance of U-H interaction in the UTi_2 hydrides.

8. Conclusions and future outlook

1. U-Ti and U-Nb alloys were successfully retained in the form of *bcc* γ-U phase. The minimum concentration of the elements required for stabilization of the phase corresponds to 25 at.% of Ti and 20 at.% of Nb. Comparison of the produced materials with the literature data indicates that ultra-fast cooling is an important component on the success, which also allows to reduce the necessary concentration of the transition element (Ti, Nb). Increase of the concentration of the transition element leads to decrease of the lattice parameter a, which is also reflected in the modification of the electronic properties. Estimated Sommerfeld coefficients indicate increase of the density of states at the Fermi level related to narrowing of 5*f*-band due to the change of the interatomic U-U spacing. Debye temperatures of the U-Ti and U-Nb splats indicate softening of the lattice, for γ-U structure the values are considerably lower from the α-U.

2. Temperature dependences of electrical resistivities indicate that U-Ti and U-Nb splats can be classified as strongly disordered alloys. The strong disorder can be considered as the reason of the negative temperature coefficient ($\frac{\mathrm{d}\rho}{\mathrm{d}T} < 0$) observed for $\mathrm{U}_{1-x}\mathrm{T}_x$ (T= Ti, Nb) splats over very wide concentration range. The materials also exhibit a dramatic change of the residual resistivity with the increase of the concentration of the alloying element. The apparent violation of the Matthiessen’s rule indicates that our alloys approach the Mott limit, reaching the minimum electron mean free path.

3. At low temperatures, the studied U-Ti and U-Nb splats are superconductors with maximum superconducting transition temperature close to 2 K. They exhibit upper critical field in the range of 6 to 8 T. It cannot be described by WHH theory of the conventional weak electron coupling. From the perspective of the response of superconductivity to the magnetic field, the studied alloys are similar to strong coupling A15 superconductors.

4. Significant enhancement of the superconducting transition temperature was achieved in the Ti-rich alloy ($\mathrm{U}_{0.20}\mathrm{Ti}_{0.80}$, T_c = 3.74 K). The height of the specific heat anomaly related with the transition is considerably higher than the value estimated according to the BCS theory which highlights the strong-coupling character of the

alloy. The obtained critical slope $-\mu_0 \mathrm{d}H_{c2}/\mathrm{d}T$ and critical field $\mu_0 H_{c2}$ support the conclusion.

5. Hydrogenation of the U-Ti and U-Nb splats produces ferromagnetic hydrides with dominant β-UH_3 phase, which exhibits a nanocrystalline structure. Crystal structure changes do not provide clear fingerprints of incorporation of transition elements, nevertheless, the modification of the Curie temperatures allows to see the effect of alloying. The transition temperature exhibits a maximum at critical concentration of Ti (Nb) of about 15%, followed by a decrease. Estimated values of magnetization per U atom M_S do not show significant deviation from original β-UH_3. Moreover, magnetization loops of the hydrides are similar to the so-called HARD materials.

6. The splat and hydride with 30 at.% of Ti exhibit significant enhancement of the Sommerfeld coefficient γ from 15.6 mJ/ mol U K^2 to 36 6 mJ/ mol U K^2. It testifies an increase of density of states at the Fermi level which is usually attributed to the increase of the U-U spacing and 5*f* band narrowing in the hydride.

7. High-temperature hydrogenation of Ti-rich alloys leads to the stabilization of UTi_2H_x with the crystal structure of the cubic Laves phase. This compound forms due to the presence of hydrogen. The number of the H atoms in the hydride can be modified by different hydrogenation procedures. Investigation of the magnetic properties indicates that UTi_2H_x can order magnetically in the case of UTi_2H_6, while UTi_2H_5 is paramagnet with the Curie-Weiss behavior. The study under the hydrostatic pressure shows that the ferromagnetism of UTi_2H_6 is not suppressed at 3.1 GPa, which suggests that hydrogen can play an important role in the formation of magnetic moments.

8. At low-temperatures UTi_2H_5 exhibits a pronounced anomaly in specific heat which can be described by weakly interacting spin fluctuation model. The defined Sommerfeld coefficients $\gamma = 256$ mJ/mol K^2 classifies the compound as a mid-weight heavy-fermion. The specific heat of the hydride is similar to another Laves phase and archetypal spin-fluctuation materials UAl_2. Investigation of UTi_4H_5 points out the possibility of U substitution by Ti. Increase of the Ti concentration leads to reduction of the interactions between spins. Specific heat data of the hydride were described by the non-interacting spin fluctuation model which gives Sommerfeld coefficient of

γ=345 mJ/mol K^2. Thermodynamic, transport and magnetic properties of UTi_2H_5 indicate that this hydride is a spin fluctuator poised at the verge of magnetic ordering.

9. An important question which requires further clarification is the role of the hydrogen concentration in the development of magnetic/non-magnetic ground state of UTi_2H_x. For this purpose neutron studies of the corresponding magnetic and non-magnetic deuterides UTi_2D_x are required. On the other hand, *ab initio* theoretical investigations of the hydrides should also shed light on the changes of the electronic structure of the Laves structure with different H occupancy as well as Ti antistructure atoms. Due to a broad stability range of the Laves hydrides, they also thoroughly studied from the perspective of energy storage, therefore improvements of the available models that describe such materials is an important challenge.

10. Further study of the U hydrides is an important subject by itself. Theoretical investigations of the U-H phase diagram indicate the richness of the system. Crystal structure predictions suggest that 14 new compounds could appear at high or very high pressures [202]. Some of the defined hydrides should exhibit a superconducting ground state. LaH_{10} is an example of a high-temperature superconductor that also appears at high pressures ($T_c > 200$ K [203]). Therefore, synthesis and study of the transport properties of the possible U-H hydrides should help to understand the development of superconductivity at that high-temperatures. Recent thin-film investigations show that UH_2 stabilizes at an appropriate temperature [204]. We have to test the temperature&pressure phase diagram and find the thermodynamical routes which lead to suggested U hydrides.

Bibliography

[1] S. V. Vonsovsky, *Magnetism*, Nauka, Moskva, 1971.

[2] S. Chikazumi, C.D. Graham, *Physics of Ferromagnetism*, 2nd ed., Oxford University Press on Demand, Oxford, 2009.

[3] C. Kittel, *Introduction to Solid State Physics*, 8th ed., Wiley, New York, 2004.

[4] W. Heisenberg, *Zur Theorie des Ferromagnetismus*, Zeitschrift Für Phys. 49 (1928) 619–636.

[5] W. Nolting, A. Ramakanth, *Atomic Magnetism*, in: Quantum Theory Magn., Springer Berlin Heidelberg, Berlin, 2009: pp. 25–84.

[6] W. Nolting, A. Ramakanth, *Quantum Theory of Magnetism*, Springer Berlin Heidelberg, Berlin, 2009.

[7] D. Vollhardt, N. Blümer, K. Held, M. Kollar, *Band-Ferromagnetism*, Springer Berlin Heidelberg, Berlin, 2001.

[8] E. Stoner, *Collective electron ferronmagnetism*, Proc. R. Soc. London. Ser. A. Math. Phys. Sci. 165 (1938) 372–414.

[9] E. Stoner, *Collective electron ferromagnetism II. Energy and specific heat*, Proc. R. Soc. London. Ser. A. Math. Phys. Sci. 169 (1939) 339–371.

[10] J. Hubbard, *Electron correlations in narrow energy bands*, Proc. R. Soc. London. Ser. A. Math. Phys. Sci. 276 (1963) 238–257.

[11] N.W. Ashcroft, N.D. Mermin, *Solid State Physics*, Cengage Learning, Boston, 1976.

[12] S. Blundell, *Magnetism in condensed matter*, Oxford University Press, Oxford, 2001.

[13] D.C. Mattis, *The Theory of Magnetism I*, Springer, Berlin, Heidelberg, 1981.

[14] D. Liberman, J.T. Waber, D.T. Cromer, *Self-Consistent-Field Dirac-Slater Wave Functions for Atoms and Ions. I. Comparison with Previous Calculations, Phys*. Rev. 137 (1965) A27–A34.

[15] S. Imoto, H. Adachi, S. Assai, No Title, in: J. Mulak, W. Suski, R. Troc (Eds.), Proc. 2nd Int. Coqf. Electron. Struct. Actinides, Wroclaw, 1977: p. 61.

[16] W.A. Harrison, *Electronic structure of f-shell metals*, Phys. Rev. B. 28 (1983) 550–559.

[17] K.T. Moore, M.A. Wall, A.J. Schwartz, B.W. Chung, D.K. Shuh, R.K.

Schulze, J.G. Tobin, *Failure of Russell-Saunders Coupling in the 5f States of Plutonium*, Phys. Rev. Lett. 90 (2003) 196404.

[18] H.H. Hill, W.N. Miner, *Plutonium and Other Actinides*, AIME. (1970) 1–19.

[19] J.R. Naegele, J. Ghijsen, L. Manes, *Localization and hybridization of 5f states in the metallic and ionic bond as investigated by photoelectron spectroscopy*, in: L. Manes (Ed.), Actinides — Chem. Phys. Prop., Springer Verlag, Berlin, Heidelberg, 1985: pp. 197–262.

[20] A.J. Freeman, D.D. Koelling, *Electronic structure and properties of the actinides*, Phys. B+C. 86–88 (1977) 16–25.

[21] A.J. Freeman, J.B. Darby, *The actinides : electronic structure and related properties*. Volume 1, Academic Press, Cambridge, 1974.

[22] B. Johansson, *Nature of the 5f electrons in the actinide series*, Phys. Rev. B. 11 (1975) 2740–2743.

[23] S.S. Hecker, M. Stan, *Properties of plutonium and its alloys for use as fast reactor fuels*, J. Nucl. Mater. 383 (2008) 112–118.

[24] A. Svane, L. Petit, Z. Szotek, W.M. Temmerman, *Self-interaction-corrected local spin density theory of 5f electron localization in actinides*, Phys. Rev. B - Condens. Matter Mater. Phys. 76 (2007) 115116. d

[25] K.T. Moore, G. van der Laan, *Nature of the 5f states in actinide metals*, Rev. Mod. Phys. 81 (2009) 235–298.

[26] N.F. Mott, *The transition to the metallic state*, Philos. Mag. 6 (1961) 287–309.

[27] A. Toropova, C.A. Marianetti, K. Haule, G. Kotliar, *One-electron physics of the actinides*, Phys. Rev. B - Condens. Matter Mater. Phys. 76 (2007) 155126.

[28] B. Johansson, O. Eriksson, M.S.S. Brooks, H.L. Skriver, *Electronic structure of actinide intermetallic compounds*, J. Less-Common Met. 133 (1987) 25–29.

[29] L. Havela, M. Paukov, M. Dopita, L. Horak, M. Cieslar, D. Drozdenko, P. Minarik, I. Turek, M. Divis, D. Legut, L. Kyvala, T. Gouder, F. Huber, A. Seibert, E. Tereshina-Chitrova, *XPS, UPS, and BIS study of pure and alloyed β-UH_3 films: Electronic structure, bonding, and magnetism*, J. Electron Spectros. Relat. Phenomena. 239 (2020) 146904.

[30] X. Dai, S.Y. Savrasov, G. Kotliar, H. Migliori, H. Ledbetter, E. Abrahams, *Calculated Phonon Spectra of Plutonium at High Temperatures*, Science. 300 (2003) 953–955.

[31] B. Coqblin, J.R. Iglesias-Sicardi, R. Jullien, *Spin fluctuations in metals: Application to the actinides*, Contemp. Phys. 19 (1978) 327–354.

[32] J.C. Lashley, A. Lawson, R.J. McQueeney, G.H. Lander, *Absence of magnetic moments in plutonium*, Phys. Rev. B - Condens. Matter Mater. Phys. 72 (2005) 054416.

[33] A.G. Volkov, A.A. Povzner, A.N. Filanovich, *The peculiarities of Americium electronic structure and magnetic susceptibility*, J. Supercond. Nov. Magn. 26 (2013) 1765–1769.

[34] M.B. Brodsky, *Magnetic properties of the actinide elements and their metallic compounds*, Reports Prog. Phys. 41 (1978) 1547.

[35] A.T. Aldred, B.D. Dunlap, D.J. Lam, I. Nowik, *Magnetic properties of neptunium Laves phases:* $NpAl_2$, $NpOs_2$, $NpIr_2$, *and* $NpRu_2$, Phys. Rev. B. 10 (1974) 1011–1019.

[36] V. Sechovsky, L. Havela, *Intermetallic compounds of actinides*, in: E.P. Wohlfarth, K.H.J. Buschow (Eds.), Handb. Ferromagn. Mater., Elsevier B.V., Amsterdam, 1988: pp. 309–491.

[37] A.C. Lawson, A. Williams, J.G. Huber, R.B. Roof, *Magnetic structure of UPt*, J. Less-Common Met. 120 (1986) 113–122.

[38] R. Troc, W. Suski, *The discovery of the ferromagnetism in* $U(H,D)_3$ *: 40 years later*, J. Alloys Compd. 219 (1995) 1–5.

[39] D.M. Gruen, *Magnetic properties of uranium hydride*, J. Chem. Phys. 23 (1955) 1708–1710.

[40] W. Bartscher, A. Boeuf, R. Caciuffo, J.M. Fournier, W.F. Kuhs, J. Rebizant, F. Rustichelli, *Neutron diffraction study of* β-UD_3 *and* β-UH_3, Solid State Commun. 53 (1985) 423–426.

[41] J.W. Ward, J.M. Haschke, J. Rebizant, W. Bartscher, *Phase relations, structures and bonding for the Pa-H system*, J. Less Common Met. 100 (1984) 195–214.

[42] J.W. Ward, L.E. Cox, J.L. Smith, G.R. Stewart, J.H. Wood, *Some observations on the electronic structure of* β-UD_3, Le J. Phys. Colloq. 40 (1979) C4-15-C4-17.

[43] T. Gouder, A. Seibert, J. Rebizant, F. Huber, L. Havela, *Comparative photoemission study of actinide (Am, Pu, Np and U) metals, nitrides, and*

hydrides, in: Mater. Res. Soc. Symp. Proc., Cambridge University Press, 2007: pp. 17–28.

[44] A.C. Lawson, J.A. Goldstone, J.G. Huber, A.L. Giorgi, J.W. Conant, A. Severing, B. Cort, R.A. Robinson, *Magnetic structures of actinide materials by pulsed neutron diffraction* (invited), J. Appl. Phys. 69 (1991) 5112–5116.

[45] I. Tkach, M. Paukov, D. Drozdenko, M. Cieslar, B. Vondráčková, Z. Matěj, D. Kriegner, A. V. Andreev, N.-T.H. Kim-Ngan, I. Turek, M. Diviš, L. Havela, *Electronic properties of* $\alpha-UH_3$ *stabilized by Zr*, Phys. Rev. B. 91 (2015) 115116.

[46] A.C. Switendick, *Electronic energy band structure of* UH_3, J. Less-Common Met. 88 (1982) 257–262.

[47] L. Havela, M. Paukov, I. Tkach, Z. Matěj, D. Kriegner, S. Mašková, B. Vondráčková, M. Prachařová, I. Turek, M. Diviš, M. Cieslar, D. Drozdenko, N.-T.H. Kim-Ngan, A.V. Andreev, UH_3*-based ferromagnets: New look at an old material*, J. Magn. Magn. Mater. 400 (2016) 130–136.

[48] A.P. Gonçalves, M.S. Henriques, J.C. Waerenborgh, L.C.J. Pereira, E.B. Lopes, M. Almeida, S. Mašková, L. Havela, A. Shick, Z. Arnold, D. Berthebaud, O. Tougait, H. Noël, *Peculiarities of U-based Laves phases*, IOP Conf. Ser. Mater. Sci. Eng. 9 (2010) 012090.

[49] L. Severin, L. Nordström, M.S.S. Brooks, B. Johansson, *Theoretical study of the ferromagnetism in* UNi_2, Phys. Rev. B. 44 (1991) 9392–9399.

[50] R.J. Trainor, M.B. Brodsky, H. V. Culbert, *Specific Heat of the Spin-Fluctuation System* UAl_2, Phys. Rev. Lett. 34 (1975) 1019–1022.

[51] K.H.J. Buschow, *Handbook of magnetic materials*. Volume 11, North-Holland, 1998.

[52] C. Uher, *Thermal Conductivity of Metals*, in: T.M. Tritt (Ed.), Therm. Conduct. Theory, Prop. Appl., Springer US, Berlin, 2005: p. 290.

[53] L.N. Cooper, *Theory of Superconductivity*, Am. J. Phys. 28 (1960) 91–101.

[54] J. Bardeen, L.N. Cooper, J.R. Schrieffer, *Theory of superconductivity*, Phys. Rev. 108 (1957) 1175–1204.

[55] A. Nie, M. Williams, *Determination of the critical field and critical temperature for various type I and type II metals and alloys*, Harvard Univ. 77 Massachusetts Ave. Cambridge. (2016).

[56] G.R. Stewart, *Unconventional superconductivity*, Adv. Phys. 66 (2017) 75–196.

[57] J.S. Dugdale, *Electron transport in metallic glasses*, Contemp. Phys. 28 (1987) 547–572.

[58] E. Brück, H. Nakotte, F.R. De Boer, P.F. De Chĝtel, H.P. Van Der Meulen, J.J.M. Franse, A.A. Menovsky, N.H. Kim-Ngan, L. Havela, V. Sechovsky, J.A.A.J. Perenboom, N.C. Tuan, J. Sebek, *Electronic properties of UNiAl in high magnetic fields*, Phys. Rev. B. 49 (1994) 8852–8863.

[59] Z. Fisk, H.R. Ott, J.L. Smith, *Superconductivity of uranium compounds*, Phys. B C. 130 (1985) 159–162.

[60] G.R. Stewart, Z. Fisk, J.O. Willis, J.L. Smith, *Possibility of coexistence of bulk superconductivity and spin fluctuations in UPt$_3$*, in: H.R. Ott (Ed.), Ten Years Supercond. 1980–1990, Springer, Dordrecht, 1984: pp. 85–88.

[61] V. Sechovsky, L. Havela, L. Jirman, E. Brück, F.R. de Boer, H. Nakotte, W. Ye, T. Takabatake, H. Fujii, T. Suzuki, T. Fujita, *Magnetoresistance behaviour of UNiGa and UNiAl*, Phys. B Condens. Matter. 177 (1992) 155–158.

[62] I. Tkach, N.-T.H. Kim-Ngan, A. Warren, T. Scott, A.P. Gonçalves, L. Havela, *Electronic properties of γ-U and superconductivity of U–Mo alloys*, Phys. C Supercond. 498 (2014) 14–20.

[63] J.H. Mooij, *Electrical conduction in concentrated disordered transition metal alloys*, Phys. Status Solidi. 17 (1973) 521–530.

[64] T.G. Berlincourt, *Hall effect, resistivity and superconductivity of some metastable uranium-rich alloys*, J. Phys. Chem. Solids. 11 (1959) 12–17.

[65] Z. Fisk, H.R. Ott, *Superconductivity in Uranium materials*, Int. J. Mod. Phys. B. 03 (1989) 535–571.

[66] M. Krupska, N.-T.H. Kim-Ngan, S. Sowa, M. Paukov, I. Tkach, D. Drozdenko, L. Havela, Z. Tarnawski, *Structure, Electrical Resistivity and Superconductivity of Low-alloyed γ-U Phase Retained to Low Temperatures by Means of Rapid Cooling*, Acta Metall. Sin. (English Lett. 29 (2016) 388–398.

[67] L. Havela, M. Paukov, V. Buturlim, I. Tkach, S. Mašková, M. Dopita, S. Maskova, M. Dopita, *Origin of negative resistivity slope in U-based*

ferromagnets, Phys. B Condens. Matter. 536 (2018) 527–531.

[68] M. Falkowski, V. Buturlim, M. Paukov, L. Havela, *Thermal transport and thermopower of bcc U-Mo splat-cooled alloys*, Phys. B Condens. Matter. 536 (2018) 535–538.

[69] Z. Hua, T. Yao, A. Khanolkar, X. Ding, K. Gofryk, L. He, M. Benson, D. Hurley, *Intragranular thermal transport in U–50Zr*, J. Nucl. Mater. 534 (2020) 152145.

[70] J.B. Moser, O.L. Kruger, *Thermal Conductivity and Heat Capacity of the Monocarbide, Monophosphide, and Monosulfide of Uranium*, J. Appl. Phys. 38 (1967) 3215–3222.

[71] S. Motoyama, Y. Ichikawa, Y. Hiwatari, A. Oe, *Thermal conductivity of uranium dioxide by nonequilibrium molecular dynamics simulation*, Phys. Rev. B. 60 (1999) 292–298.

[72] I.C. Hobson, R. Taylor, J.B. Ainscough, *Effect of porosity and stoichiometry on the thermal conductivity of uranium dioxide*, J. Phys. D. Appl. Phys. 7 (1974) 1003–1015.

[73] K. Gofryk, S. Du, C.R. Stanek, J.C. Lashley, X.-Y. Liu, R.K. Schulze, J.L. Smith, D.J. Safarik, D.D. Byler, K.J. McClellan, B.P. Uberuaga, B.L. Scott, D.A. Andersson, *Anisotropic thermal conductivity in uranium dioxid*e, Nat. Commun. 5 (2014) 4551.

[74] R.O.A. Hall, J.A. Lee, *The thermal conductivity of α uranium between 5 and 100 K*, J. Low Temp. Phys. 4 (1971) 415–419.

[75] P. Coleman, *Condensed-matter physics: Magnetic spins that last for ever*, Nature. 413 (2001) 788–789.

[76] Q. Si, S. Rabello, K. Ingersent, J.L. Smith, *Locally critical quantum phase transitions in strongly correlated metals*, Nature. 413 (2001) 804–808.

[77] H. Amitsuka, T. Shimamoto, T. Honma, T. Sakakibara, *Single uranium-site properties of dilute uranium alloys* $U_xTh_{1-x}Pd_2Si_2$ *(*$x \leq 0.07$*)*, Phys. B Phys. Condens. Matter. 206–207 (1995) 461–463.

[78] A. Schröder, G. Aeppli, R. Coldea, M. Adams, O. Stockert, H. V. Löhneysen, E. Bucher, R. Ramazashvili, P. Coleman, *Onset of antiferromagnetism in heavy-fermion metals*, Nature. 407 (2000) 351–355.

[79] P. Gegenwart, J. Custers, C. Geibel, K. Neumaier, T. Tayama, T. Tayama, K.

Tenya, O. Trovarelli, F. Steglich, *Magnetic-field induced quantum critical point in $YbRh_2Si_2$*, Phys. Rev. Lett. 89 (2002) 056402/1-056402/4.

[80] S. Raymond, D. Jaccard, *Electronic properties of under pressure*, Phys. Rev. B - Condens. Matter Mater. Phys. 61 (2000) 8679–8682.

[81] G.R. Stewart, *Non-fermi-liquid behavior in d- and f-electron metals*, Rev. Mod. Phys. 73 (2001) 797–855.

[82] S. Paschen, T. Lühmann, S. Wirth, P. Gegenwart, O. Trovarelli, C. Geibel, F. Steglich, P. Coleman, Q. Si, *Hall-effect evolution across a heavy-fermion quantum critical point*, Nature. 432 (2004) 881–885.

[83] P.M. de L.C. Estrela, *Non-fermi liquid behaviour in uranium-based heavy-fermion compounds*, University of Amsterdam, 2000.

[84] P. Coleman, *Theories of non-Fermi liquid behavior in heavy fermions*, Phys. B Condens. Matter. 259–261 (1999) 353–358.

[85] E. Miranda, V. Dobrosavljevic, G. Kotliar, *Kondo disorder: a possible route towards non-Fermi-liquid behaviour*, J. Phys. Condens. Matter. 8 (1996) 9871–9900.

[86] A.J. Millis, *Effect of a nonzero temperature on quantum critical points in itinerant fermion systems*, Phys. Rev. B. 48 (1993) 7183–7196.

[87] A.H.C. Neto, G. Castilla, B.A. Jones, *Non-Fermi liquid behavior and griffiths phase in f-electron compounds*, Phys. Rev. Lett. 81 (1998) 3531–3534.

[88] T. Moriya, T. Takimoto, *Anomalous Properties around Magnetic Instability in Heavy Electron Systems*, J. Phys. Soc. Japan. 64 (1995) 960–969.

[89] B.R. Coles, *Heavy-fermion intermetallic compounds*, Contemp. Phys. 28 (1987) 143–157.

[90] M. Paukov, L. Havela, N.-T.N.-T.H. Kim-Ngan, V. Buturlim, I. Tkach, D. Drozdenko, S. Mašková, S. Sowa, Z. Molčanová, M. Mihálik, M. Krupska, Z. Molcanova, M. Mihalik, M. Krupska, *Variations of magnetic properties of UH_3 with modified structure and composition*, J. Sci. Adv. Mater. Devices. 1 (2016) 185–192.

[91] L. Havela, V. Sechovský, P. Svoboda, M. Diviš, H. Nakotte, K. Prokeš, F.R. De Boer, A. Purwanto, R.A. Robinson, A. Seret, J.M. Winand, J. Rebizant, J.C. Spirlet, M. Richter, H. Eschrig, *Heavy fermion behavior of U_2T_2X compounds*, J. Appl. Phys. 76 (1994) 6214–6216.

[92] A.M. Boring, R.C. Albers, G.R. Stewart, D.D. Koelling, *Electronic structure and anomalous properties of* UAl_2*,* $NpAl_2$*, and* $PuAl_2$, Phys. Rev. B. 31 (1985) 3251–3259.

[93] G.R. Stewart, A.L. Giorgi, B.L. Brandt, S. Foner, A.J. Arko, *High-field specific heat of the spin-fluctuation system* UAl_2, Phys. Rev. B. 28 (1983) 1524–1528.

[94] M.S. Wire, J.D. Thompson, Z. Fisk, *Influence of spin fluctuations on the electrical resistance of* UAl_2 *and* UPt_3 *at high pressures and low temperatures*, Phys. Rev. B. 30 (1984) 5591–5595.

[95] F. Mayr, G.-F. v. Blanckenhagen, G.R. Stewart, *Non-Fermi-liquid behavior and spin fluctuations in doped* UAl_2, Phys. Rev. B. 55 (1997) 947–953.

[96] H.L. Yakel, *Review of x-ray diffraction studies in uranium alloys*, Tennessee, 1973.

[97] J.C. Marmeggi, R. Currat, A. Bouvet, G.H. Lander, *Phonon softening in alpha-uranium associated with the CDW transition*, Phys. B Condens. Matter. 263–264 (1999) 624–626.

[98] C. Suryanarayana, *Rapid Solidification Processing*, Encycl. Mater. Sci. Technol. (2002) 1–10.

[99] R.C. Budhani, T.C. Goel, K.L. Chopra, *Melt-spinning technique for preparation of metallic glasses*, Bull. Mater. Sci. 4 (1982) 549–561.

[100] M. Baricco, M. Palumbo, D. Baldissin, E. Bosco, E. Battezzati, *Metastable phases and phase diagrams*, La. Met. Ital. (2004) 1.

[101] J.W. Elmer, S.M. Allen, T.W. Eagar, *Microstructural development during solidification of stainless steel alloys*, Metall. Trans. A. 20 (1989) 2117–2131.

[102] C.W. Jacob, B.E. Warren, *The Crystalline Structure of Uranium*, J. Am. Chem. Soc. 59 (1937) 2588–2591.

[103] A.S. Wilson, R.E. Rundle, IUCr, *The structures of uranium metal*, Acta Crystallogr. 2 (1949) 126–127.

[104] J. Thewlis, *Structures of Uranium*, Nature. 168 (1951) 198–199.

[105] P. Duwez, *The Effect of the Rate of Cooling on the Allotropic Transformation Temperatures of Uranium*, J. Appl. Phys. 24 (1953) 152–156.

[106] J. Delaplace, *Centre d'Études Nucléaires de Saclay Rapport no. C.E.A.* 1399, 1960.

[107] R.F. Hills, B.R. Butcher, J.A. Heywood, *A study of the effect of cooling rate on the decomposition of the γ-phase in uranium-low molybdenum alloys*, J. Less Common Met. 3 (1961) 155–169.

[108] R.F. Hills, B.W. Howlett, B.R. Butcher, *Further studies on the decomposition of the γ phase in uranium-low molybdenum alloys*, J. Less Common Met. 5 (1963) 369–373.

[109] K. Tangri, G.I. Williams, *Metastable phases in the uranium molybdenum system and their origin*, J. Nucl. Mater. 4 (1961) 226–233.

[110] A.G. Harding, M.B. Waldron, *Transformations in uranium alloys with high solute solubility in the B.C.C. γ phase. Part 1. Preliminary observations on the "'banded structures'" produced by non-equilibrium transformations in uranium alloys*, 1958.

[111] V.P. Sinha, P.V. Hegde, G.J. Prasad, G.K. Dey, H.S. Kamath, *Phase transformation of metastable cubic γ-phase in U–Mo alloys*, J. Alloys Compd. 506 (2010) 253–262.

[112] N.-T.H. Kim-Ngan, I. Tkach, S. Mašková, A.P. Gonçalves, L. Havela, *Study of decomposition and stabilization of splat-cooled cubic γ-phase U–Mo alloys*, J. Alloys Compd. 580 (2013) 223–231.

[113] B.F. Hills, B.R. Butcher, B.W. Howlett, D. Stewart, *The effect of cooling rate on the decomposition of the γ-phase in uranium-zirconium alloys*, J. Nucl. Mater. 16 (1965) 25–38.

[114] J.G. Huber, P.H. Ansari, *The superconductivity of bcc U-Zr alloys*, Phys. B+C. 135 (1985) 441–444.

[115] J. Keeler, H. Saller, *Uranium-titanium alloys*, US2743174A, 1946.

[116] R.W. Buzzard, R.B. Liss, D.P. Fickle, *Titanium-Uranium System in the Region 0 to 30 Atomic Percent of Titanium*, J. Res. Natl. Bur. Stand. (1934). 50 (1953) 209.

[117] M.C. Udy, F.W. Boulger, *Uranium-titanium alloy system*, JOM. 6 (1954) 207–210.

[118] D.L. Douglass, L.L. Marsh, *Effect of heat treatment on the hardness and microstructure of U-Ti alloys*, JOM. 9 (1957) 1260–1267.

[119] C.A.W. Peterson, W.J. Steele, S.L. DiGiallonardo, *Isothermal transformation study of some uranium-base alloys*, (n.d.).

[120] H.M. Volz, R.E. Hackenberg, A.M. Kelly, W.L. Hults, A.C. Lawson, R.D. Field, D.F. Teter, D.J. *Thoma, X-ray diffraction analyses of aged U-Nb alloys*, J. Alloys Compd. 444–445 (2007) 217–225.

[121] A.M. Kelly, R.D. Field, D.J. Thoma, *Metallographic preparation techniques for U-6 wt.%Nb*, J. Nucl. Mater. 429 (2012) 118–127.

[122] J.T. McKeown, L.L. Hsiung, H.J. Ryu, J.M. Park, P.E.A. Turchi, W.E. King, *Rapidly solidified U-6 wt%Nb powders for dispersion-type nuclear fuels*, J. Nucl. Mater. 448 (2014) 72–79.

[123] A.J. Sunwoo, D.S. Hiromoto, *Effects of natural aging on the tensile properties of water-quenched U-6%Nb alloy*, J. Nucl. Mater. 327 (2004) 37–45.

[124] Y. Zhang, X. Wang, Q. Xu, Y. Li, *X-ray diffraction study of low temperature aging in U-5.8 wt.%Nb*, J. Nucl. Mater. 456 (2015) 41–45.

[125] R.A. Vandermeer, *Phase transformations in a uranium 14 at.% niobium alloy*, Acta Metall. 28 (1980) 383–393.

[126] K. Tangri, D.K. Chaudhuri, *Metastable phases in uranium alloys with high solute solubility in the BCC gamma phase. Part I — the system U-Nb*, J. Nucl. Mater. 15 (1965) 278–287.

[127] B. Djurić, *Decomposition of gamma phase in a uranium 9.5 wt. % niobium alloy*, J. Nucl. Mater. 44 (1972) 207–214.

[128] K. Miliyanchuk, L. Havela, A.V. Kolomiets, A.V. Andreev, *Effect of hydrogenation on magnetism of* U_2Co_2Sn, Phys. B Condens. Matter. 359–361 (2005) 1042–1044.

[129] C.D. Taylor, R. Scott Lillard, *Ab-initio calculations of the hydrogen-uranium system: Surface phenomena, absorption, transport and trapping*, Acta Mater. 57 (2009) 4707–4715.

[130] C.D. Taylor, T. Lookman, R.S. Lillard, *Ab initio calculations of the uranium-hydrogen system: Thermodynamics, hydrogen saturation of α-U and phase-transformation to* UH_3, Acta Mater. 58 (2010) 1045–1055.

[131] Y. Fukai, *The Metal-Hydrogen System: Basic Bulk Properties*, Springer, Berlin, 2006.

[132] C. Kun, L. Junsheng, L. Gan, *Density functional study of hydrogen atomic adsorption and transportation on γ-U (100) surface*, At. Energy Sci. Technol. 46 (2012) 907–911.

[133] Y. Yang, P. Zhang, P. Shi, X. Wang, *s–d Electronic Interaction Induced H_2 Dissociation on the γ-U(100) Surface and Influences of Niobium Doping*, J. Phys. Chem. C. 115 (2011) 23381–23386.

[134] D.R. Morrison, A.K. Ray, *Atomic H interaction with the γ-U (100) surface*, Phys. Status Solidi. 250 (2013).

[135] E.F. Holby, *Crystallographic orientation effects of hydrogen diffusion in α-uranium from DFT: Interpreting variations in experimental data*, J. Nucl. Mater. 513 (2019) 293–296.

[136] I. Grenthe, J. Drożdżyński, T. Fujino, E.C. Buck, T.E. Albrecht-Schmitt, S.F. Wolf, *Uranium*, in: L.R. Morss, N.M. Edelstein, J. Fuger (Eds.), Chem. Actin. Trans. Elem., Springer Netherlands, Dordrecht, 2008: pp. 253–698.

[137] J. Grunzweig-Genossar, M. Kuznietz, B. Meerovici, *Nuclear magnetic resonance in uranium hydride and deuteride*, Phys. Rev. B. 1 (1970) 1958–1977.

[138] R.N.R. Mulford, F.H. Ellinger, W.H. Zachari-Asen, *A new form of uranium hydride*, J. Am. Chem. Soc. 76 (1954) 297–298.

[139] R. Orr, H. Godfrey, C. Broan, D. Goddard, G. Woodhouse, P. Durham, A. Diggle, J. Bradshaw, *Formation and physical properties of uranium hydride under conditions relevant to metallic fuel and nuclear waste storage*, J. Nucl. Mater. 477 (2016) 236–245.

[140] Y. Kojima, Y. Kawai, S. Towata, T. Matsunaga, T. Shinozawa, M. Kimbara, *Development of metal hydride with high dissociation pressure*, J. Alloys Compd. 419 (2006) 256–261.

[141] M. Kandavel, V. Bhat, A. Rougier, L. Aymard, G. Nazri, J. Tarascon, I*mprovement of hydrogen storage properties of the AB_2 Laves phase alloys for automotive application*, Int. J. Hydrogen Energy. 33 (2008) 3754–3761.

[142] D. Ivey, D. Northwood, *Hydrogen site occupancy in AB_2 Laves phases*, J. Less Common Met. 115 (1986) 23–33.

[143] W. Bartscher, J. Rebizant, J.M. Haschke, *Equilibria and thermodynamic properties of the $ThZr_2$-H system*, J. Less Common Met. 136 (1988) 385–394.

[144] Y. Takuya, T. Satoru, Y. Michio, *Hydrogen absorption-desorption properties of U_2Ti*, J. Nucl. Mater. 170 (1990) 140–146.

[145] Y. Takuya, K. Hideo, Y. Michio, I. for M.R.U. The Oarai Branch, I. for

M.R.U. The Oarai Branch, F. of E. of T. Nuclear Engineering Research Laboratory, *New Ternary Hydride Formation in U-Ti-H System*, Sci. Reports Res. Institutes, Tohoku Univ. Ser. A, Physics, Chem. Metall. 35 (1991) 275–282.

[146] K.M. Nicholson, D.S. Sholl, *First-Principles Prediction of Ternary Interstitial Hydride Phase Stability in the Th–Zr–H System*, J. Chem. Eng. Data. 59 (2014) 3232–3241.

[147] S. Sowa, N.-T.H. Kim-Ngan, M. Krupska, M. Paukov, V. Buturlim, L. Havela, *Structure and properties of U alloys with selected d-metals and their hydrides*, Phys. B Condens. Matter. 536 (2018) 546–552.

[148] T. Yamamoto, H. Kayano, S. Sinaga, F. Ono, S. Tanaka, M. Yamawaki, *Hydrogen absorption-desorption properties of UCo*, J. Less-Common Met. 172–174 (1991) 71–78.

[149] V. Pecharsky, P. Zavalij, *Fundamentals of Diffraction*, in: Fundam. Powder Diffr. Struct. Charact. Mater., Springer US, Boston, MA, n.d.: pp. 133–149.

[150] K. Tangri, D.K. Chaudhuri, C.N. Rao, *Metastable phases in uranium alloys with high solute solubility in the BCC gamma phase. Part II — the system U-Ru*, J. Nucl. Mater. 15 (1965) 288–297.

[151] W. Zhou, R. Apkarian, Z.L. Wang, D. Joy, *Fundamentals of Scanning Electron Microscopy (SEM)*, in: Scanning Microsc. Nanotechnol., Springer, New York, 2006: pp. 1–40.

[152] T. Maitland, S. Sitzman, *Backscattering Detector and EBSD in Nanomaterials Characterization*, in: Scanning Microsc. Nanotechnol., Springer, New York, 2006: pp. 41–75.

[153] D. Drozdenko, P. Minarik, M. Paukov, V. Buturlim, I. Tkach, L. Havela, *EBSD Study of Uranium Alloys*, MRS Adv. 1 (2016) 3013–3018.

[154] J.C. Lashley, M.F. Hundley, A. Migliori, J.L. Sarrao, P.G. Pagliuso, T.W. Darling, M. Jaime, J.C. Cooley, W.L. Hults, L. Morales, D.J. Thoma, J.L. Smith, J. Boerio-Goates, B.F. Woodfield, G.R. Stewart, R.A. Fisher, N.E. Phillips, *Critical examination of heat capacity measurements made on a Quantum Design physical property measurement system*, Cryogenics (Guildf). 43 (2003) 369–378.

[155] Quantum Design, *Physical Property Measurement System: Heat Capacity*

Option User's Manual, (2010).

[156] J. Prchal, V. Buturlim, J. Valenta, M. Dopita, M. Divis, I. Turek, L. Kyvala, D. Legut, L. Havela, *Pressure variations of the 5f magnetism in* UH_3, J. Magn. Magn. Mater. 497 (2020) 165993.

[157] N. Fujiwara, T. Matsumoto, K. Nakazawab, A. Hisada, Y. Uwatoko, *Fabrication and efficiency evaluation of a hybrid NiCrAl pressure cell up to 4 GPa*, Rev. Sci. Instrum. 78 (2007) 073905.

[158] K. Murata, H. Yoshino, H.O. Yadav, Y. Honda, N. Shirakawa, *Pt resistor thermometry and pressure calibration in a clamped pressure cell with the medium*, Daphne 7373, Rev. Sci. Instrum. 68 (1997) 2490–2493.

[159] D. Staško, J. Prchal, M. Klicpera, S. Aoki, K. Murata, *Pressure media for high pressure experiments, Daphne Oil 7000 series*, High Press. Res. (2020) 1–12.

[160] J. Besson, P.L. Blum, J. Laugier, *Sur l'existence d'une transformation directe* $\alpha \rightarrow \gamma$ *dans l'uranium disperse dans un milieu inerte*, JNuM. 16 (1965) 74–75.

[161] R. Wyckoff, *Rocksalt structure*, Cryst. Struct. 1 (1963) 85–237.

[162] E. Wicke, K. Otto, *Über das System Uran—Wasserstoff und die Kinetik der Uranhydridbildung*, Zeitschrift Für Phys. Chemie. 31 (1962) 222–248.

[163] G. Kimmel, A. Landau, J. Sariel, U. Admon, *Phase transformations in dilute U-Ti alloys*, J. Less-Common Met. (1986) 483–486.

[164] J. Lehmann, R.F. Hills, *Proposed nomenclature for phases in uranium alloys*, J. Nucl. Mater. (n.d.).

[165] I. Tkach, N.-T.H. Kim-Ngan, S. Mašková, M. Dzevenko, L. Havela, A. Warren, C. Stitt, T. Scott, *Characterization of cubic* γ*-phase uranium molybdenum alloys synthesized by ultrafast cooling*, J. Alloys Compd. 534 (2012) 101–109.

[166] L.B. Asprey, R.A. Penneman, *Chemistry of the actinides*, Los Alamos Scientific Lab., N. Mex., 1967.

[167] A.F. Wells, *Structural Inorganic Chemistry*, 5th edn., Clarendon, (1984).

[168] M. Anagnostidis, M. Colombié, H. Monti, *Phases metastables dans les alliages uranium-niobium*, J. Nucl. Mater. 11 (1964) 67–76.

[169] M. Isino, *Concentration and temperature dependences of the electrical resistivity of disordered binary transition metal alloys*, J. Phys. Soc. Japan. 54 (1985) 3848–3857.

[170] J.C. Lashley, B.E. Lang, J. Boerio-Goates, B.F. Woodfield, G.M. Schmiedeshoff, E.C. Gay, C.C. McPheeters, D.J. Thoma, W.L. Hults, J.C. Cooley, R.J. Hanrahan, J.L. Smith, *Low-temperature specific heat and critical magnetic field of α-uranium single crystals*, Phys. Rev. B - Condens. Matter Mater. Phys. 63 (2001) 224510.

[171] N.R. Werthamer, E. Helfand, P.C. Hohenberg, *Temperature and purity dependence of the superconducting critical field,* H_{c2}*. III. Electron spin and spin-orbit effects*, Phys. Rev. 147 (1966) 295–302.

[172] D. Dew-Hughes, *Superconducting A-15 compounds: A review*, Cryogenics (Guildf). 15 (1975) 435–454.

[173] P.W. Anderson, K.A. Muttalib, T. V. Ramakrishnan, *Theory of the "universal" degradation of* T_c *in high-temperature superconductors*, Phys. Rev. B. 28 (1983) 117–120.

[174] L. Havela, I. Tkach, M. Paukov, Z. Matej, D. Drozdenko, A. V. Andreev, N.-T.H. Kim-Ngan, *Structure and properties of hydrides of γ-U alloys*, J. Alloys Compd. 645 (2015) S190–S192.

[175] A.J. Arko, J.J. Joyce, L. Havela, *5f-Electron Phenomena in the Metallic State*, in: Chem. Actin. Trans. Elem., Springer Netherlands, Dordrecht, n.d.: pp. 2307–2379.

[176] V.O. Struebing, H.H. Hill, J.L. Smith, *Superconductivity and magnetic susceptibility of TiU alloys*, Solid State Commun. 25 (1978) 1041–1042.

[177] C.H. Cheng, K.P. Gupta, E.C. Van Reuth, P.A. Beck, *Low-temperature specific heat of body-centered cubic Ti-V alloys*, Phys. Rev. 126 (1962) 2030–2033.

[178] L.E. DeLong, J.G. Huber, K.N. Yang, M.B. Maple, *Observation of High-Field Superconductivity of a Strongly Interacting Fermi Liquid in* U_6Fe, Phys. Rev. Lett. 51 (1983) 312–315.

[179] L. Lutterotti, *Total pattern fitting for the combined size-strain-stress-texture determination in thin film diffraction*, Nucl. Instruments Methods Phys. Res. Sect. B Beam Interact. with Mater. Atoms. 268 (2010) 334–340.

[180] I. Tkach, S. Mašková, Z. Matěj, N.-T.H. Kim-Ngan, A. V. Andreev, L. Havela, *Ferromagnetism with* $T_C = 200$ *K in the amorphous 5f compound* $UH_3Mo_{0.18}$, Phys. Rev. B. 88 (2013) 060407.

[181] H. Oesterreicher, F.T. Parker, M. Misroch, *Analysis of giant intrinsic magnetic hardness in* $SmCo_{5-x}Ni_x$, Phys. Rev. B. 18 (1978) 480–485.

[182] T. Egami, *Theory of intrinsic magneitc after-effect II. Tunnelling process and comparison with experiments*, Phys. Status Solidi. 20 (1973) 157–165.

[183] O. Koloskova, V. Buturlim, M. Paukov, P. Minarik, M. Dopita, K. Miliyanchuk, L. Havela, *Hydrogen in U-T alloys: Crystal structure and magnetism of* UH_3*-V*, J. Alloys Compd. (2020) 157406.

[184] J.C. Fernandes, M.A. Continentino, A.P. Guimarães, *The low temperature contributions to β-uranium hydride specific heat*, Solid State Commun. 55 (1985) 1011–1015.

[185] S.F. Matar, *Drastic changes in the electronic and magnetic structures of hydrogenated* U_2Ti *intermetallic from first principles*, J. Magn. Magn. Mater. 358–359 (2014) 70–75.

[186] L. Havela, M. Paukov, I. Tkach, V. Buturlim, Z. Matej, S. Maskova, I. Turek, M. Divis, D. Drozdenko, M. Cieslar, M. Dopita, Z. Molcanova, M. Mihalik, *Strong 5f ferromagnetism in* UH_3*-based materials*, MRS Adv. 1 (2016) 2987–2992.

[187] T. Yamamoto, M. Teshigawara, H. Kayano, N. Minakawa, S. Funahashi, *Formation and crystal structure of* UTi_2D_x, J. Alloys Compd. 224 (1995) 36–38.

[188] R. Weast, *CRC Handbook of Chemistry and Physics*, Boca Raton: CRC, 1981.

[189] J.J.M. Franse, I*tinerant-electron magnetism studied in high-magnetic field and high-pressure experiments*, J. Magn. Magn. Mater. 31–34 (1983) 819–828.

[190] Z. Tarnawski, L. Kolwicz-Chodak, H. Figiel, A. Budziak, L. Havela, J. Vejpravová, A. Kolomiets, V. Sechovský, N.-T.H. Kim-Ngan, *Specific heat of* $TbMn_2(H,D)_2$, Phys. B Condens. Matter. 355 (2005) 202–206.

[191] N.D. Patel, A. Mukherjee, N. Kaushal, A. Moreo, E. Dagotto, *Non-Fermi Liquid Behavior and Continuously Tunable Resistivity Exponents in the Anderson-Hubbard Model at Finite Temperature*, Phys. Rev. Lett. 119 (2017) 086601.

[192] J.E. Parrot, *Thermal Conductivity of Solids*. AD Stuckes, (1975).

[193] F. Pobell, *Matter and Methods at Low Temperatures*, Springer Berlin Heidelberg, Berlin, Heidelberg, 2007.

[194] A.T.T. Burkov, T. Nakama, T. Kohama, T. Shimoji, K. Shintani, R. Shimabukuro, K. Yagasaki, E. Gratz, *Contribution of spin fluctuations to the low-temperature resistivity and thermopower of* YCo_2, J. Magn. Magn. Mater. 177–181 (1998) 1069–1070.

[195] K. Behnia, D. Jaccard, J. Flouquet, *On the thermoelectricity of correlated electrons in the zero-temperature limit*, J. Phys. Condens. Matter. 16 (2004) 5187–5198.

[196] G. Katz, A.J. Jacobs, *Lattice constants of the intermetallic compounds* UAl_2 *and* UFe_2, J. Nucl. Mater. 5 (1962) 338–340.

[197] M.B. Brodsky, *Magnetic susceptibility of* $U_{1-x}\ Th_xAl_2$, Le J. Phys. Colloq. 40 (1979) C4-147-C4-149.

[198] J.S. Kim, J. Alwood, S.A. Getty, F. Sharifi, G.R. Stewart, U_2Co_2Sn *: An undoped non-Fermi-liquid system with* $C_e \approx \gamma - AT$, Phys. Rev. B. 62 (2000) 6986–6990.

[199] A.L. Giorgi, G.R. Stewart, M.S. Wire, J.O. Willis, *New spin-fluctuation system:* $U_{0.5}Th_{0.5}Al_3$, Phys. Rev. B. 32 (1985) 3010–3013.

[200] J.J.M. Franse, P.H. Frings, F.R. de Boer, A. Menovsky, C.J. Beers, A.P.J. van Deursen, H.W. Myron, A.J. Arko, *Suppression of spin fluctuations in* UAl_2 *in high magentic fields*, Phys. Rev. Lett. 48 (1982) 1749–1752.

[201] M. Zimmermann, M. Carrard, M. Gremaud, W. Kurz, *Characterization of the banded structure in rapidly solidified Al-Cu alloys*, Mater. Sci. Eng. A. 134 (1991) 1278–1282.

[202] I.A. Kruglov, A.G. Kvashnin, A.F. Goncharov, A.R. Oganov, S.S. Lobanov, N. Holtgrewe, S. Jiang, V.B. Prakapenka, E. Greenberg, A. V Yanilkin, *Uranium polyhydrides at moderate pressures: Prediction, synthesis, and expected superconductivity*, Sci. Adv. 4 (2018) eaat9776.

[203] M. Kostrzewa, K.M. Szczęśniak, A.P. Durajski, R. Szczęśniak, *From* LaH_{10} *to room–temperature superconductors*, Sci. Rep. 10 (2020) 1592.

[204] L. Havela, M. Paukov, M. Dopita, L. Horák, D. Drozdenko, M. Diviš, I. Turek, D. Legut, L. Kývala, T. Gouder, A. Seibert, F. Huber, *Crystal Structure and Magnetic Properties of Uranium Hydride* UH_2 *Stabilized as a Thin Film*, Inorg. Chem. 57 (2018) 14727–14732.

List of Abbreviations

AC	Alternating Current
ACMS	AC Measurement System
ACT	AC Transport
AFM	Antiferromagnetic
APW	Augmented-Plane Wave
BCS	Bardeen–Cooper–Schrieffer theory
BSE	Back Scattered Electron
CDW	Charge Density Wave
DC	Direct Current
DFT	Density Functional Theory
DMFT	Dynamical Mean Field Theory
DOS	Density of States
EBSD	Electron Backscatter Diffraction
EDS	Energy Dispersive Spectroscopy
EDX	Energy-Dispersive X-Ray
FC	Field Cooling
FEG	Field Emission Gun
FIB	Focused Ion Beam
FL	Fermi Liquid
FM	Ferromagnetic
GGA	Generalized Gradient Approximation
HARD	High Anisotropy Random Distribution materials
LDA	Local Density Approximation
MAUD	Material Analysis Using Diffraction
MPMS	Magnetic Property Measurement System
NFL	non-Fermi Liquid
PIPS	Precision Ion Polishing System
PPMS	Physical Property Measurement System
PSM	Primary Solidification Mode
QCP	Quantum Critical Point
QN	Quantum Number

RKKY	Ruderman-Kittel-Kasuya-Yosida
RS	Rapid Solidification
RT	Room Temperature
SE	Secondary Electrons
SEM	Scanning Electron Microscope
SIC-LSD	Self-Interaction Corrected
SO	Spin-Orbit
SP-LDA	Spin Polarized
SQUID	Superconducting Quantum Interference Device
T	3*d* (4*d*) element
TEM	Transmission Electron Microscop
TTO	Thermal Transport option
UFC	Ultra-Fast Cooling
WHH	Werthamer-Helfand-Hohenberg theory
X	*p*-metal
XRD	X-ray diffraction
ZFC	Zero-Field Cooling

List of Tables

List of Publications

Conference contributions presented by the author

1. M. Paukov, L. Havela, N.-T. H. Kim-Ngan, **V. Buturlim**, I. Tkach, D. Drozdenko, S. Mašková, S. Sowa, Z. Molčanová, M. Mihálik, M. Krupska, *Variations of magnetic properties of UH_3 with modified structure and composition*, Cracow Symposium on Physics and Chemistry of Materials, (CSPCM), Cracow, Poland, May 6, 2016.
2. **V. Buturlim**, L. Havela, S. Sowa, N.T.H. Kim-Ngan, M. Paukov, D. Drozdenko, M. Dopita, P. Minarik, S. Mašková, *Development of bcc phase in $U_{1-x}Ti_x$ system ($x = 0.05–0.50$) and magnetic properties of related hydrides*, 7èmes Journées des Actinides (JdA), Karpacz, Poland, March 26-30, 2017.
3. **V. Buturlim**, L. Havela, S. Sowa, N.T.H. Kim-Ngan, M. Paukov, D. Drozdenko, M. Dopita, P. Minarik, S. Mašková, M. Falkowski, *Structure and properties of U-Ti alloys and their hydrides*, Week of Doctoral students, Prague, Czech Republic, June 6–8, 2017.
4. **V. Buturlim**, L. Havela, S. Sowa, N.T.H. Kim-Ngan, M. Paukov, D. Drozdenko, M. Dopita, P. Minarik, S. Mašková, M. Falkowski, *Structure and properties of U-Ti alloys and their hydrides*, 14th International Symposium om Physics of Materials, Prague, Czech Republic, September 10-15, 2017.
5. **V. Buturlim**, L. Havela, S. Sowa, H. K. N. Nhu-Tarnawska, M. Paukov, D. Drozdenko, M. Dopita, P. Minarik, S. Mašková, *Laves phase UTi_2 stabilized by hydrogen and its magnetic properties*, International Conference on Strongly Correlated Electron Systems (SCES), Prague, Czech Republic, July 17-21, 2017.
6. **V. Buturlim**, L. Havela, M. Paukov, O. Koloskova, D. Drozdenko, M. Dopita, P. Minarik, S. Mašková, M. Falkowski, *Electronic transport of the Ti rich U hydrides*, 48èmes Journées des Actinides (JdA), Praia de Porto Novo, Portugal, March 21-24, 2018.
7. **V. Buturlim**, L. Havela, O. Koloskova, D. Drozdenko, M. Dopita, P. Minarik, S. Mašková, *Strong electron correlations in the UTi_2 stabilized by hydrogen*, 12th Prague Colloquium on *f*-Electron Systems (PCFES), Prague, Czech Republic, July 4-7, 2018.

8. **V. Buturlim**, O. Koloskova, D. Drozdenko, M. Dopita, P. Minarik, S. Mašková, L. Havela, *Interaction of U-Ti alloys with hydrogen*, Uranium Science, Bristol, United Kingdom, January 21-22, 2019.

9. **V. Buturlim**, L. Havela, O. Koloskova, D. Drozdenko, M. Dopita, P, Minarik, S, Mašková, M. Falkowski, *Extraordinary enhancement of the electron mass in the U-Ti hydrides*, 49 Journées des Actinides (JdA), Erice, Italy, April 14-18, 2019.

10. **V. Buturlim**, O. Koloskova, P. Minarik, L. Havela, *Enhancement of the electronic coupling in the U-Ti alloys*, International Conference on Strongly Correlated Electron Systems (SCES), Okayama, Japan, September 23-28, 2019.

Publications in peer-reviewed international journals

1. **V. Buturlim**, M. Falkowski, M. Paukov, O. Koloskova, D. Drozdenko, M. Dopita, P. Minárik, S. Mašková, P. Doležal, L. Havela, *Spin fluctuations in hydrogen-stabilized Laves phase* UTi_2H_5, Philos. Mag. 99 (2019) 1881–1898.

2. **V. Buturlim**, L. Havela, S. Sowa, N.T.H. Kim-Ngan, M. Paukov, D. Drozdenko, M. Dopita, P. Minarik, S. Mašková, *Laves phase* UTi_2 *stabilized by hydrogen and its magnetic properties*, Phys. B Condens. Matter. 536 (2018) 539–542.

3. L. Havela, M. Paukov, **V. Buturlim**, I. Tkach, D. Drozdenko, M. Cieslar, S. Mašková, M. Dopita, Z. Matěj, *Electrical resistivity of 5f-electron systems affected by static and dynamic spin disorder*, Phys. Rev. B. 95 (2017) 235112.

4. M. Falkowski, **V. Buturlim**, M. Paukov, L. Havela, *Thermal transport and thermopower of bcc U-Mo splat-cooled alloys*, Phys. B Condens. Matter. 536 (2018) 535–538.

5. L. Havela, M. Paukov, **V. Buturlim**, I. Tkach, S. Mašková, M. Dopita, *Origin of negative resistivity slope in U-based ferromagnets*, Phys. B Condens. Matter. 536 (2018) 527–531.

6. S. Sowa, N.T.H. Kim-Ngan, M. Krupska, M. Paukov, **V. Buturlim**, L. Havela, *Structure and properties of U alloys with selected d-metals and of their hydrides*, Phys. B Condens. Matter. 536 (2018) 546-552.

7. M. Chrobak, Z. Tarnawski, S. Sowa, M. Krupska, N.-T.H. Kim-Ngan, M. Paukov, **V. Buturlim**, L. Havela, *Superconducting phase transitions in the milikelvin temperature range in splat-cooled U-Pt alloys*, Adv. Nat. Sci. Nanosci. Nanotechnol. 8 (2017) 25016.

8. M. Paukov, L. Havela, N.-T. Kim-Ngan, **V. Buturlim**, I. Tkach, D. Drozdenko, S. Mašková, S. Sowa, Z. Molčanová, M. Mihálik, M. Krupska, *Variations of magnetic properties of UH_3 with modified structure and composition*, J. Sci. Adv. Mater. Devices. 1 (2016) 185–192.

9. L. Havela, M. Paukov, I. Tkach, **V. Buturlim**, Z. Matej, S. Maskova, I. Turek, M. Divis, D. Drozdenko, M. Cieslar, M. Dopita, Z. Molcanova, M. Mihalik, *Strong 5f Ferromagnetism in UH_3-Based Materials*, MRS Adv. 1 (2016) 2987–2992.

10. D. Drozdenko, P. Minarik, M. Paukov, **V. Buturlim**, I. Tkach, L. Havela, *EBSD Study of Uranium Alloys*, MRS Adv. 1 (2016) 3013–3018.

11. J. Prchal, **V. Buturlim**, J. Valenta, M. Dopita, M. Divis, I. Turek, L. Kyvala, D. Legut, L. Havela, *Pressure variations of the 5f magnetism in UH_3*, J. Magn. Magn. Mater. 497 (2020) 165993.

12. N.T.H. Kim-Ngan, S. Sowa, M. Krupska, **V. Buturlim**, M. Paukov, D. Drozdenko, P. Minarik, L. Havela, *Superconductivity in U-Nb alloys with γ-U phase and ferromagnetism of their hydrides*, Phys. B Condens. Matter. 545 (2018) 152–158.

13. N.-T. Hoa Kim-Ngan, M. Krupska-Klimczak, **V. Buturlim**, D. Drozdenko, P. Minarik, L. Havela, S. Sowa, *Stabilization of the cubic γ-U structure in UT alloys (T= Mo, Pt, Nb, Ru, Ti)*, J. Mach. Constr. Maint. - Probl. Eksploat. no. 1 (2019).

14. **V. Buturlim**, O. Koloskova, P. Minarik, L. Havela, *Anomalous Superconductivity of the U-Ti Alloys*, in: Proc. Int. Conf. Strongly Correl. Electron Syst. J. Phys. Soc. Japan, 2020.

15. O. Koloskova, **V. Buturlim**, M. Paukov, P. Minarik, M. Dopita, K. Miliyanchuk, L. Havela, *Hydrogen in U-T alloys: Crystal structure and magnetism of UH_3-V*, J. Alloys Compd., in press; https://doi.org/10.1016/j.jallcom.2020.157406

16. U. D. Wdowik, **V. Buturlim**, L. Havela, D. Legut*, Effect of carbon vacancies and oxygen impurities on the dynamical and thermal properties of*

uranium monocarbide, J. Nucl. Mater., in press; https://doi.org/10.1016/j.jnucmat.2020.152547

17. N.T.H. Kim-Ngan, Z. Tarnawski, M. Chrobak, S. Sowa, A. Duda, M. Paukov, **V. Buturlim**, L. Havela, *Superconducting phase transitions in mK temperature range in splat-cooled* $U_{0.85}Pt_{0.15}$ *alloys*, Phys. B Condens. Matter. 536 (2018) 708–712.